2013

Finite Element Infrared Thermography Study on Concrete and Steel-Concrete Composite Structures

Tobi Peter Showunmi
Lehigh University

FINITE ELEMENT INFRARED THERMOGRAPHY STUDY ON CONCRETE AND STEEL-CONCRETE COMPOSITE STRUCTURES

by

Tobi Showunmi

A Thesis

Presented to the Graduate and Research Committee

of Lehigh University

in Candidacy for the Degree of

Master of Science

in

Structural Engineering

Department of Civil and Environmental Engineering

Lehigh University

Bethlehem, Pennsylvania

January 2013

This thesis is accepted and approved in partial fulfillment of the requirements for the Master of Science.

_____

Date

_____

Dr. Stephen Pessiki

Thesis Advisor

_____

Dr. Diplas Panos

Interim Chairperson of Department

ACKNOWLEDGMENTS

This research was supervised by Dr. Stephen Pessiki at the Center for Advanced Technology for Large Structural Systems (ATLSS) at Lehigh University. I would like to acknowledge Dr. Wesley Keller for his support in this research and paper. I would also like to thank Peter Bryan, the support of the Lehigh University Civil Engineering faculty and staff and my fellow graduate students for their support and contributions as well.

Lastly, I would like to thank my family for their encouragement, guidance and support throughout my entire experience as a student at Lehigh University.

TABLE OF CONTENTS

LIST OF TABLES

LIST OF FIGURES

CHAPTER 2

CHAPTER 3

CHAPTER 4

CHAPTER 5

CHAPTER 6

ABSTRACT

The objective of this research is to demonstrate and validate the effectiveness of impulse thermography for use in nondestructive testing on Steel-Concrete Composite Structures, and to examine the limitations of impulse thermography with parametric studies. Numerical results from experiments and finite element models were obtained in order to verify the use of thermography for composite structures. This research has shown the effectiveness of impulse thermography, but has displayed that this method of nondestructive testing (NDT) has its limitations.

It was found that, the finite element analysis technique can be successfully used to model infrared thermography for nondestructive testing. The finite element model results can reasonably locate defects within concrete specimens; although, when compared to impulse thermography BAM experiment, the surface temperature differences between the BAM model and the BAM experiment had slightly different results.

To investigate the effectiveness and limitations of thermography as a form of NDT on Steel-Concrete Composite (SCC) walls, several parameters were studied. The parameters mainly focused on the effects of the change in depths of the defects, heating intensity and heating durations of the analysis. The results of the study demonstrate that defects within the specimen were detectable at certain depths, heating intensities and heating duration. Limitations of the detectability of the defects were seen corresponding to the different parametric cases. This was clearly shown on the finite element infrared thermography models. One of the most evident limitations of detecting defects in the subsurface of the specimen was the depth of the defect. Other parameters such as the

duration of the heating and cooling process helped determine characteristics of the defects in the model. For example, longer heating and cooling durations allowed a more definitive thermographic surface image of deeper defects that cannot be seen in shorter time durations.

CHAPTER 1
INTRODUCTION

1.1 INTRODUCTION

In the United States, there are currently 104 commercially operating nuclear reactors and there is an expected four to six newly developed units that are to be built by 2020; the first of those resulting from 16 license applications made since the mid 2007 to build 24 new nuclear reactors. With several years of research and development, several more efficient and structurally sound nuclear power plants reactor designs have been tested and will soon be put into commercial use in the United States. One of the most recently tested designs is the Steel-Concrete Composite wall containment structure. This internal containment structure is composed of Steel-plate barriers supported by concrete and reinforcing steel within the two steel-plate barriers similar to a “sandwich wall”.

The construction of the Steel-Concrete Composite walls are prefabricated modules, built as composite sandwich walls. These containment structures are considerably difficult to inspect for internal defects or defects in the concrete layer between the two exterior steel plates. In order to prove quality assurance of the Steel-Concrete Composite wall structures, nondestructive testing methods are essential to implement the inspection task of these structures. This research focuses on an evaluation of the usefulness of infrared thermography as an inspection tool for Steel-Concrete Composite wall structures (hereafter referred to as SCC wall) in nuclear containment structures.

1.2 RESEARCH OBJECTIVE

The objective of this research is to demonstrate and validate the effectiveness of impulse thermography as a nondestructive test (NDT) method for detecting internal defects in Steel-Concrete Composite wall structures.

In this research, finite element analyses are performed to accurately validate and replicate the nondestructive testing method of infrared thermography on concrete and Steel-Concrete Composite walls. This approach demonstrates the usefulness of infrared thermography in any newly designed Steel-Concrete Composite wall structures.

1.3 RESEARCH APPROACH

In order to achieve the objective of this research, the following approach was taken:

1. Identify the use of impulse thermography as an effective nondestructive testing tool for inspecting Steel-Concrete Composite construction.
2. Verify the finite element approach to modeling impulse thermography by modeling existing experiments documented in the Technical University of Berlin, BAM experimental literature.
3. Use the verified modeling approach to build a finite element model and test the Steel-Concrete Composite wall model, with several parametric cases.
4. Generate the results from the Steel-Concrete Composite wall model and formulate a conclusion based on the data obtained.

1.4 SUMMARY OF FINDINGS

The findings from this study of impulse thermography as a form of nondestructive testing on Steel-Concrete Composite structures are summarized below.

The BAM experiment was a concrete infrared thermography experiment conducted by the Technical University of Berlin. The results of this experiment were used to validate the finite element model developed in this study for infrared thermography as a form of NDT. During the assessment of the results obtained in the BAM experiment, there was discrepancy with the surface temperature data recorded for one of the defects. Furthermore, a summary of the results obtained from the finite element model does differ from the results of the BAM experiment maximum difference in surface temperature over the defects. The Table 3.1 shows that there is a range from .02 Kelvin to 4.95 Kelvin, difference at the measured defects. This is not a considerably significant difference in results between the experiment and the model. However, the results from the tables and graphs in Chapter 3, show an analogous surface temperature behavior between the model and the experiment data. For example, the deeper defects caused a smaller surface temperature difference in both cases or the larger defects caused a higher surface temperature difference in both cases.

Due to the correlation between the BAM experiment and the model results, it can be concluded that the finite element model does capture the correct behavior of infrared thermography, but not with precise accuracy.

Based on the parametric cases conducted in Chapter 5 for the SCC wall model, it can also be concluded that the detection of the defects in the composite structure is limited based on the depth of the defect. In the analyses conducted in Chapter 5 and Chapter 6, it is shown that all defects directly under the steel plate at approximately .5 inches, can be easily distinguished by infrared thermography. At approximately 1.5 inches depth, detection of defects is visible at certain heat fluxes and heating durations. In

addition, at approximately 3.5 inches depth, detection of defects is not visible based on the parameters used in this study.

Also studied in Chapter 6 is how each of the different parameter fluctuations can be used to optimize the best thermographic image in locating defects and other abnormalities. For example, Figure 6.4 and Figure 6.6 shows that the deeper defects can be seen better at longer heating and cooling durations, where defects close to the surface may not show a clear difference in surface temperature; or Figures 6.13 and 6.14 display a large differences in surface temperature when the heat flux is increased.

1.5 NOTATION

The following notation is used in this report:

A	area
c_p	specific heat capacity
D	Depth
E_b	total amount of thermal radiation
e	emissivity
h	convection heat transfer coefficient
J	Joules
K	Kelvin
k	thermal conductivity
m	meters
Q	radiant energy exchange
q	heat flux density
q_{con}	heat transfer due to convection
R	rate of energy (radiation) per unit area of surface
s	seconds
T	temperature
$T_{max\Delta}$	maximum temperature difference

T_{sur}	material surface temperature
T_{∞}	surrounding ambient temperature
t	time
$t_{max\Delta}$	time of maximum temperature difference
$t\Delta_{Tmax}$	maximum temperature change occurrence
U	potential energy
α	absorptivity
α_b	thermal diffusivity
ε	Emissivity
ρ	reflectivity
σ	Stefan-Boltzmann constant (5.67 X 10^{-8} $Wm^{-2}K^{-4}$)
τ	transmissivity
^{o}c	Celsius
ΔT_{max}	maximum temperature change
∇T	temperature gradient

CHAPTER 2
RESEARCH BACKGROUND

2.1 INTRODUCTION

Recommendations on nondestructive testing methods for composite structures are given in the American Concrete Institute committee 349.3R report, “Evaluation of Existing Nuclear Safety-Related Concrete Structures”. The report describes several different alternatives to evaluate newly constructed structural components and existing nuclear structural components. Structural defects can be evaluated by means of visual inspection, nondestructive testing, invasive testing and analytical methods that are supplemented with other forms of testing. In the applications of SCC wall structures, several difficulties may arise in the evaluation of detecting abnormalities within the subsurface due to the composite structure being two extremely different material properties, the thickness of the materials and the large area of inspection that would be required for composite walls used in nuclear reactors. With the unique design of the SCC wall, infrared thermography has several characteristics that may allow this method of nondestructive testing to be highly effective in detecting defects within the concrete component of the structure, which are discussed later in the report.

2.2 NONDESTRUCTIVE TESTING

Nondestructive test (NDT) methods are used to determine concrete physical properties and to evaluate the condition of concrete in deep foundations, bridges, buildings, pavements, dams and other concrete constructions. The advantages of using NDT are the ability to assess concrete structural performance without causing significant damage to the structure. The main methods of NDT are visual inspection, stress-wave methods

for deep foundations, nuclear methods, magnetic and electrical methods, penetrability methods, infrared thermography and radar. NDT also has a large economical advantage because the method allows one to conduct a comprehensive structural assessment of the existing structure, without causing any damages or alterations to the structure. Several NDT methods can also be performed in a large-scale situation and in a quick time span compared to other methods that required samples to be tested in the laboratory.

For each NDT method, there are several advantages and limitation that favors certain methods for applications involving nuclear power plants. Table 2.1 summarizes some of the NDT methods advantages and limitations. The focus of this report is infrared thermography, which is discussed in the next section.

2.3 THERMOGRAPHY

Infrared thermography as a method of nondestructive testing has been used to identify internal defects, delaminations, and cracks in concrete structures. Infrared thermography devices sense the emission of thermal radiation and produces visual images of the varying thermal signals. This concrete testing method is based primarily on two principles. The first principle is energy in the form of electromagnetic radiation which is constantly being emitted from the surface of an object. The rate of energy emitted per surface area is given by the Stefan-Boltzmann law:

$$R = e\sigma T^4$$

Where R is the rate of energy (radiation) per unit area of surface, e is the emissivity, σ is defined as Stefan-Boltzmann constant (5.67 X 10^{-8}) and T is the temperature of the object's surface. The electromagnetic radiation emitted from the surface of an object is given off in the form of wavelengths that have characteristics that are dependent on the temperature. With an increase in temperature, the wavelength becomes shorter. At a sufficiently high temperature, the radiation becomes visible in the wavelength spectrum. Radiation at the wavelength less than 0.1 ηm pertains to gamma rays, x-rays are usually experienced at levels of 0.1 to 10 ηm , visible light has a wavelength of about 0.4 to 1 μm and infrared radiation wavelengths range from 1 to 14 μm. Radiation can be detected by special sensors that produce electrical signals in proportion to the amount of incident radiant energy. Infrared sensors can then be calibrated to send output data in terms of temperature; thus allowing the surface temperature of concrete to be measured.

The second principle corresponds to how subsurface anomalies affect the heat flow through concrete. Depending on the size, depth and type of anomalies within the concrete structure, a change in heat flow will occur and cause a localized difference in temperature around the area of heat flow disruption. This phenomenon is discussed later in this report and will play a significant role in the detection of abnormalities within concrete.

Infrared thermography as a method of nondestructive testing on concrete is influenced greatly by two main heat transfer mechanisms: conduction and radiation (which are discussed in more depth later in the report). Radiation emission and absorption of objects depends upon the emissivity of the material's surface. Emissivity is defined as the ability of the material to radiate energy into or out of a body. A perfect "black body" is an idealized physical body that absorbs all incident electromagnetic radiation.

Absorption of radiation can be altered or reduced due to several factors such as rougher surfaces that cause higher emissivity values; therefore, different surface textures and finishes will influence the surface radiation properties. Other parameters that impact the emitted infrared radiation measurements are: concrete surface emissivity, surrounding ambient temperature, thermal conductivity, volumetric-heat capacity, thickness of the heated surface, and other environmental influences. It is very unlikely for a body to behave as a perfect “black body”.

Thermographic monitoring and the data analysis systems comprise of three main components: a detector unit, a data acquisition or analysis device, and a visual image recorder. The infrared detectors are often an optical camera with lenses that transmit only infrared radiation within the wavelengths of 1 to 12 μm. Normally, infrared detectors are cooled by liquid nitrogen to a low temperature, which allows the device to sense temperature variations as minute as 0.1 Celsius. Data obtained by the detectors unit are digitized and displayed as shades of grey or color on the image displayer. Temperature varying surfaces are signified by variation of darker shades or different colors depending on the software.

2.4 HEAT TRANSFER

Heat transfer is a primary component in the use of thermography as a form of nondestructive testing. Heat transfer can be simply defined as the flow or transfer of thermal energy from one body to another. There are three modes of heat transfers, which were all used in the modeling the BAM experiment in the finite element analysis. They are conduction, convection and radiation.

2.4.1 Conduction

The transfer of thermal energy resulting from microscopic diffusion and collisions of particles within a body due to a temperature gradient is called conduction. The basic equation for conductive heat transfer is given by Fourier's law:

$$q = -k \cdot \nabla T(x, y, z, t)$$

Where *q* is the heat flux density (rate of heat transfer), k is the thermal conductivity of the material and ∇T is the temperature gradient of the element in the three directions of the local axis. The negative sign in the equation represents the heat flow from the region of higher temperature to regions of lower temperature. The thermal conductivity is the property of a material to conduct heat. Therefore, material with high conductivity will allow heat transfer to occur at a high rate across the material's body. This parameter becomes important in this study because defects or non-homogeneous characteristics within the subsurface of the objects are shown on the infrared images as surface temperature fluctuations during the infrared thermography analysis. The changes of temperatures on the surface of the specimen are caused by the different thermal properties that are found in the defects or abnormalities within the specimen subsurface.

2.4.2 Convection

Convection heat transfer occurs due to molecular motion and bulk fluid motion in a material. The transfer of heat due to convection can occur in two forms, natural convection and forced convection. In the BAM experiment and model, natural convection was used. Natural convection is driven by the material density differences

associated with the temperature changes generated by external heating or cooling forces. The basic equation for convection heat transfer is given by Newton's law:

$$q_{con} = -h \cdot (T_{\infty} - T_{sur})$$

Where q_{con} is defined as the rate of heat transfer, T_{∞} is the fluid or surrounding ambient temperature, T_{sur} is the material surface temperature, and h is the convection heat transfer coefficient. The convection heat transfer coefficient is also known as the film coefficient, and it is defined as a single quantity that subsumes a variety of features of heat transfer properties such as thermal conductivity, density, specific heat and viscosity.

2.4.3 Radiation

Radiation can be defined as the energy emitted and absorbed by a charged particle, generated by the thermal motion. Thermal radiation is the emission of electromagnetic waves from all matter that has a temperature greater than absolute zero. Essentially, thermal radiation absorption, reflection and transmission are dependent on various properties of the surface it is emanating from or traveling towards. Surface absorption, reflection and transmission are all important characteristics of radiation. The three thermal radiation characteristics are defined by three variables which are designated in this report as absorptivity (α), reflectivity (ρ), and transmissivity (τ); each term representing thermal radiation that a body absorbs, reflects and transmits, respectively. The mathematical relationship that all three of these parameters share is shown in the equation below:

$$\alpha + \rho + \tau = 1$$

If the radiating body's surface temperature is in thermodynamic equilibrium and the surface has a perfect absorptivity at all wavelengths, it is characterized as a black body. The total radioactive intensity of a black body can be expressed by the Stefan-Boltzmann law:

$$E_b = \sigma \cdot T^4$$

Where σ is Stefan-Boltzmann constant which has a value of 5.67×10^{-8} W/(m^{2}K^4), and T is the absolute temperature in Kelvin. In most cases, a "grey body" is the common scenario that is observed rather than a blackbody. A grey body refers to a radiating body that is not completely in thermodynamic equilibrium and does not have a perfect absorptivity. The total amount of thermal radiation, E_b, emitted by a grey body is given by the equation below:

$$E_b = \varepsilon \cdot \sigma \cdot T^4$$

Where ε is the emissivity of a material, which reflects on the material's ability to emit energy by radiation from its surface.

Heat exchange between the two grey body surfaces (concrete specimen and external heating source) can be illustrated as two very large parallel plates. In the finite element model, the external heating surface is applied as an evenly distributed thermal loading throughout the entire surface of the specimen. The distance between the two bodies,

(external heating source and concrete surface) is relatively small in comparison to the body's surface. Therefore, by using the assumption of the two parallel "infinite" plates (infinitely large surface area compared to an extremely small strip or distance defined as dx between the two body's surfaces) the radiant heat emitted by surface 1 is either absorbed by surface 2 or reflected back to surface 1 in indefinite process. This process can be algebraically expressed and solved for the total radiant energy exchange, Q:

$$Q = \frac{\epsilon 1 - \epsilon 2}{1 - \rho 1 \rho 2} \cdot \sigma (T_1^4 - T_2^4) A$$

Where A is the plate area and the subscripts 1 and 2 represent the two different plate surfaces, shown in Figure 2.1. The emissivity coefficient used in modeling the thermal radiation was obtained by experimental data extracted from the BAM experiment. This heat-exchanged process is implemented in the finite element model by determining the convection heat transfer coefficient, emissivity and conductivity.

2.5 FINITE ELEMENT ANALYTICAL APPROACH

This section introduces the analytical and theoretical approach of finite element models used to simulate and investigate nondestructive testing using infrared thermography on concrete and composite structures.

The finite element software used in this research was Abaqus CAE 6.11-1, which is a commercially available nonlinear finite element analysis program. The analysis procedure of the finite element approach in Abaqus is structured by a division of the "problem histories" into steps. Each step is any suitable phase of the problem history of

the analysis, such as a thermal transient analysis, dynamic transient analysis, structural analysis, and etc. In each step, an analysis procedure is chosen to define the type of analytical method that are performed during the individual segments of the model; in the case of the impulse thermography finite element model, a transient heat transfer analysis was used to replicate the BAM experiment previously performed at the Technical University of Berlin. A transient heat transfer analysis is the change in heat transfer in a given time interval, in which the system is not in thermal equilibrium. The main concern of this model is the temperature change that can be detected on the surface of the specimen. Therefore, the type of transient heat transfer analysis conducted in Abaqus was an uncoupled heat transfer analysis. This type of heat transfer analysis can analyze the temperature fields without the knowledge of the stress and deformation state or electrical field in the bodies being used. The change of temperature over duration of time can be expressed by the transient heat transfer balance equation below:

$$q_x A dt + QAdxdt = \Delta U + q_{x+dx} A dt$$

Where the entire equation above represents the change in energy of the entire system. The group of terms in the equation on the left of the equals sign ($q_x A dt$), represents the heat conduction into the controlled volume; while the second group of terms on the left side of the equals sign ($QAdxdt$), relates to the internal energy or heat source created within the control volume. On the right side of the equation, the first term is the specific heat mass capacity and the last terms in the energy equation is the heat conduction leaving the controlled volume.

In order to simplify the model and shorten the modeling time, a linear finite element heat transfer analysis was performed. Although this experiment has several non-linear material and heat transfer properties, a linear method of analysis was chosen due to the low temperature changes occurring during the BAM experiment and finite element model. The low external heating sources applied to the specimen in the experiment and model only caused a small change in temperature for the specimen. The small change in temperature would have an insignificant effect on the results of the model if a non-linear analysis were chosen. With the small change of temperature fluctuation, a non-linear analysis would not provide more accurate results, such as the case of a drastic temperature change of a, i.e. Structural fire analysis.

2.6 FINITE ELEMENT MODEL

The finite element model consists of the three heat transfer mechanisms which affects the thermal properties of the specimen's ability to allow heat to penetration and diffusion heat through the material body. In addition, the three thermal mechanisms also serve as heat transfer boundary condition in the analysis. The heat transfer mechanisms that were discussed in the previous section (Section 2.4), play an extremely important role in the finite element model presented in this report.

The external heating source was modeled using a uniformly distributed surface heat flux, with instantaneous amplitude for the designated time interval. Only the top and bottom surface areas of the specimen have radiation and convection boundary conditions as specified. The boundary conditions for radiation and convection were defined by the ambient temperature of the surrounding medium and the thermal coefficients for radiation and convection were selected by literature pertaining to concrete thermal

properties. The sides and edges of the specimen were modeled as adiabatic boundary conditions.

The specimen was also modeled in a 3-dimensional modeling space with a defined deformable type of material analysis. In order to create smooth meshing, the concrete specimen was created using several separate parts analytically connected by nodal tie constraints. A nodal tie constraint analytically ties all separated parts into one part. The meshing comprised of small discrete cubic elements, which are discussed in the next chapter. The element type used in this thermal analysis was a diffusive heat transfer 20 node quadratic heat transfer brick (DC3D20).

Table 2.1: Several methods of nondestructive testing evaluation for concrete structures, described by ACI Committee 228.2R-13 manual

Method	Advantages	Limitations
Direct transmission radiometry	Portable equipment available for determination of in-place Density. Minimal operator skill is required.	Operators must be licensed. Available equipment limited to path lengths less than 12 in. Requires access to inside of member or opposite faces
Parallel seismic	Determines whether concrete structure is uniform	Does not distinguish the type of flaw and location of the flaw.
Radiography	Provides view of the internal structure of the object. Use of image plates allows for digital signal processing to extract more information about the internal structure. Tomography of reinforcement in large columns and beams can be achieved.	Operators must be licensed and skilled. It is expensive and difficult to identify cracks and limited penetration.
Covermeter	Able to locate reinforcing bars and other embedded metal objects. Equipment is lightweight, portable, and easy to use. Cover depth can be estimated.	Low accuracy and can only detect ferromagnetic objects. Maximum penetration is limited.
Ground-Penetrating radar	Rapid scanning, very sensitive to embedded metals and ability to penetrate concrete-air interfaces.	Limited to cone-shaped volume for scan. Cracks and necking are not easy to detect.
Impact-echo	Access to only one face needed; equipment is commercially available and capable of locating a variety of defects.	Experienced operator is required and limited member thickness.
Impulse-response method	Determines the location of cracks and constrictions in the concrete structure.	Results interpretation is complex. Similar limitations on geometry of shafts tested as sonic-echo

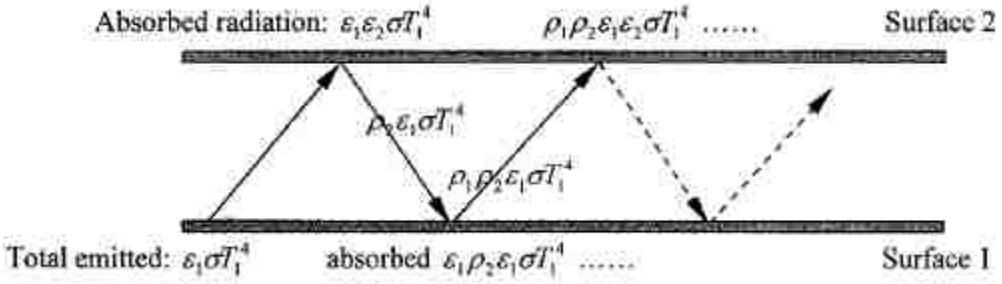

Figure 2.1: Representation of two flat parallel plates with radiation being emitted, absorbed and reflected by both surfaces of the plates (Jun Lee, Pessiki, Kohno, Analytical Investigation of Steel Column Fire Tests, 2006).

CHAPTER 3
BAM EXPERIMENT VERIFICATION

3.1 INTRODUCTION

This chapter presents the verification of the finite element approach used in this research to model infrared thermography. To verify the approach, the finite element models developed are compared with the results of the infrared thermography tests of a concrete block specimen conducted at Technical University of Berlin (TUB) by Wiggenhauser, Hille and Cziesieki (2004). In this report the research and experiments performed by TUB are referred to as the BAM tests.

Section 3.2 of this report explains the background of the BAM test, and includes both a description of the experiments that were conducted along with a presentation of the key results that were found. These results are later used in this research to verify the finite element model approach of infrared thermography.

3.2 BAM TEST SETUP

The BAM test consisted of experimental and analytical studies to evaluate the use of Infrared thermography as a means to detect defects in concrete structures. The experiment consisted of three concrete specimens each consisting of the same dimensions, but with different internal defects and abnormalities within the concrete subsurface.

Although three concrete specimens were tested in this experiment, only one of the tests conducted was used in this report and research to validate the finite element model

(shown in Figure 3.1). The experiment consisted of a concrete block measuring 1.5 m X 1.5 m X 0.5 m. Within the concrete subsurface, the defects were made by casting polystyrene foam blocks into the concrete. The concrete specimen consisted of eight defects which are simulated voids made by the polystyrene blocks. The defects were grouped into two different sizes; one group consisted of a 20 cm x 20 cm x 10 cm cubic defects and the other consisted of 10 cm^3 cubic defects The defects are located at four different depths, which are 0.02 m, 0.04 m, 0.06 m and 0.08 m from the top of the concrete surface on the side facing the external heating source.

Figure 3.2 is a photograph of the test hardware and concrete specimen tested. As shown in Figure 3.2, the tests were performed using three radiators each having up to 2,400 watts of power. The heating process was done dynamically with the three radiators longitudinally arranged as shown in Figure 3.2. The radiators move repeatedly at speeds of .12 meters per second over the length of the concrete specimen. They are aligned uniformly parallel to the arrangement of larger surface area of the concrete specimen, moving in the direction from left to right at about 15 cm from the specimen's surface. The infrared camera used in the experiment was a ThermaCAM SC1000. The features of the ThermaCAM SC2100 unit include a focal plane array detector consisting of a 256 by 256 detector elements and its own computer operational system. Other specifications for the infrared camera used can be found on Table 3.1.

In order to sustain a controlled experimental environment, the experiment was conducted in a temperature-controlled room, with a recorded heating time, heating temperature, air temperature, and humidity. The recorded data was then entered into computer software for analysis processing. The infrared camera was positioned at a

distance of 2.8 m away from the concrete surface and was at a measured height of 0.82 m from the ground, allowing the image to capture the entire concrete specimen.

3.3 BAM TEST PROCEDURE

The temperature-time curves of a reference point located in a region away from the flaw (defect) and a point cursor directly over the center of the flaw (defect) were compared. Furthermore, the temperature difference curve (the difference between the reference point temperature and the temperature directly over the void) was calculated in order to locate the maximum temperature difference at a given time in the experiment. The purpose of evaluating the temperature at the surface in respect to time is because the other influencing parameters such as geometry and material characteristics are held constant in this experiment. Thus, the largest dependencies on the results are reflected upon by the defect's depth, heating duration and heating temperature, which are all reflected in the surface temperature versus time curve.

The concrete specimen surface temperature was measured at 6 different heating durations of 300, 600, 900, 1800, 2700 and 3600 seconds. The experiment consisted of a constant heating temperature with a heat flux of 1250 W/m, applied to the concrete specimen. After the heating process was completed, the experiment followed a two-hour cooling process. Figure 3.4 shows two of the thermograms corresponding to the concrete specimen with a heating duration of 900 seconds. The two thermogram images of the concrete specimen also have different cooling durations from which the surface temperatures were recorded. In Figure 3.4, the thermogram on the left represents the specimen at 485 seconds after the end of the heating phase and the thermogram on the right represents 2445 seconds after the end of the heating phase.

The defects are identified by a temperature contrast on the surface over the areas of the defects as shown in the Figure 3.4. The image on the left has a noticeably good temperature contrast color on the surface, meaning it is most likely a near-surface defect. However, unlike shallow defects, the deeper defects are not clearly visible at shorter cooling times. The image on the right is a concrete specimen with a longer cooling duration of 2445 seconds. The image with the longer cooling duration allows one to see the deeper defects within the concrete subsurface more clearly on the thermogram images. Based on the two images shown on Figure 3.4, it can be deduced that a longer cooling period allows deeper defects to be seen more clearly in thermographic images. This phenomenon is discussed in later sections of this report.

The results of the experiments were evaluated by graphing surface temperature versus time over a reference point and directly over the center of a designated defect (shown in Figure 3.4). The temperature difference between both graphs were then created and graphed as the change in surface temperature versus time; showing the maximum temperature difference ($T_{max\Delta}$) in respect to time ($t_{max\Delta}$) of its occurrence. The graphical representations of the results are shown Figure 3.5 for Defect 2 and Figure 3.6 for Defect 5. Figure 3.5 illustrates the BAM test results using three graphs, Defect 2 temperature vs. time curve; reference point 1 temperature vs. time curve; and, the corresponding difference between Defect 2 and reference point 1 temperature vs. time curve. Likewise, Figure 3.6 illustrates Defect 5 temperature vs. time curve, reference point 5 temperature vs. time curve, and the corresponding difference between Defect 5 and reference point 5 temperature vs. time curve. Figure 3.5 and Figure 3.6 show the surface temperatures at the left side of the graph and a surface temperature difference scale between the defect and reference point, at the right side of the graph.

3.4 CAUSE OF SURFACE TEMPERATURE CHANGE

The basic concept of how surface anomalies occur during impulse thermography starts when the external heating source creates a change in temperature on the surface of the specimen. The change of temperature excites the intermolecular particles of the material creating thermal energy in the form of radiation, which propagates to the surface of the specimen. The process of heat transfer in and out of the specimen is caused by thermal conduction, convection and radiation. Thermal diffusivity is a property that measures the thermal inertia or a substance ability to allow heat to move through it, contributing to the time factor of which heat is transferred throughout the specimen. During the cooling process, thermal energy is released through radiation, convection and conduction at a rate defined by the materials thermal diffusivity and other thermal properties. Thermal diffusivity is mathematically defined by the equation shown below:

$$\alpha = \frac{k}{\rho c_p}$$

Where α is the thermal diffusivity, k is the thermal conductivity, ρ is the density and c_p is the specific heat capacity.

During the heating phase, the presence of a subsurface defect and/or abnormality can reduce or increase the diffusion rate. This could cause the surface temperature near or over the subsurface defect and/or abnormalities to emerge as an area of higher or lower temperature with respect to the surrounding areas. Consequently, the change in the diffusion rate causes an accumulation of heat, and creates a higher surface temperature

above the subsurface defect. Moreover, this phenomenon occurs later for deeper defects and with a much more diluted thermal contrast on the surface.

3.5 BAM TEST RESULTS

The results of the BAM test are shown in Table 3.2. The results are displayed by the maximum temperature difference at a given time for six different heating times and eight different defects. The maximum temperature difference shown on the table is the recorded difference between the defect's maximum temperature and the corresponding reference point maximum temperature (i.e. Defect 2 vs. reference point 2). The experimental results shows several consistencies with the varying heating times and defect depths. If the eight defects are classified into two subgroups, one being the larger size defects of 20 cm x 20 cm x 10 cm (Defects 1-4) and the other four defects with the dimensions of 10 cm x 10 cm x 10 cm (Defects 5-8), we can then easily compare the results of each group; only comparing the impact on the depths of the defects within each subgroup.

As anticipated, both subgroups showed the maximum temperature difference decreasing with the increasing depth of the defect. Similarly, the occurrence of the maximum temperature at a given time increases along with the increasing heating times of the experiment. The defects in this experiment were filled with polystyrene blocks, which is a material with a significantly lower thermal diffusivity and thermal mass in comparison to concrete. This decrease of thermal mass and diffusivity causes the polystyrene defects to absorb and release thermal energy at a quicker rate than the surrounding concrete material, causing an increase in temperature within the area of the defect. In effect, heat accumulation within the area of the polystyrene can be seen on

the surface during the infrared thermography test. The experimental results show a large heat accumulation on the concrete surface over the regions of the defects during the heating and cooling process as expected.

The larger defects (Defect 1, Defect 2, Defect 3 and Defect 4) in comparison to the smaller defects (Defects 5, Defect 6, Defect 7 and Defect 8) at coinciding depths (such as Defect 4 and Defect 5 both located at a depth of 8 cm) should have a larger surface temperature change. This is expected due to the increase of the defect's area, which has a much lower thermal mass than the surrounding concrete material. The decreases in surface temperature change with respect to the increase of the depth of the defects are also due to the increase of thermal mass as you approach the lower depths of the deeper defects. The results obtained from the experiment remained constant throughout all of the results apart from Defect 7, which did not follow the common characteristics of the other seven defects. Defect 7 had an unusually high surface temperature, which suggests that experimental or human error may have been present in the results for this defect.

3.6 IMPULSE THERMOGRAPHY EXPERIMENT FINITE ELEMENT MODEL

The finite element model created to simulate the BAM test defects followed the finite element approached discussed in Chapter 2. The concrete block contained eight defects all filled with polystyrene blocks. The model was created using 3-dimensional parts with identical dimensions and material properties as shown in Figure 3.7, Figure 3.8 and Figure 3.9. The polystyrene parts are placed into the defects inside of the concrete part and the surfaces of both parts are then connected together through a tie

constraint. This allows the thermal energy to distribute through the concrete and the polystyrene parts as one entire body, but with different thermal properties. In order to create different defect depths in the concrete block, several layers on the top of the concrete block was created as separate parts, and were later tied back to the concrete specimen once the polystyrene blocks were placed into the different depths of the defects .

There were three analytical steps performed in this analysis: step one was the initial conditions; step two was the heating phase; and step three was the cooling phase of the analysis. During the first step, a time duration of zero was selected and an initial ambient temperature of 20 ^{0}C was defined for the concrete specimen and its surrounding. At the second phase, a surface heat flux (q) was applied to the top surface of the concrete specimen in the z-direction for the specified heating duration. There was one heating duration of 900 seconds. The applied thermal heat flux was uniformly distributed with an instantaneous and constant load of 1250 $Js^{-1}m^{-2}$, shown in Figure 3.10. The thermal heat flux simulates the radiators used in the experiment, which was used as the heating source. Also introduced in this phase are two thermal surface interactions. The surface interactions created were radiation and convection. These surface interactions mainly acted as boundary conditions from which thermal energy is absorbed and released from. The thermal interactions during this step were only applied to the bottom of the concrete specimen (opposite and parallel to the surface of where the heat flux is being applied). The surface interactions were not applied to the top surface where the surface heat flux was applied because Abaqus automatically applies thermal convection and radiation to a surface where the thermal heat flux is being applied. The sides of the concrete block are modeled as adiabatic boundary conditions, in order to simplify the heat transfer model. The defects are located at a considerable distance

from the block edges, so heat losses from the sides and corners of the specimen do not influence the surface temperature at the locations of the defects. The final step in the analysis was the cooling phase. In this step the surface heat flux is deactivated and the same surface interactions continue to propagate. Due to the deactivation of the heat flux on the top surface of the concrete specimen, the thermal radiation and convection surface interactions are then applied to the top surface of the concrete, with identical thermal parameters as the bottom surface interactions.

3.7 FINITE ELEMENT MODEL CONVERGENCE STUDIES

This section discusses the convergence studies conducted for the finite element model created in Abaqus. Both h-and p-convergence studies were performed. These two methods are shown in Figure 3.11. Both methods are used to improve the accuracy of the solutions obtained in the analysis. The objective for this convergence study is to refine the mesh to obtain the necessary accuracy by using only the required amount of degrees of freedoms. The h-convergence pertains to the geometric discretization and the elements basic shape function. While the p-convergence refers to polynomial equation used to determine the certain degree of accuracy required by the user. Both convergence studies were done by altering the characteristic of the element sizes, shapes and the amount of nodes defined in each element. The characteristics of the convergence study parameters were selected based on the concrete specimen's relatively large thickness in comparison to the depth of the temperature gradient penetrating through the concrete during the analysis. A finer mesh is necessary in order to ensure that the temperature distribution and gradient is similar to the experimental temperature diffusion through the concrete block; this could only be done by comparing

the surface temperature of the model and experiment, until reasonable values were obtained.

3.7.1 Parameters

For the h-convergence study, Figure 3.12 is a display of the meshes used for the concrete specimen. There were three different size meshes used for the convergence study. The three sizes were categorized as intermediate mesh (Mesh 1), a coarse mesh (Mesh 2) and a very fine mesh (Mesh 3). The meshes were generated by increasing or decreasing the number of elements throughout the concrete specimen, with Mesh 2 containing the least amount of elements and Mesh 3 containing the largest number of elements.

Figure 3.13 illustrates the two different types of elements used in the p-convergence study. The 8 node linear heat transfer element shown on the left in Figure 3.13 is a first order element, with a temperature variation that is algebraically defined as a linear equation over the elements nodes. The other element used in this study was a 20-node quadratic heat transfer element shown on the right in Figure 3.13. The 20-node quadratic heat transfer element is a second order element in which the temperature can vary parabolically between the element nodes.

The polystyrene foam parts shown in Figure 3.9 were meshed using one geometric and nodal element size since the parts were extremely small in comparison to the entire concrete model. Using a finer mesh would have increased the duration of the running time of the finite element model, and would still not have an impact on the temperature

gradient through the parts due to their small size in comparison to the entire concrete specimen. Table 3.4 summarizes the parameters discussed in the previous section.

3.7.2 Results of convergence study

Figure 3.14 shows the temperature vs. time relationship at the surface of the specimen exposed to the external heating source for an 8-node linear heat transfer element. This is shown on the plot for Mesh 1, Mesh 2, and Mesh 3.

Likewise, Figure 3.15 shows the temperature vs. time relationship at the surface of the specimen exposed to an external heating source for a 20-node quadratic heat transfer element.

Figure 3.16 contains the graphs of all of the measured temperature vs. time curves for both the linear and quadratic nodal elements.

The results graphed for the 8-node linear elements are shown in Figure 3.14. The figure shows a maximum surface temperature difference of approximately 5 ^{0}C. The finer mesh (M3-1) reflects a higher temperature on the surface of the concrete specimen, when compared to the more coarse mesh. This increase in surface temperature when analyzing the finer mesh corresponds to the capability of the temperature distribution from the external heating source to penetrate and diffuse through the elements more effectively.

The results graphed for the 20-node quadratic elements, shown in Figure 3.15, shows a small difference in temperature in the three different meshes graphed. The maximum

temperature difference between the three meshes was approximately 2 ^{0}C, occurring at the end of the analysis. This shows that the h-convergence parameter does not have a significant impact on the results obtained in the finite element model (FEM), when a higher degree polynomial convergence parameter is used.

Figure 3.16 contains all of the graphs created in this convergence study in order to get a better understanding of how all of the h-convergence and p-convergence parameters affect the finite element model results. In Figure 3.16 the graphs M2-1, M1-1 and M1-2 all show a variance in the temperature versus time curves in comparison to the relatively consistent graphs M2-2, M3-1, and M3-2. This discrepancy in temperature is mainly shown where the h-convergence parameter (meshing) is a coarse larger element sizes. This is also true to the linear p-convergence parameter, where a finer mesh size is not used to over confiscate the less accurate linear analysis method.

The convergence study performed showed a convergence in the surface temperature as the gradual increase in a more precise method of solutions was used in the model. Therefore to obtain the most accurate results from the model, a 20 node quadratic heat transfer brick (DC3D20) element was used. The element size and meshing used to model the concrete specimen was similar to that of M3-2.

3.8 BAM MODEL RESULTS AND CONCLUSION

The results of the BAM model were graphed for each of the defects, using a temperature versus time plot. The heating duration used in this analysis was 900 seconds and the measured temperatures were taken at the surface directly above the center of each defect. Each figure contains three graphs, the temperature of the surface above the

defect, the designated reference point surface temperature, and the difference in temperature of the defect and reference point.

The results of the finite element model analysis are graphed on Figure 3.17 through Figure 3.24, corresponding to Defects 1 through Defect 8, respectively. The finite element results have been graphed for each defect, showing the temperature versus time curve in respect to 900 seconds of heating time. In each graph, the designated reference point (corresponding to each defect) is also graphed along with the difference curve, which shows the change in temperature on the surface of the specimen over the defect. The figures show the surface temperature of the specimen on the left side of the graph, and on the right side is the temperature difference between the defect and reference point.

Table 3.3 shows the results of the impulse thermography finite element model and the experimental results of the BAM test. The results shown consist of the maximum temperature change after the heating phase of the experiment (900 seconds heating duration) and the time at which the maximum change in surface temperature occurred (difference between the reference point temperature and defect temperature).

Comparing the values of the temperature change from the BAM test and finite element analysis Defect 1, Defect 2 and Defect 3 (which are three deepest larger defects), the data shows a very similar temperature changes and time occurrence of their maximum temperature change.

Defect 4 and Defect 5 are the defects closest to the surface of the concrete. Comparing the experimental and analysis results for these defects, the BAM model results yield a

much higher surface temperature change occurring at an earlier time after the heating phase ends.

Defects 6, 7 and 8 are the deepest and smaller sized defects. The results show that these defects have a higher surface temperature change in the BAM test in comparison to the finite element model results. The BAM test results also have shorter time duration to reach the maximum temperature change for Defect 6, Defect 7 and Defect 8. Figure 3.17 through Figure 3.24 show that, for the deeper defects at 60 mm and 80 mm, there is little difference between the surface temperatures over the defects and the reference surface temperature. This is the case for the defects at 60 mm (Defect 2 and Defect 7) and the defects at 80 mm (Defect 1 and 8). This result from the finite element analysis does appear to have error. For example, the experimental results for Defect 5 shown in Figure 3.6 reveal a difference in the surface temperature over the defect and the reference surface temperature, throughout the experiment (compared to the BAM model results shown in Figure 3.21).

Based on the results shown on Table 3.3, the data obtained from the finite element model can be perceived to have some discrepancy in the maximum temperature change and time of occurrence for five of the different defects.

However, the important aspect from the data shown on Table 3.3 is the analogous behavior between both the model and the experiment data recorded. When investigating the defects maximum temperatures in both analyses, the defects closest to the surface yield the larger change in temperature and the shortest time at which the maximum temperature difference occurred. Also noted, as the depth of the defect increased, both cases show the same relative change in maximum temperature

difference variation. This consistency of the model and experimental results can be observed for the change in the defect size and location. This shows that the model and experimental results both coincide with one another.

Table 3.1: Specifications and details of ThermaCAM SC1000 infrared camera (Wiggenhauser, Hille and Cziesieki 2004)

Spectral	3.4 to 5.0 microns
Temperature Range	-10 To +450 ° C
Temperature resolution	.07 K at 30 ° C.
Accuracy	± 2% and 2 K
Frame rate	50 Hz (PAL) Full Screen
Dynamic range for each measurement point	12-bit
Spatial resolution (IFOV)	1.2 mrad
Field of view with standard lens	17 ° x 16 °

Table 3.2: Representation of the recorded temperature difference between the reference point surface temperature and defect surface temperature from the BAM experiment (Wiggenhauser, Hille and Cziesieki 2004)

Heating Duration	300s		600s		900s	
Defect	ΔT_{max}(K)	$t\Delta_{Tmax}$(sec)	ΔT_{max}(K)	$t\Delta_{Tmax}$(sec)	ΔT_{max}(K)	$t\Delta_{Tmax}$(sec)
1	0.2	3860	0.7	3700	0.7	3125
2	0.4	2835	0.9	2645	1.5	2445
3	0.8	1945	1.7	1545	2.3	1485
4	1.7	1135	3.5	1055	4.7	940
5	1.4	600	2.7	525	3.5	485
6	1.2	735	2.1	600	3.0	585
7	2.2	385	4.0	290	5.5	280
8	1.0	885	1.8	765	2.6	605
Heating Duration	1800s		2700s		3600s	
Defect	ΔT_{max}(K)	$t\Delta_{Tmax}$(sec)	ΔT_{max}(K)	$t\Delta_{Tmax}$(sec)	ΔT_{max}(K)	$t\Delta_{Tmax}$(sec)
1	1.4	2915	2.0	2630	2.4	2570
2	2.6	2100	3.5	2045	4.3	1575
3	3.7	1375	5.4	1290	6.0	1175
4	8.4	655	-	-	-	-
5	5.4	325	6.6	300	7.3	285
6	4.8	390	6.1	330	6.9	295
7	8.5	160	-	-	-	-
8	4.1	515	5.8	370	6.4	350

Table 3.3: Defects maximum surface temperatures differences for the BAM experiment and BAM finite element model

Defect	BAM EXPERIMENT ΔT_{max}(K)	BAM MODEL ΔT_{max}(K)	BAM EXPERIMENT $t\Delta_{Tmax}$(sec)	BAM MODEL $t\Delta_{Tmax}$(sec)
1	0.7	0.68	3125	3300
2	1.5	1.37	2445	2420
3	2.3	3.2	1485	1320
4	4.7	9.6	940	330
5	3.5	6.8	485	220
6	3	1.6	585	880
7	5.5	0.55	280	1760
8	2.6	0.23	605	2860

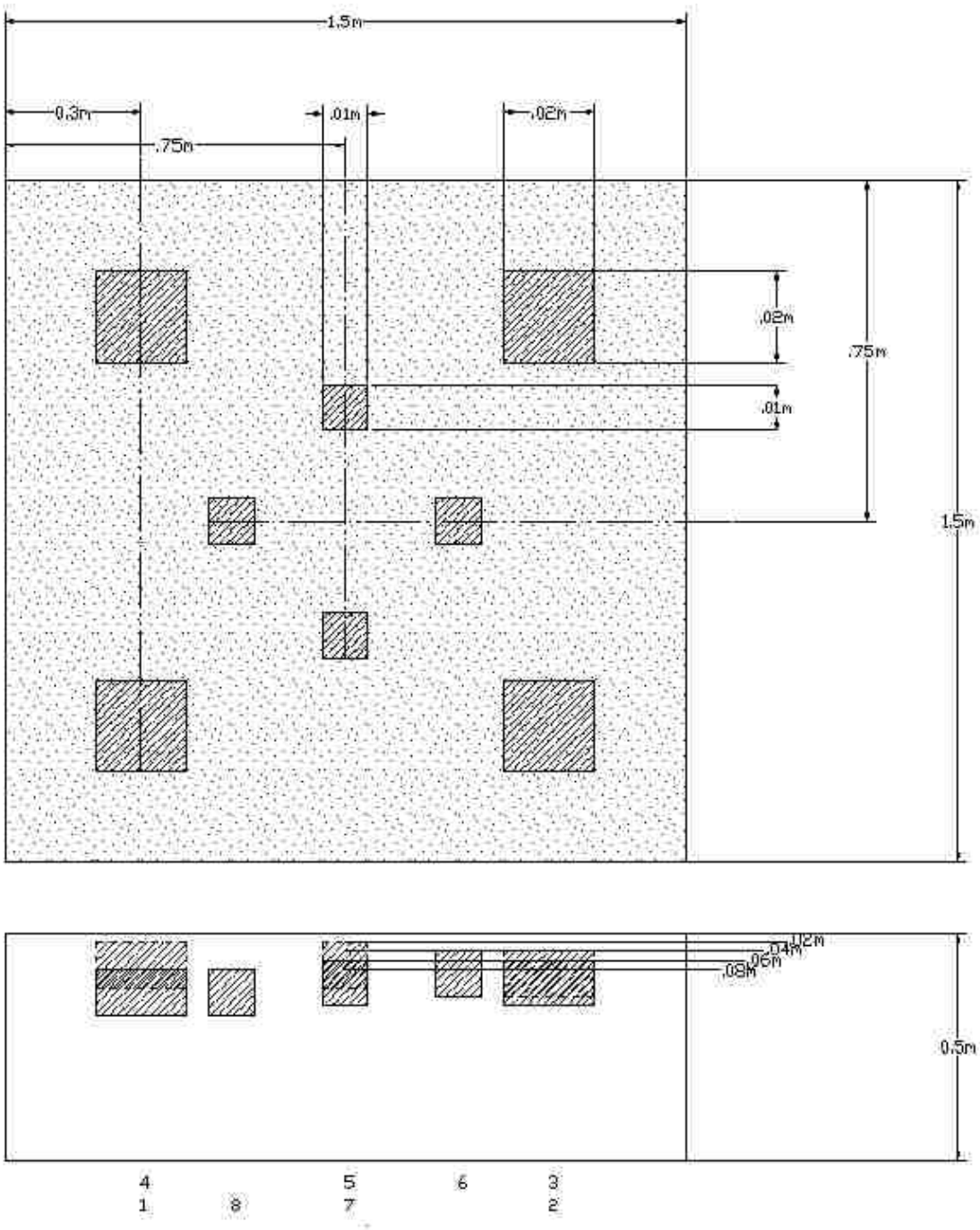

Figure 3.1: Dimensions and defect identification numbers of the concrete specimen used in the BAM experiment and finite element model (drawing not to scale)

Figure 3.2: Experimental Setup of BAM experiment, including the concrete block specimen, the radiator, the infrared thermography camera and the computer unit (Wiggenhauser, Hille and Cziesieki 2004)

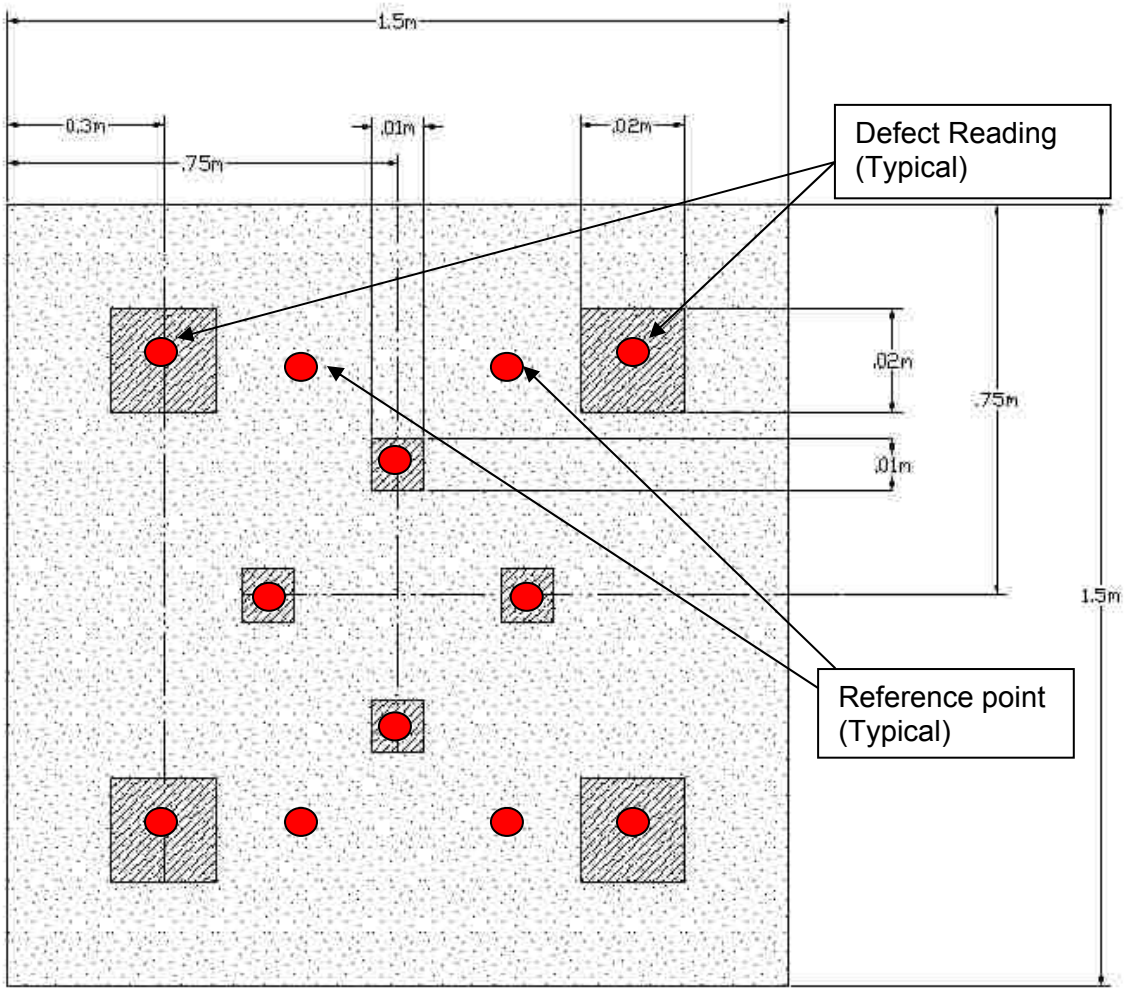

Figure 3.3: Elevation view of concrete specimen FEM model, with the corresponding reference points and defect location

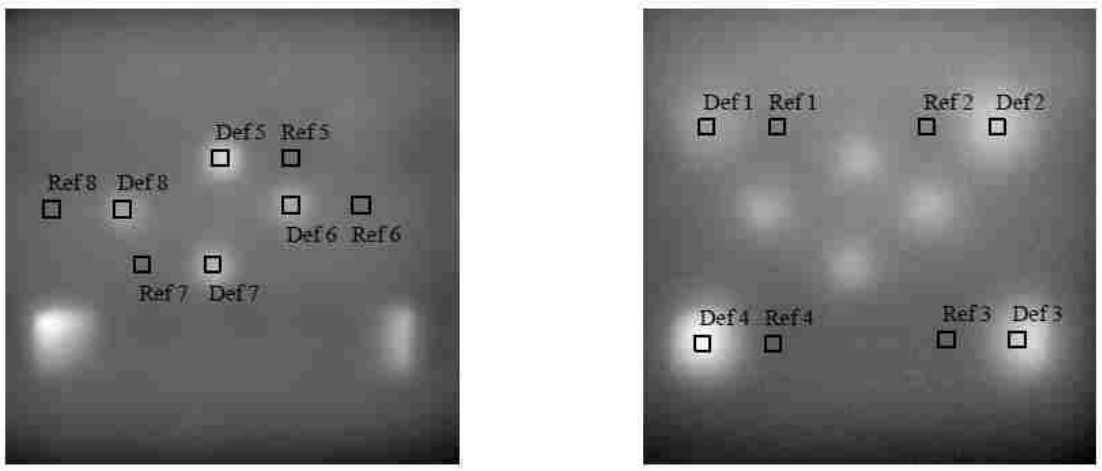

Figure 3.4: Thermogram images of concrete specimen during the cooling phase at 485 seconds (left) and 2445 seconds (right) after heating the concrete specimen for duration of 900 seconds (Wiggenhauser, Hille and Cziesieki 2004)

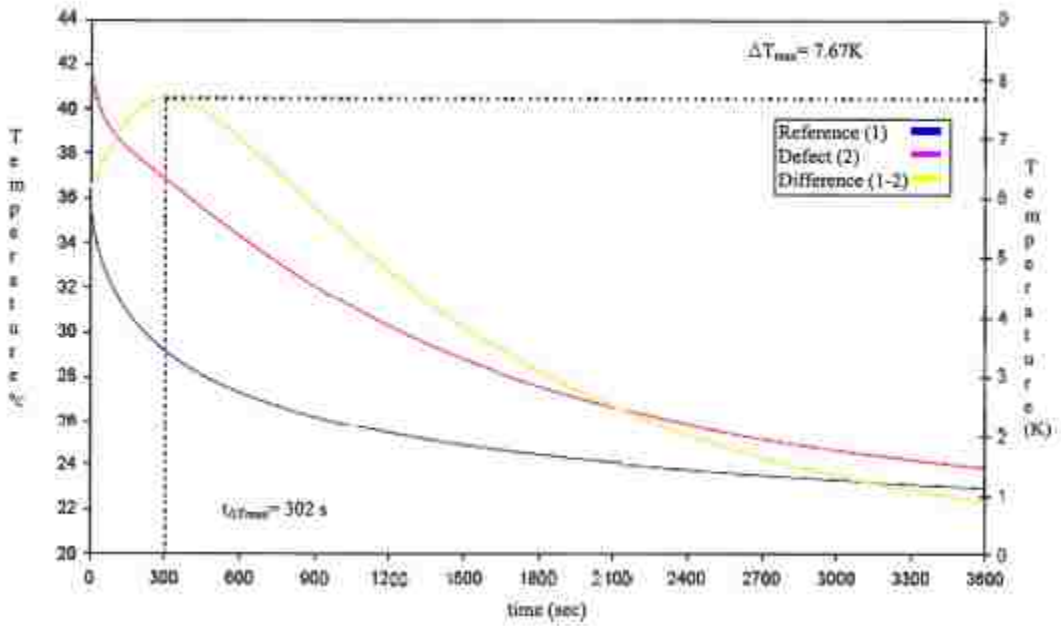

Figure 3.5: BAM test results for Defect 2 and reference point 1, temperature vs. time curve (Wiggenhauser, Hille and Cziesieki 2004)

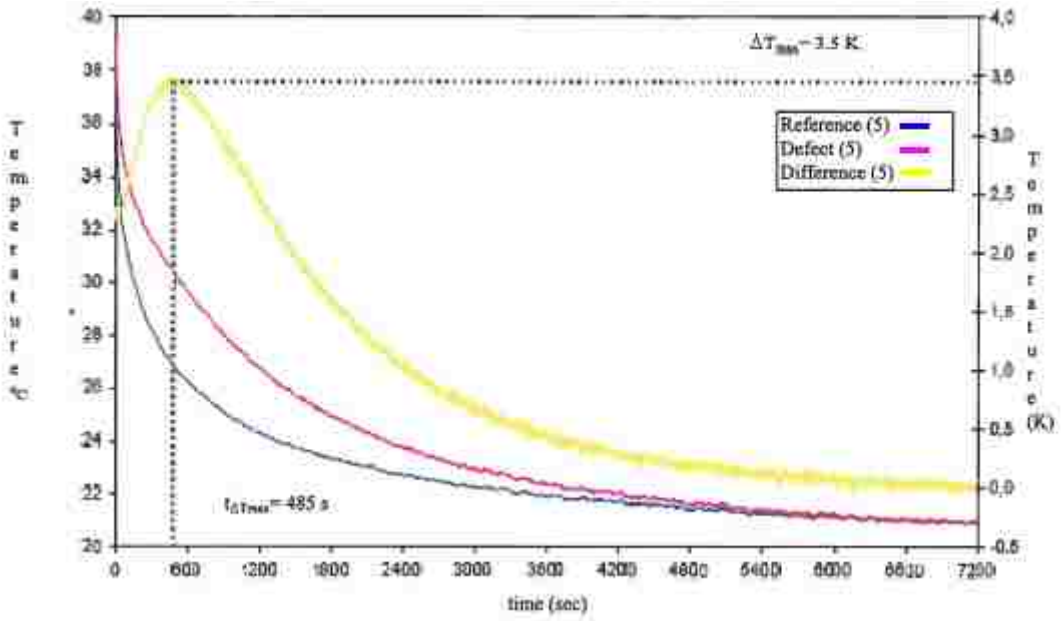

Figure 3.6: BAM test results for Defect 5 and reference point 5, the temperature vs. time curve (Wiggenhauser, Hille and Cziesieki 2004)

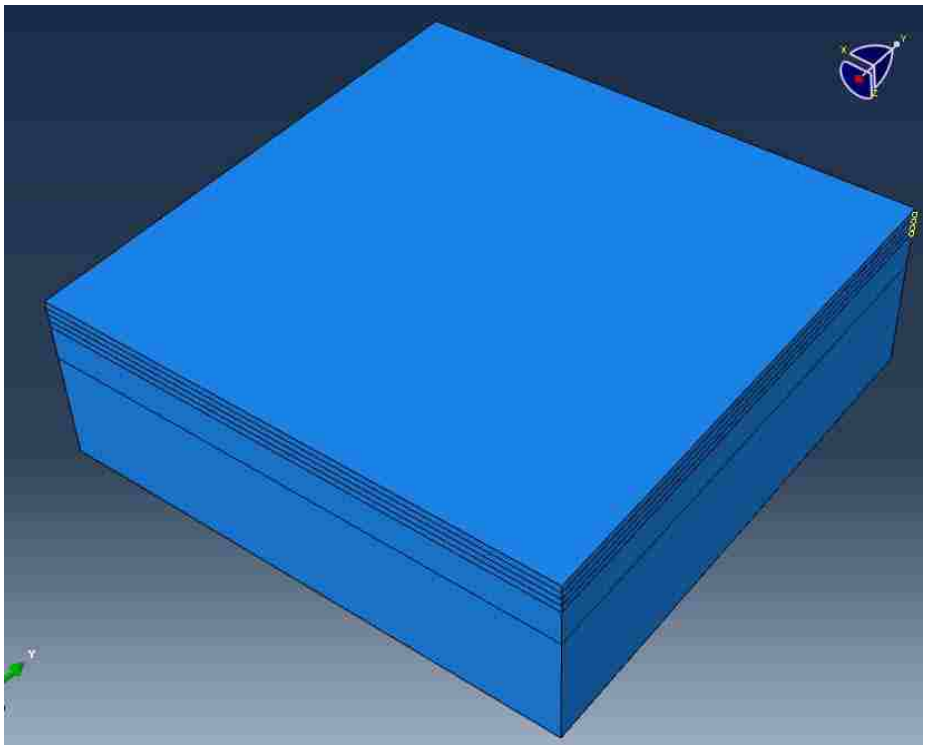

Figure 3.7: Finite element model of the concrete specimen as a 3 Dimensional part

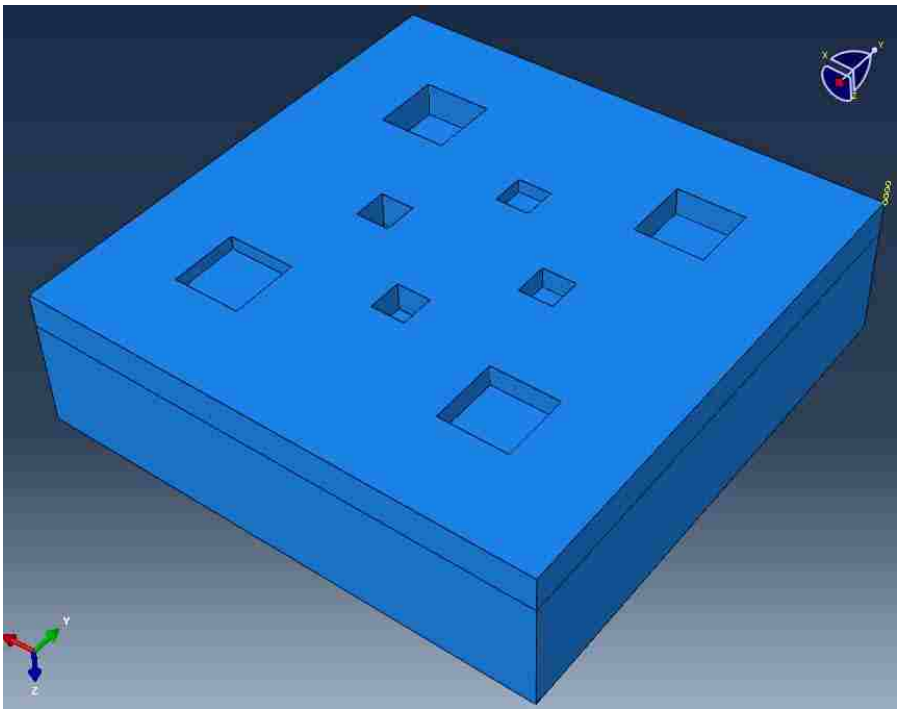

Figure 3.8: Finite element model of the concrete specimen showing the top 3 cm of the concrete remove to view of the defects

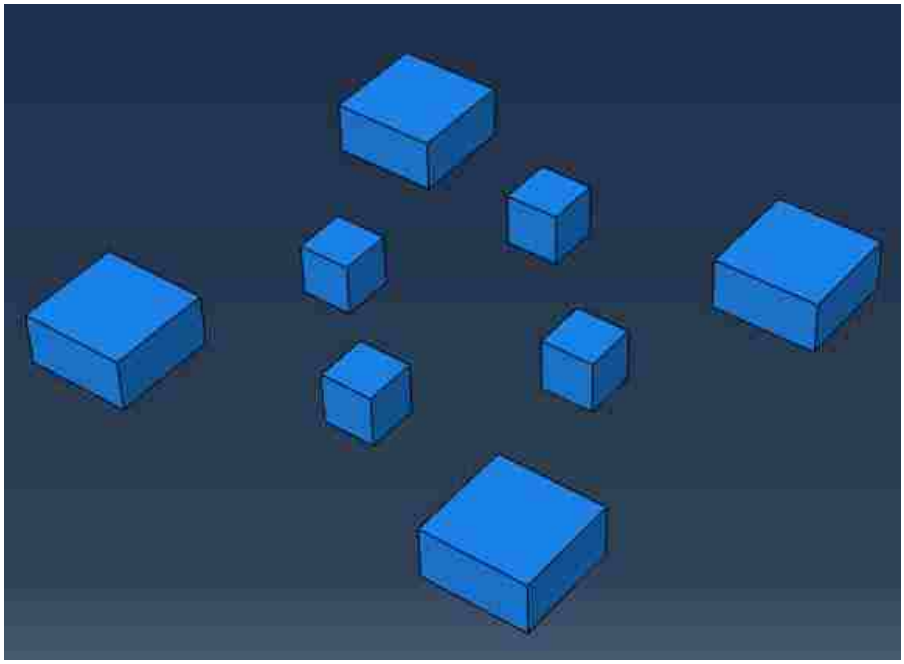

Figure 3.9: Finite element model of polystyrene blocks (defects within the concrete specimen filled into the defects)

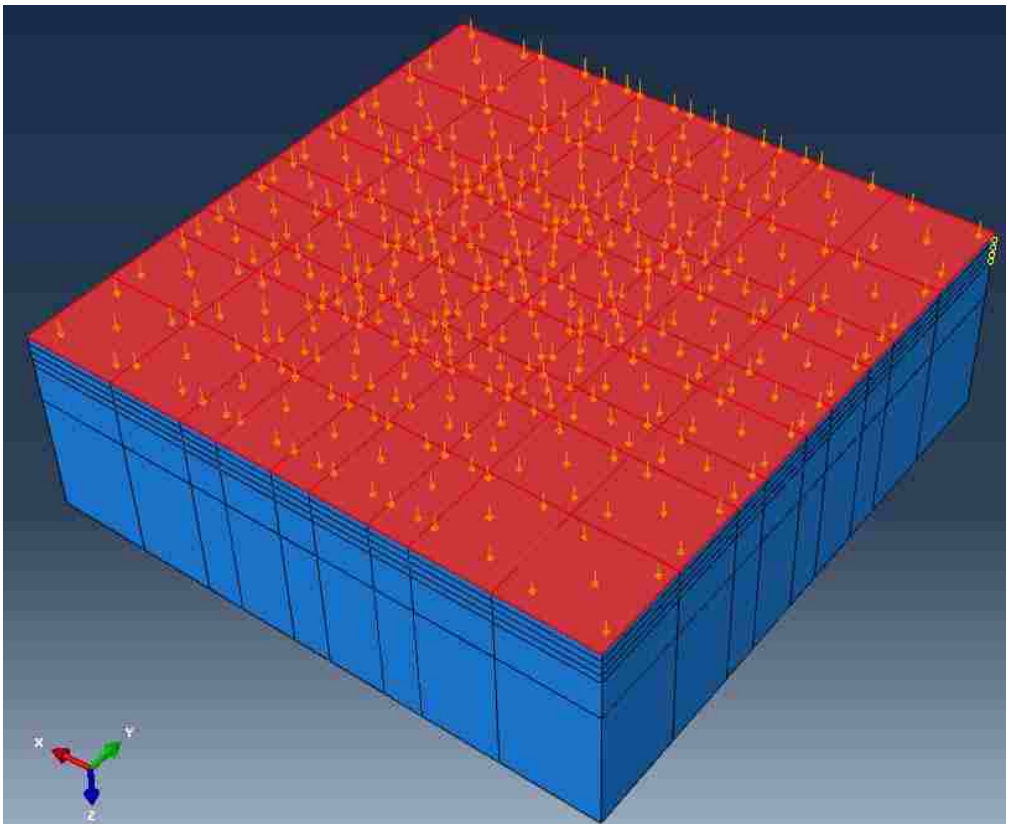

Figure 3.10: Applied thermal heat flux uniformly distributed at 1250 $Js^{-1}m^{-2}$ on the surface of the concrete specimen

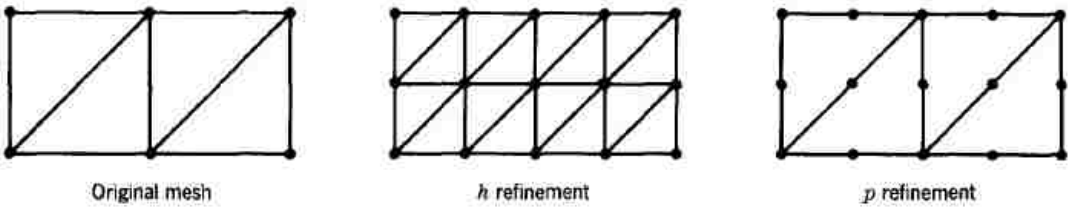

Figure 3.11: Refinement of finite element mesh using h-convergence and p-convergence method

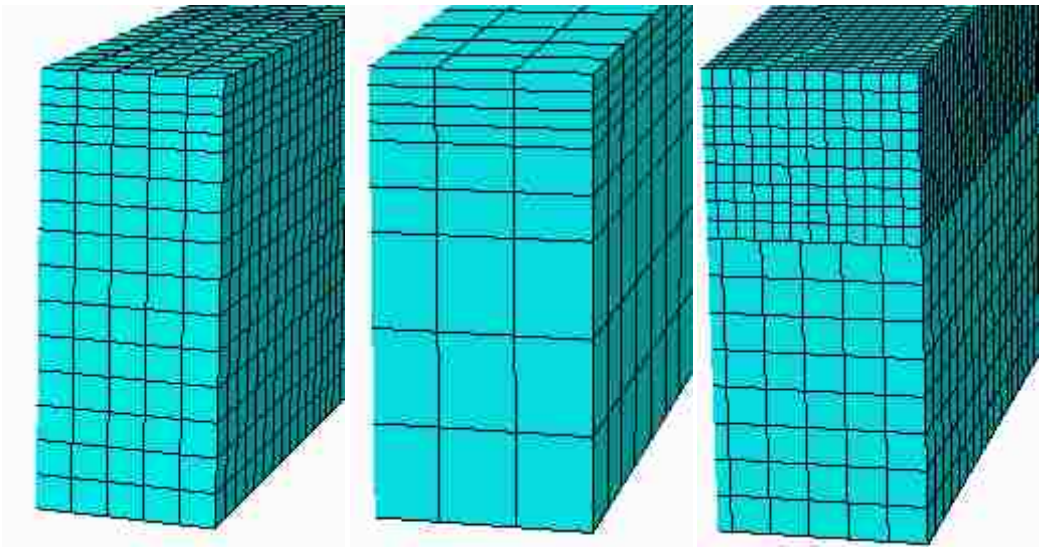

Figure 3.12: The h-convergence studies for the concrete finite element model, with the three different mesh sizes

Figure 3.13: Representations of the two types of p-convergence methods used in this study. The 8 node linear heat transfer element shown on the left and the 20-node quadratic heat transfer element shown on the right.

Table 3.4: Convergence study analysis matrix for the concrete specimen finite element analysis.

Designation	Mesh	Element Type
M1-1	Mesh 1	8-node linear element
M2-1	Mesh 2	8-node linear element
M3-1	Mesh 3	8-node linear element
M1-2	Mesh 1	20-node quadratic element
M2-2	Mesh 2	20-node quadratic element
M3-2	Mesh 3	20-node quadratic element

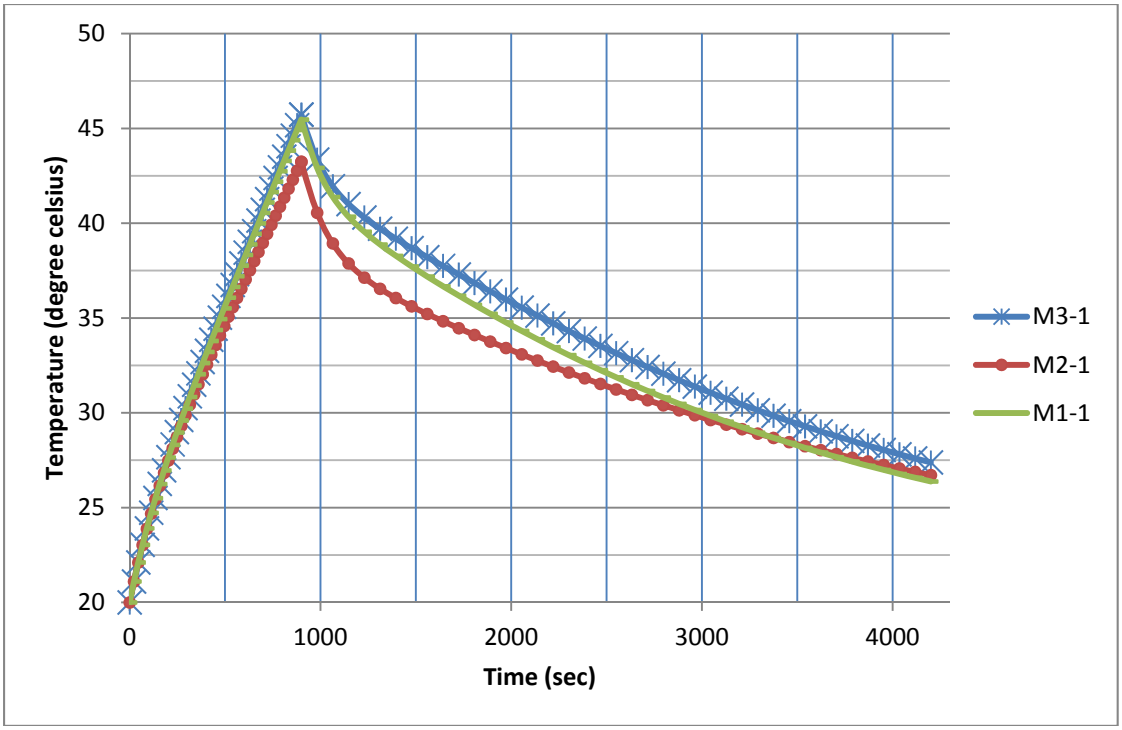

Figure 3.14: Convergence study results for the surface temperature of concrete specimen during the finite element analysis, using 8-node linear elements

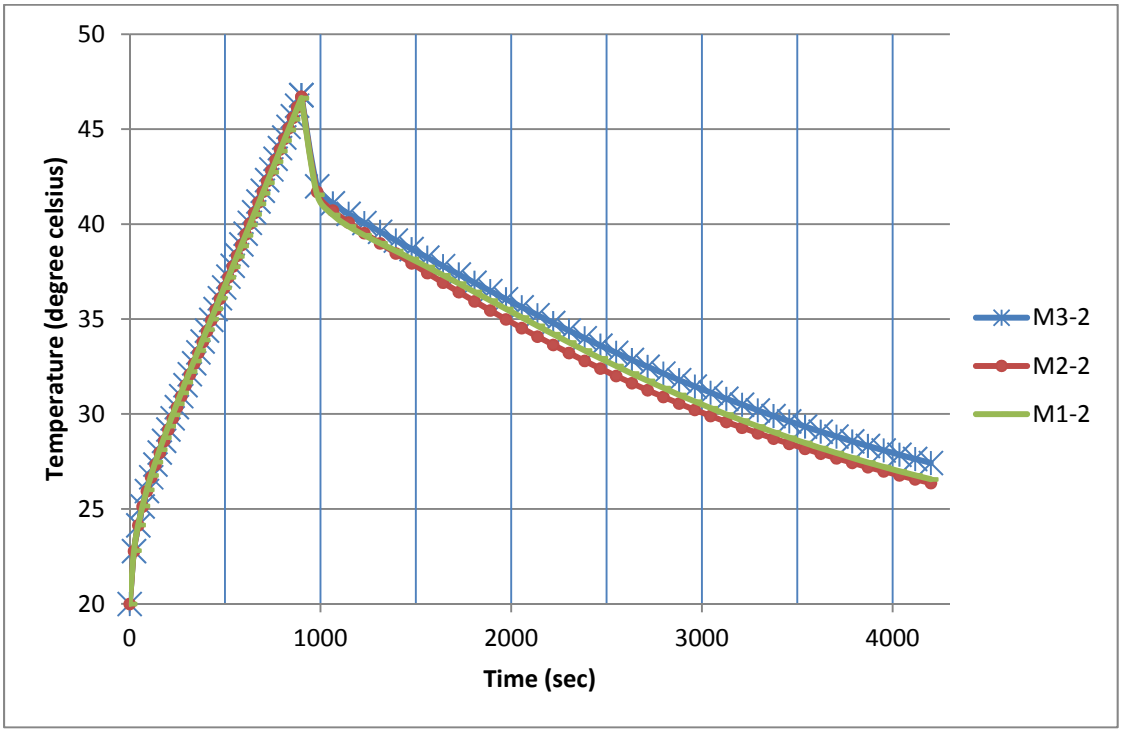

Figure 3.15: Convergence study results for the surface temperature of concrete specimen during the finite element analysis, using 20-node linear elements

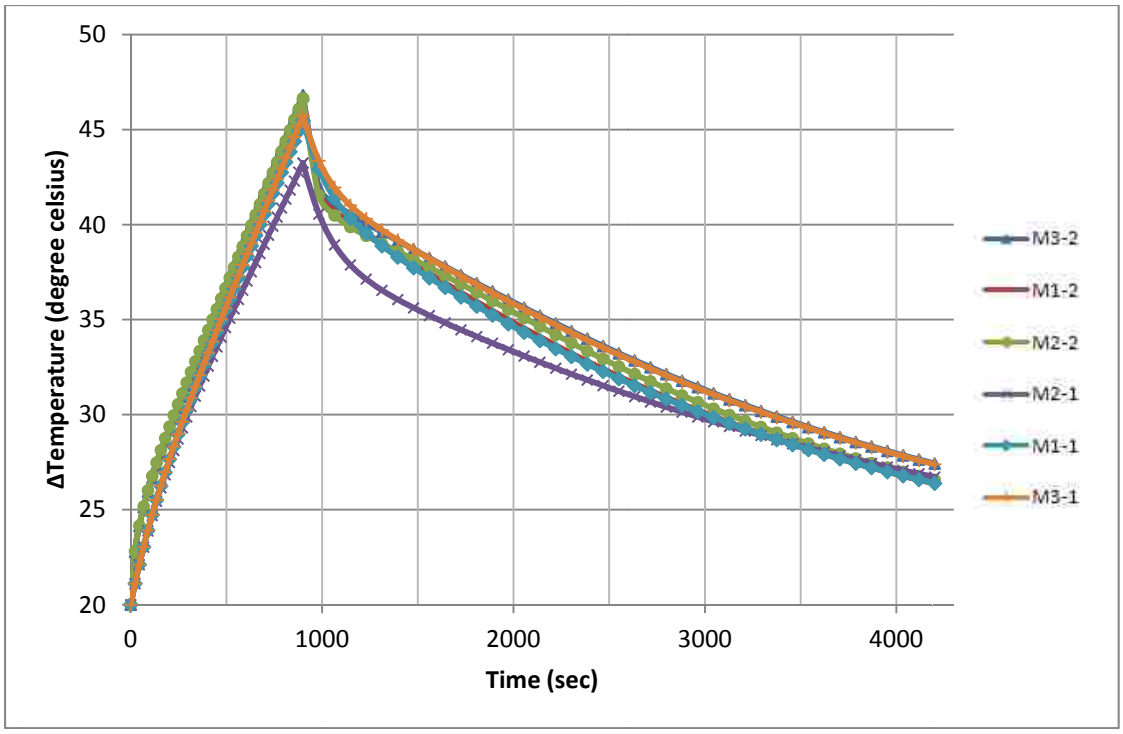

Figure 3.16: Convergence study results for the surface temperature of concrete specimen during the finite element analysis for the 8 node elements and 20 node elements

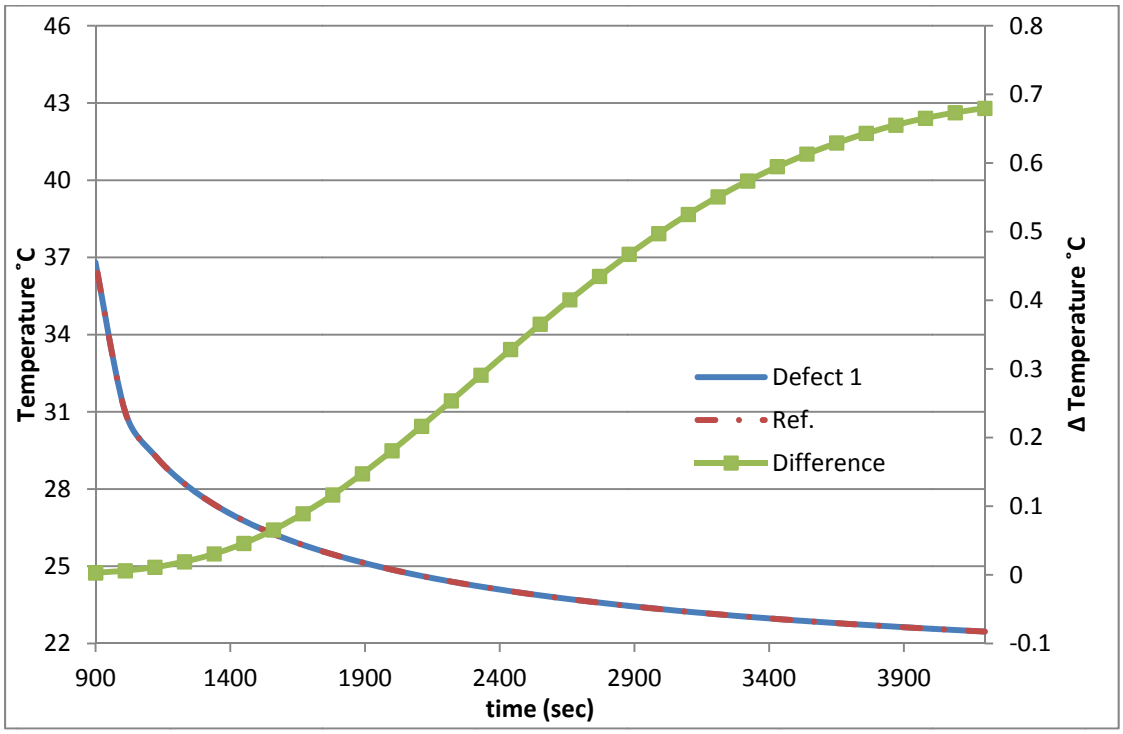

Figure 3.17: Defect 1 surface temperature versus time FEM results

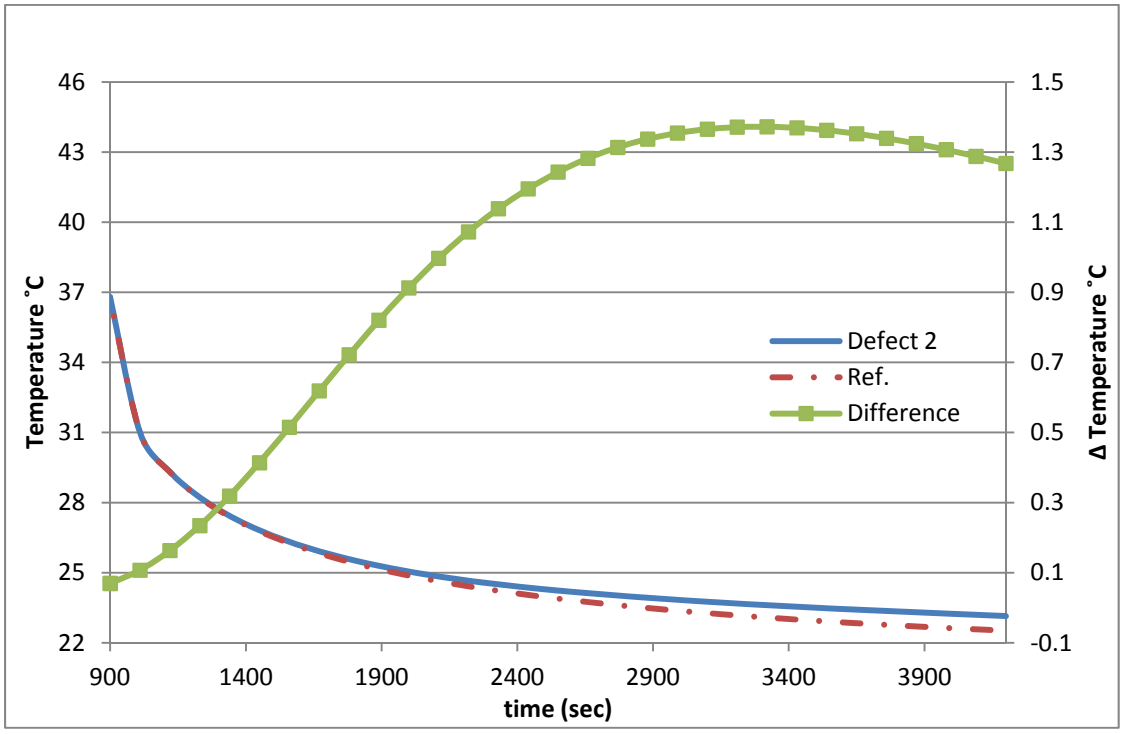

Figure 3.18: Defect 2 surface temperature versus time FEM results

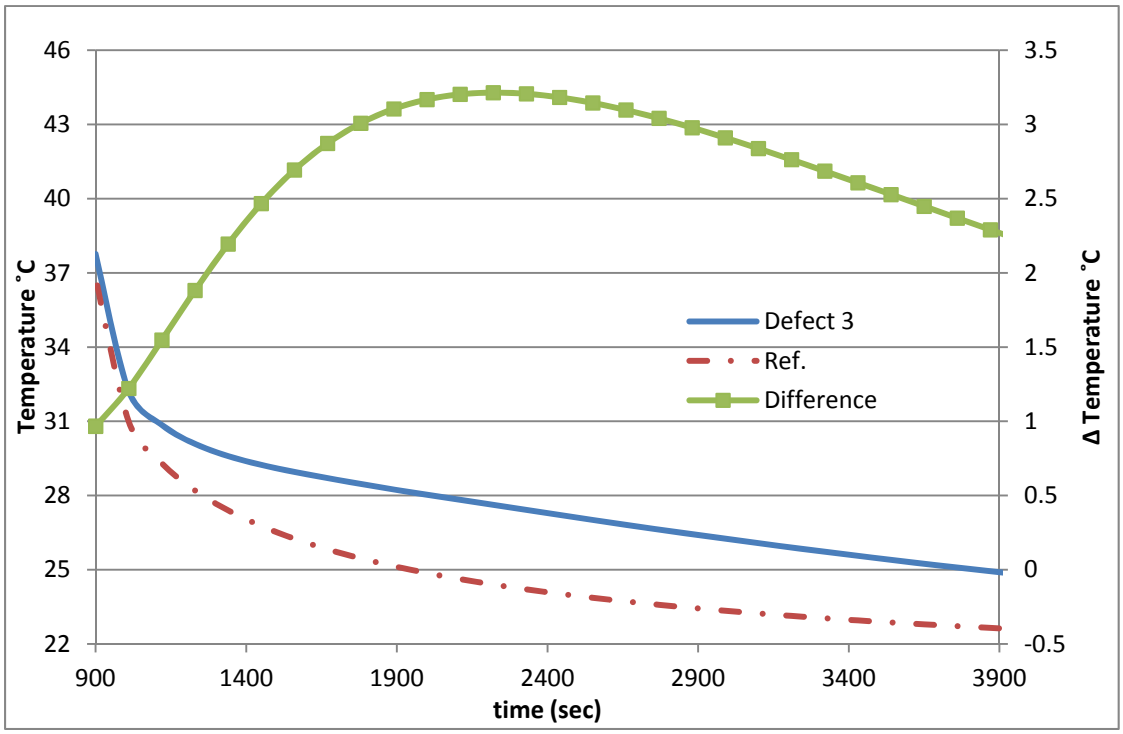

Figure 3.19: Defect 3 surface temperature versus time FEM results

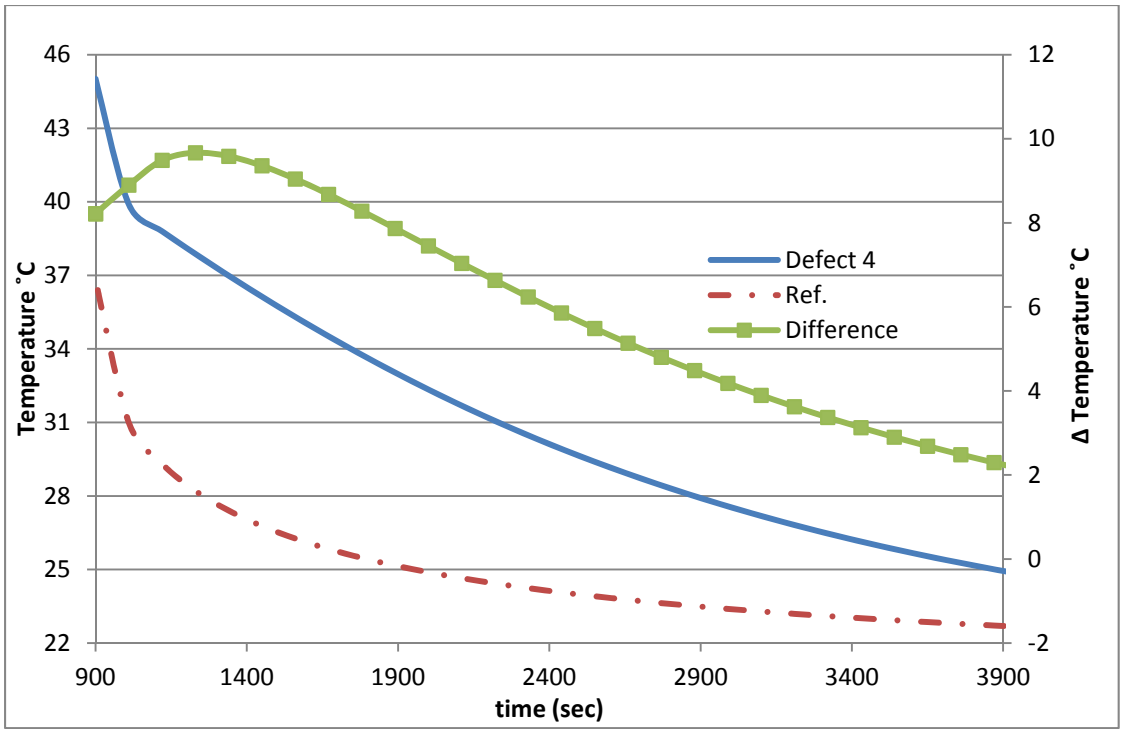

Figure 3.20: Defect 4 surface temperature versus time FEM results

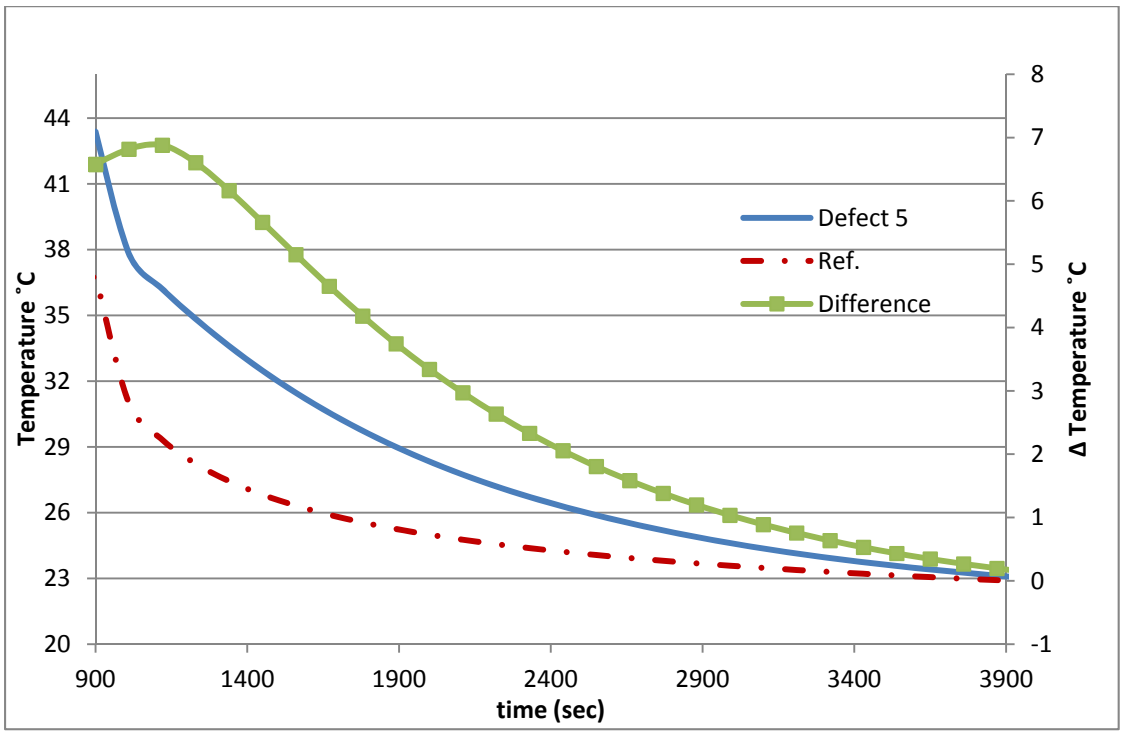

Figure 3.21: Defect 5 surface temperature versus time FEM results

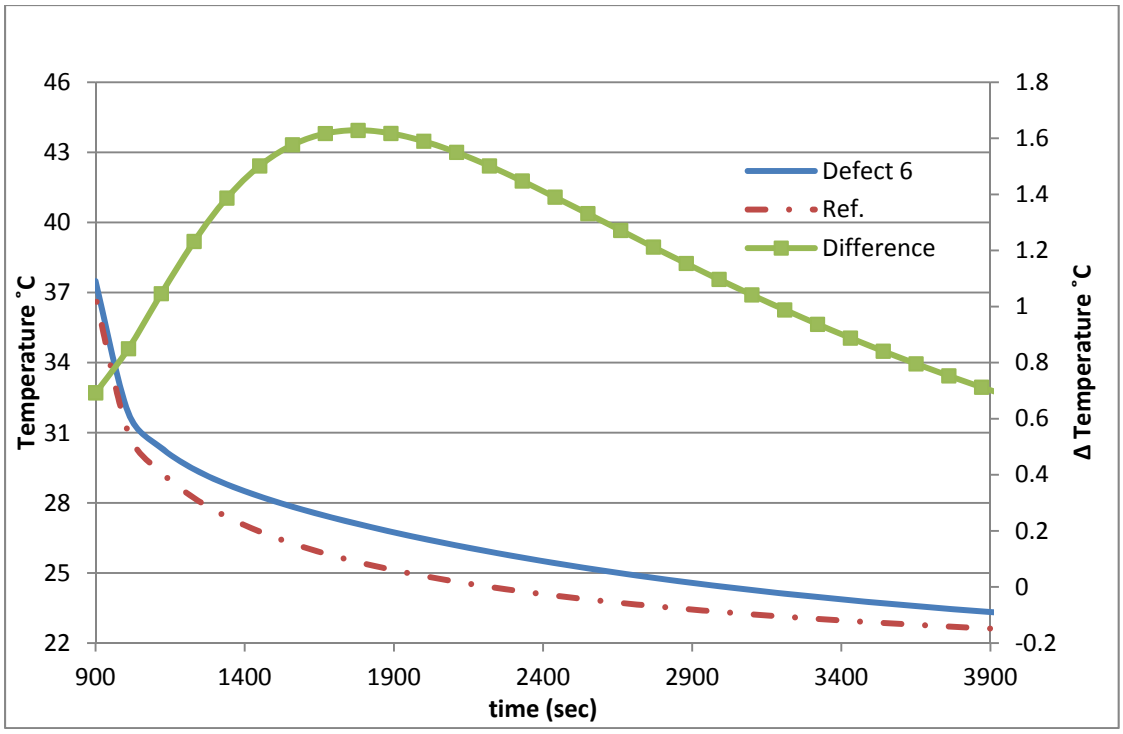

Figure 3.22: Defect 6 surface temperature versus time FEM results

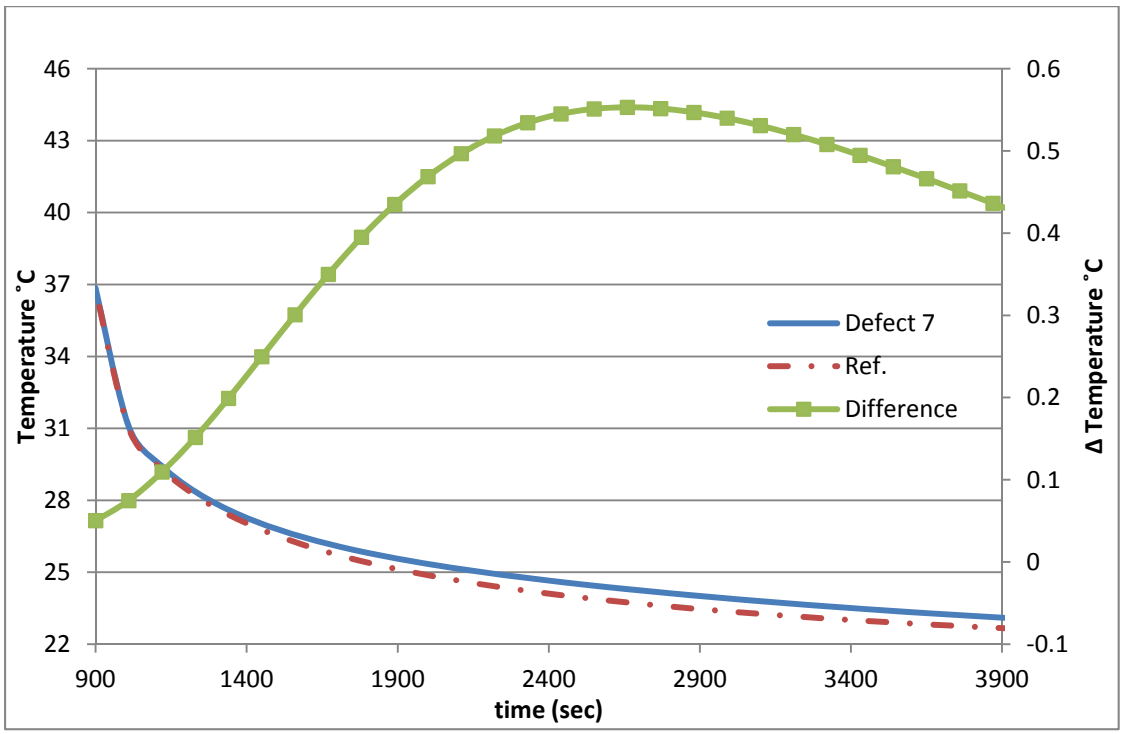

Figure 3.23: Defect 7 surface temperature versus time FEM results.

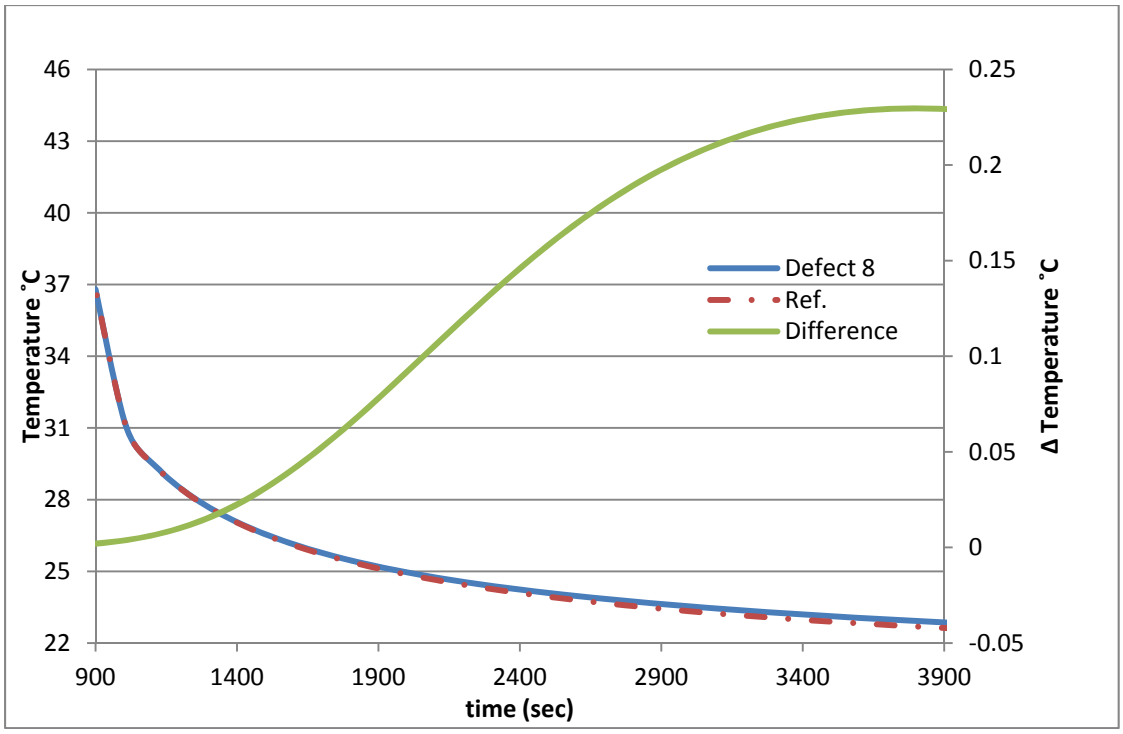

Figure 3.24: Defect 8 surface temperature versus time FEM results.

CHAPTER 4
INTRODUCTION TO SCC WALL THERMOGRAPHY STUDY

4.1 INTRODUCTION

This chapter is an introduction to the SCC wall study, which involves infrared thermography as a method to detect defects within the composite structure subsurface. The sections below discuss the construction of the SCC wall, the modeled SCC wall created in Abaqus, the modeling analysis and procedure, and the convergence study performed.

4.2 SCC WALL CONSTRUCTION

An alternative structure to reinforced concrete floors, wall and other structural components used in a nuclear power plant is the Steel Concrete Composite structure. In this study our interest is focused on the SCC wall, which is a reactor containment structure constructed by placing concrete between two steel plates that form the concrete and provide the permanent exterior face of the structure (Shown in Figure 4.1). Welded in the inner surface of the two steel plates are shear studs, which are embedded into the concrete once the concrete is poured between the two plates. The studs are embedded into the concrete to tie the concrete and steel plates together. The studs are also used to connect the two steel plates together during modular construction are tie bars, which are welded to both steel plates connecting the plates together throughout the wall (shown in Figure 4.2).

4.3 SCC WALL MODEL

The basic structural components of the model consist of two half inch thick steel plates and a concrete interior. The model did not include any steel reinforcements because they were not necessary in the thermography analysis performed. The subcomponent of the SCC wall (a section of the SCC wall) was created in the model with the dimensions of 1.5 m x 0.75 m x 0.8 m as shown in Figure 4.2 and Figure 4.3. The concrete component that lies between the two steel plates has a thickness of .7875 meters. The SCC wall model only has the top steel plate modeled since the bottom steel plate would have no significant effect on the thermal analysis results.

As the BAM model discussed previously, the concrete and steel parts were bonded together using tie constraints. Figure 4.3 is an image of the concrete and steel parts bonded together in the Abaqus model. The defect within the concrete was modeled as 10 cm^3 empty void. The defect was modeled with a cavity radiation on the interior surfaces of the concrete-air interaction of the void. The cavity radiation captures the thermal radiation that occurs due to the temperature difference inside the concrete defects. In this model, the defect was located at the center of the SCC wall model and was placed at depths specified later the report.

4.4 ANALYSIS PROCEDURE OF SCC WALL MODEL

There were three analytical steps preformed in each analysis: initial condition, heating phase and the cooling phase. The procedure of this finite element analysis was performed with the identical procedure previously discussed in the BAM model in Chapter 3. In the model, an ambient temperature of 20 ^0C was defined for the concrete and steel specimen. On the second analysis step, a uniform surface heat flux (q) was

applied to the top surface of the steel in the z axis of orientation for a time period and heat flux specified in the next chapter. During the heating phase, three thermal surface interactions (boundary conditions) were applied. The bottom surface of the SCC wall has a surface radiation interaction with an emissivity value of 0.8. Also applied to the bottom surface of the specimen was a surface film condition (thermal convection) with a film coefficient of 6.5 W/m^2. The third thermal interaction used in this step of the analysis was the cavity radiation applied to the inside surface surrounding the air void within the concrete part. As described before, this cavity radiation helps model the accumulation of heat within the void area embedded inside the concrete steel specimen. During the cooling phase, the same surface interactions continue to propagate, with an additional surface radiation and film condition applied to the top of the steel specimen using the same coefficient values. The sides and edges of the concrete specimen were modeled as adiabatic boundary conditions.

4.5 CONVERGENCE STUDY OF SCC WALL MODEL

Similar to the convergence study performed in the previous chapter, an h-convergence and p-convergence study was completed for the SCC wall model.

Table 4.1 summarizes the convergence studies performed for the SCC wall model. The convergence study consisted of three different types of meshes and two different types of nodal elements. Figure 4.4 shows the meshes used for the h-convergence study. Three meshes were used for this convergence study; which were a coarse mesh (Mesh 1), a fine mesh (Mesh 3) and an average of the two meshes (Mesh 2). Also the p-

convergence study was also conducted using an 8 node linear heat transfer element and a 20-node quadratic heat transfer element.

Figure 4.5 shows the temperature vs. time relationship at the surface of the steel plate exposed to a constant heat source of 1250 W/m^2. The graph in Figure 4.5 corresponds to the 8-node linear heat transfer element plotted for Mesh 1, Mesh 2, and Mesh 3.

Likewise, Figure 4.6 shows the temperature vs. time relationship at the surface of the steel plate for the 20-node quadratic heat transfer element corresponding to Mesh 1, Mesh 2, and Mesh 3.

Figure 4.7 is the temperature vs. time results for both the linear and quadratic nodal elements corresponding to all three meshes.

The results graphed for the 8-node linear elements shown in Figure 4.5 shows a large difference in temperature for each of the three Meshes. Mesh 2 has the highest temperature at approximately 90 ^0C, Mesh 1 at 77 ^0C and Mesh 3 at 52 ^0C. With a maximum difference of 38 ^0C, the results from the 8-node linear heat transfer prove that the element's geometric discretization has a large impact on the accuracy of the results obtained from the model. The 20-node quadratic elements shown in Figure 4.6 shows that Mesh 1 and Mesh 2 both have similar surface temperatures versus time curves, but Mesh 3 has a temperature difference of about 38 ^0C.

Figure 4.7 is a representation of all of the graphs produced in this convergence study. By combining all of the graphs into one figure, it can be seen that the most dominant factor in the accuracy of the results are based upon the geometric discretization or the

meshing of the model. For example, Mesh 3 linear and quadratic heat transfer elements both obtain almost identical results, while Mesh 2 and Mesh 1 linear and quadratic elements are dissimilar. The difference in temperatures of the linear and quadratic Mesh 2 and Mesh 1 is due to several reasons, such as the non-geometrically aligned elements (caused by the void within the concrete specimen). In this experiment, Mesh 3 has smaller element arrangement that allows it aligned to the model's geometrical shape (such as the air void in the middle of the specimen, which can create a misalignment of nodes). The difference in temperature can also be influenced by the degree of the polynomial equation used to solve the finite element analysis. Furthermore, with two different materials being used in this model (steel and concrete), the heat transfer from the steel portion of the specimen to the concrete may require a finer element to allow the temperature gradient to diffuse through the steel-concrete model.

The convergence study performed showed a convergence in the surface temperature as the gradual increase in a more precise method of solutions was used in the model. Therefore in the SCC wall model, a 20 node quadratic heat transfer brick (DC3D20) element similar to M3-1was used to obtain the most accurate results from the model.

Figure 4.1: Steel Concrete Composite wall structure under construction phase (International Atomic Energy Agency)

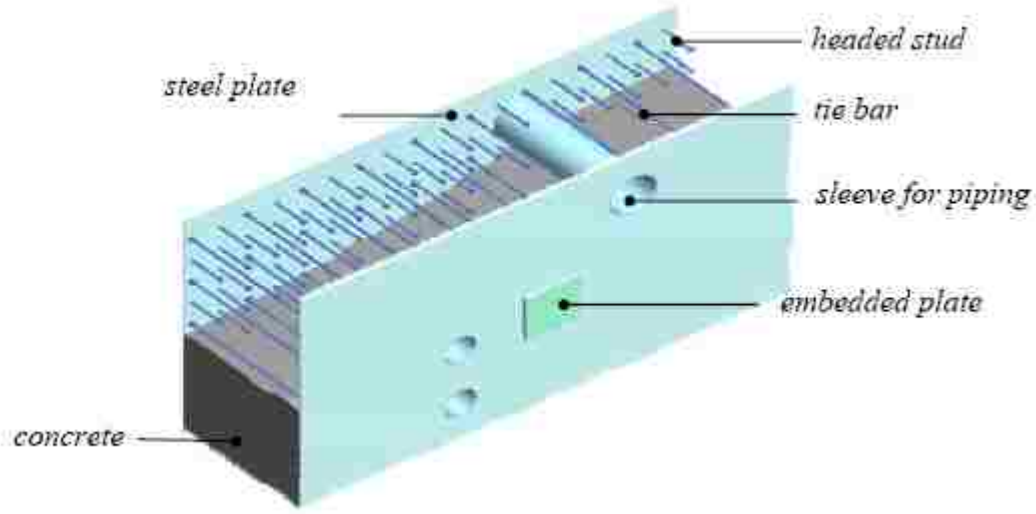

Figure 4.2: Internal arrangement of a typical Steel-Plate Concrete Composite Structure, also known as a Steel Concrete Composite Structure (U.S. Department of Energy)

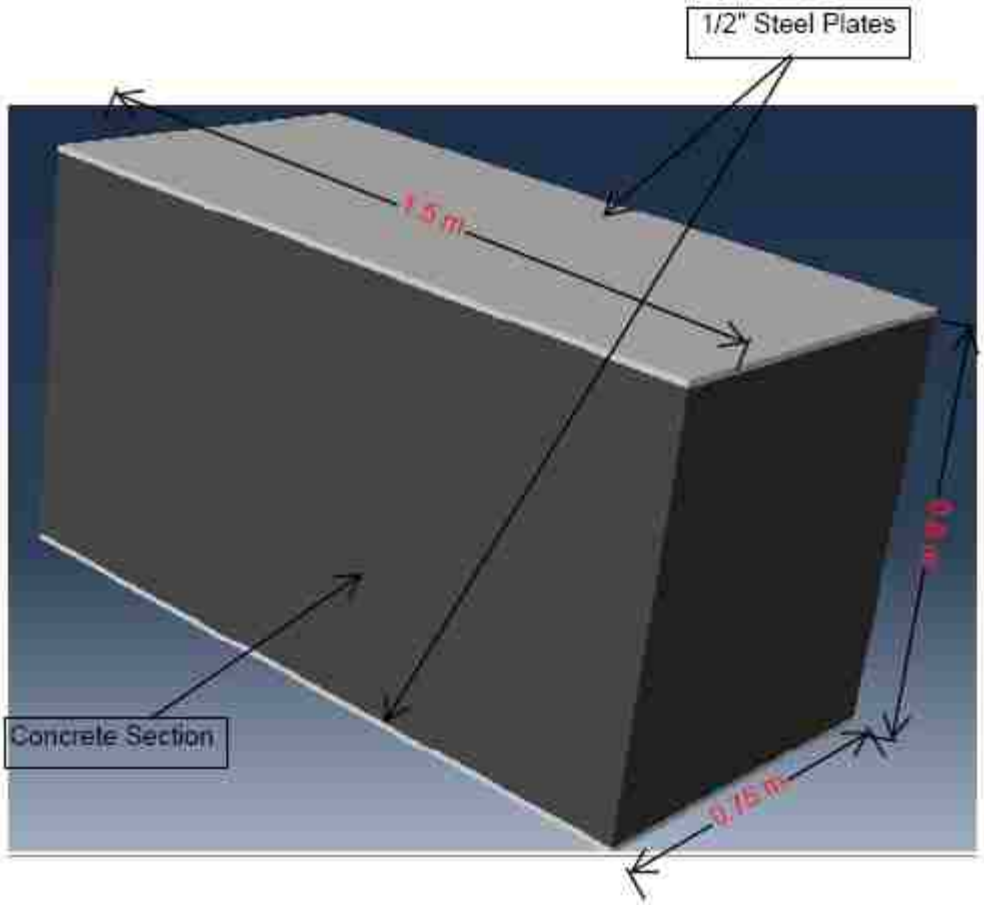

Figure 4.3: Finite element model of SCC wall substructure.

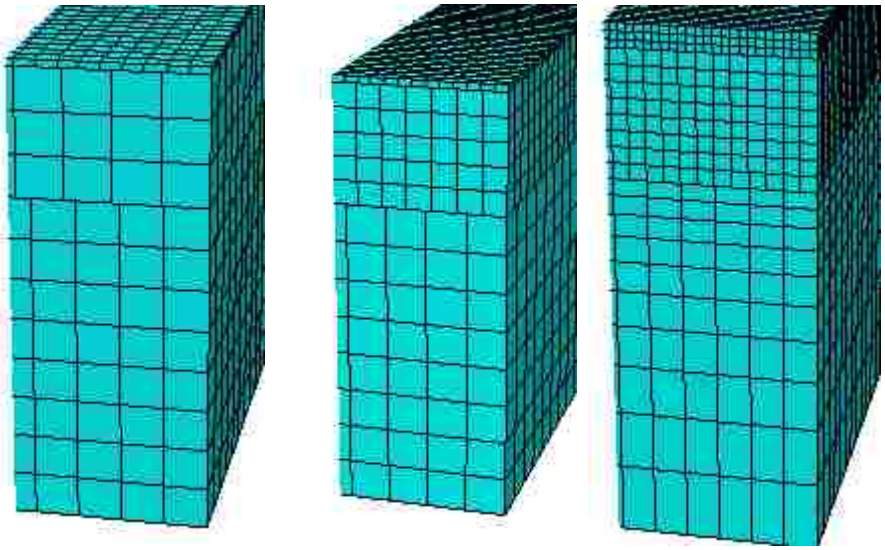

Mesh 1 Mesh 2 Mesh 3

Figure 4.4: The images above represents the h-convergence studies for the concrete model with the different mesh sizes.

Table 4.1: Convergence study analysis matrix for Steel-Concrete Composite wall specimen

Designation	Mesh	Element Type
M1-1	Mesh 1	8-node linear element
M2-1	Mesh 2	8-node linear element
M3-1	Mesh 3	8-node linear element
M1-2	Mesh 1	20-node quadratic element
M2-2	Mesh 2	20-node quadratic element
M3-2	Mesh 3	20-node quadratic element

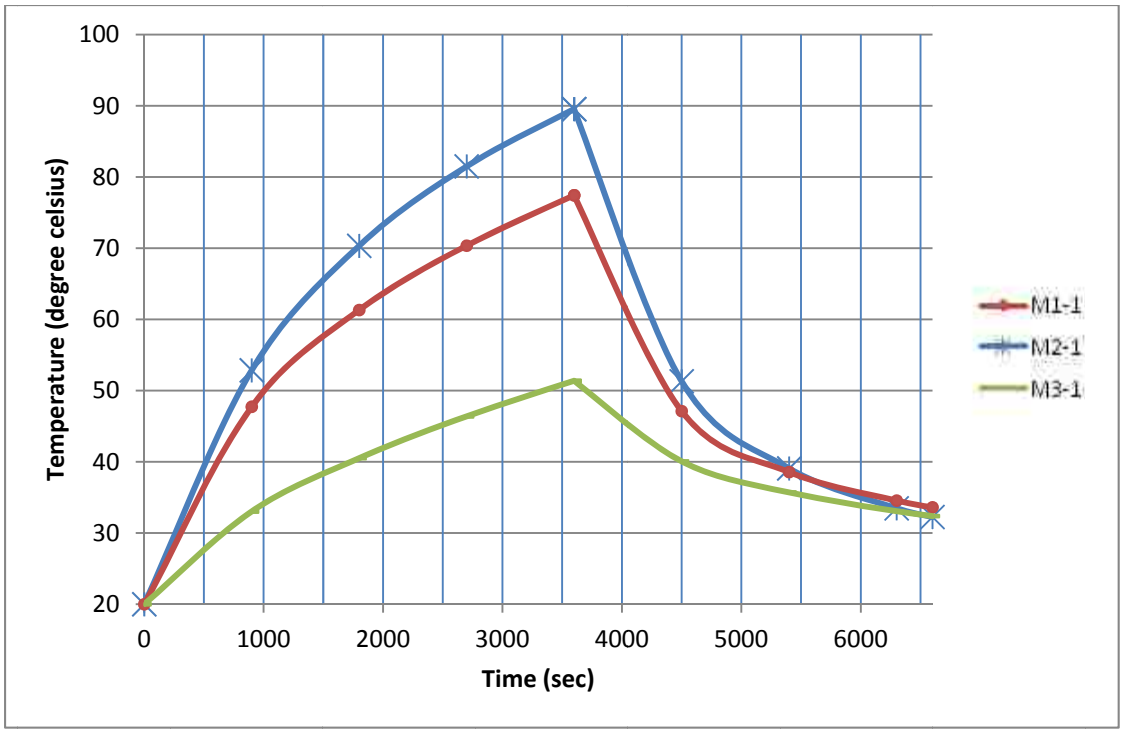

Figure 4.5: Surface temperature of concrete specimen during the finite element analysis, using 8-node linear elements

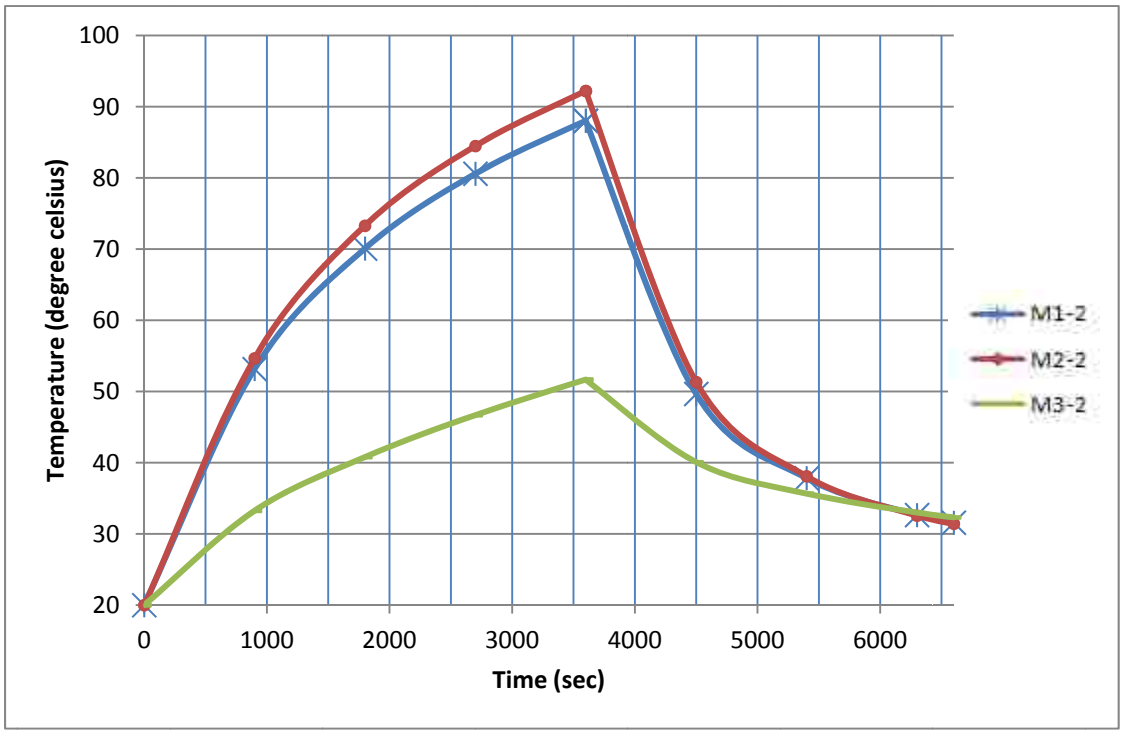

Figure 4.6: Surface temperature of concrete specimen during the finite element analysis, using 20-node linear elements

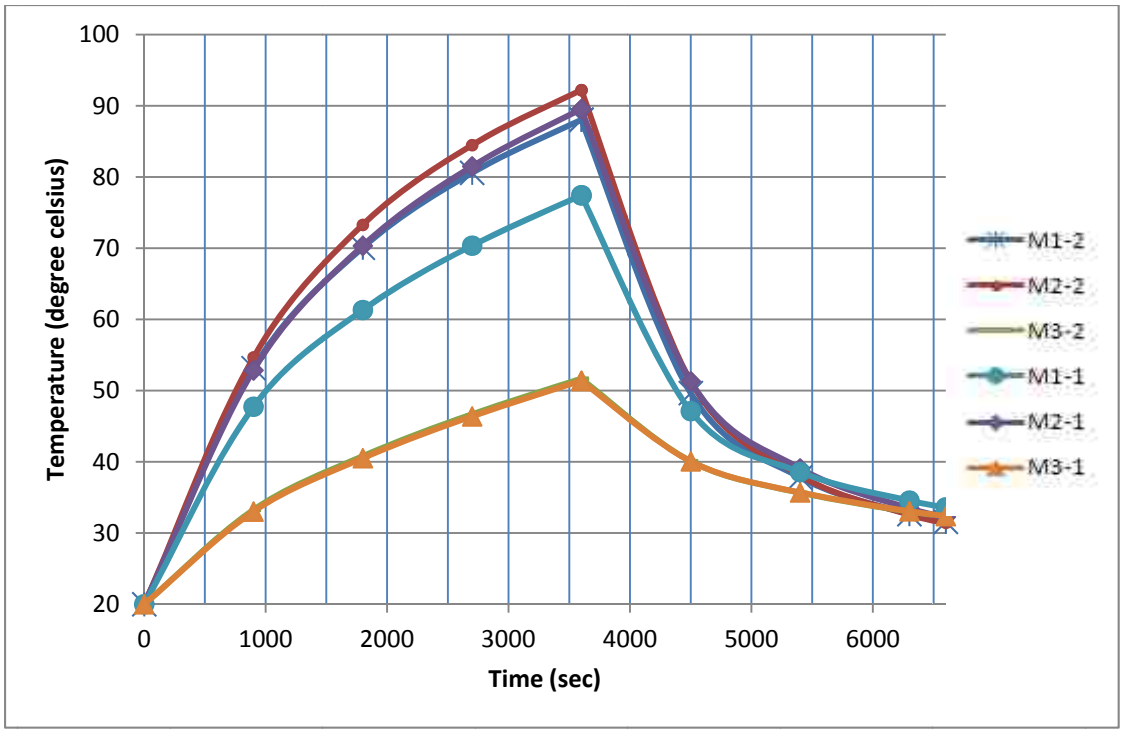

Figure 4.7: Surface temperature of concrete specimen during the finite element analysis for the 8 node elements and 20 node elements

CHAPTER 5
ANALYSIS RESULTS

5.1 INTRODUCTION

This chapter presents the results of the SCC wall analyses. The study performed consisted of seven parametric cases each influencing the results obtained in the model. In this chapter, the result for each parametric case is investigated to evaluate its influence on the temperature versus time curve and thus reveal the suitability of thermography as an NDT method for flaw detection.

5.2 ANALYSIS MATRIX

The analysis matrix consists of the seven different cases shown on Table 5.1. The three parameters treated in the analyses were the depth of the void (D), the heat flux applied to the SCC wall (q), and the time duration (t_h) for which the heat flux was applied. The depth of the void is defined from the top of the steel surface to the top of the defect's surface as shown in Figure 5.1, which is a typical section of the SCC wall modeled in Abaqus. The three parameters mentioned above all have a direct influence on the results of the detection of abnormalities within the specimen. Although many other factors may influence the detection of abnormalities, the three parameters selected are often encountered in realistic applications of thermography as a form of NDT.

Table 5.1: Analysis Matrix

Case	Flaw Depth, D (meter)			Heat Flux, q ($Js^{-1}m^{-2}$)		Heating Duration, t_h (seconds)	
	0.0125	0.0375	0.0875	625	1250	900	3600
1	X				X		X
2		X			X		X
3			X		X		X
4	X			X			X
5		X		X			X
6			X	X			X
7	X				X	X	

5.3 CASE 1

Analysis Case 1 is defined as shown on Table 5.1. In Case 1, the defect was modeled in Abaqus as a 0.1 m^3 cube. In Case 1, the defect's depth was defined at .0125 meters. Also for Case 1, the thermal surface heat flux (q) and time duration of the heat flux (t_h) were 1250 $JT^{-1}L^{-2}$ and 3600 seconds respectively. Figure 5.1 shows the locations of where the surface temperatures during the analysis were recorded on the specimen. The result of the maximum temperature occurrence on the surface of the specimen in respect to time was graphed on Figure 5.2. The maximum temperature occurrence for all cases were located at the center of the void, which are shown later in this chapter.

Figure 5.2 shows an increasing surface temperature directly above the void, while a constant heat flux is applied to the specimen until the end of the heating phase at 3600 seconds. The maximum temperature occurred at the end of the heating phase and was computed as approximately 93 ^{0}C. During the cooling phase, the surface temperature initially decreased rapidly towards the ambient temperature. The rate of cooling was somewhat greater than the rate of heating.

Figure 5.3 shows the difference in surface temperature over the void as compared to a reference point on the specimen's surface. The reference point's temperature was designated as a surface temperature at a distance from which it is not affected by the defect, giving the specimen's normal undisturbed temperature as shown in Figure 5.1. It can be seen that the maximum temperature difference occurs at the ending of the heating phase and is measured at approximately 35 ^{0}C. This change of temperature is significant when performing infrared thermography, in order to detect defects within the specimen. High maximum temperature differences allow defects to be easily seen during the infrared thermography evaluation.

Figure 5.4 is a plot of Case 1 surface temperature versus the specimen's surface position in the y-axis. The surface temperature reading for this graph was taken at a series of points going across the specimen from the center of the defect, to 0.3 meters at both ends in the y-axis. The graph shows how the temperature distribution across the width of the specimen is affected by the defect. Six different specified times (in 900 second intervals) during the analysis were graphed in order to provide an overall depiction of how the temperature varies across the width of the specimen. Figure 5.4 plots are each symmetric, with a maximum temperature occurring at the center of the specimen directly over the void. The width of the defect is positioned on the graph at the location of 0.1 meters to 0.2 meters, which a drastic increase in the temperature can been seen. The maximum temperature recorded occurred at the end of the heating phase, (3600 seconds) at 93 ^{0}C. As expected, with the increase of time, the surface temperature also increased. The times corresponding to the cooling phase in this figure shows a significant drop in surface temperature; such that, the last two times of 6300 and 6600 seconds begin to concave over the defects . The small concavity over the

defect shows that the thermal energy over the area of the defect allows the temperature to dissipate from the specimen at a more rapid rate compared to the undisturbed surfaces of the specimen.

Figure 5.5 shows the difference in temperature in the y-axis of orientation, which gives a better perspective of the change in temperature in respect to an undisturbed reference point on the specimen's surface. Similar to Figure 5.4, the maximum difference in temperature can be seen in the graph, and more importantly the change in temperature at a specified position on the specimen can also be observed on the graph. Subsequently, it can be seen that a large temperature change near and over the defect can been detected starting at 900 seconds of the heating.

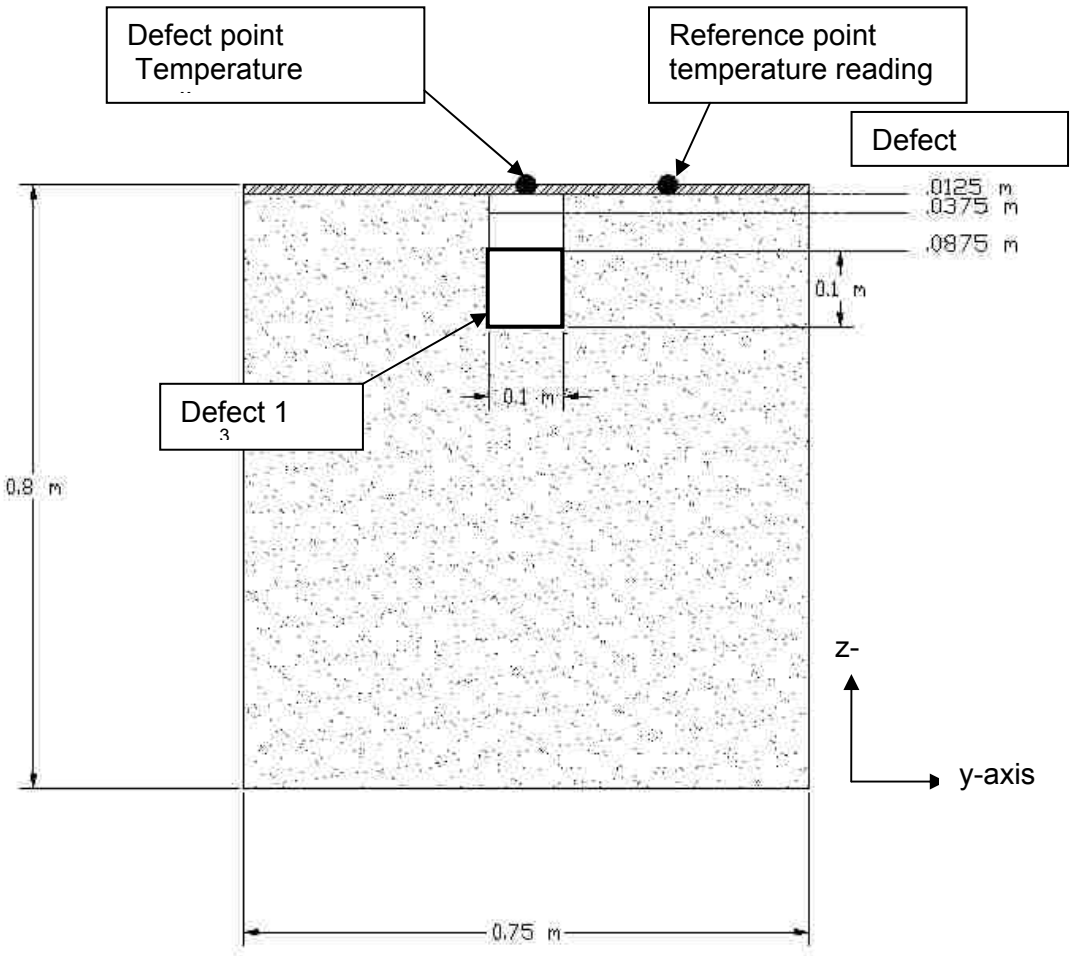

Figure 5.1: Elevation view of SCC wall section with the corresponding reference point location

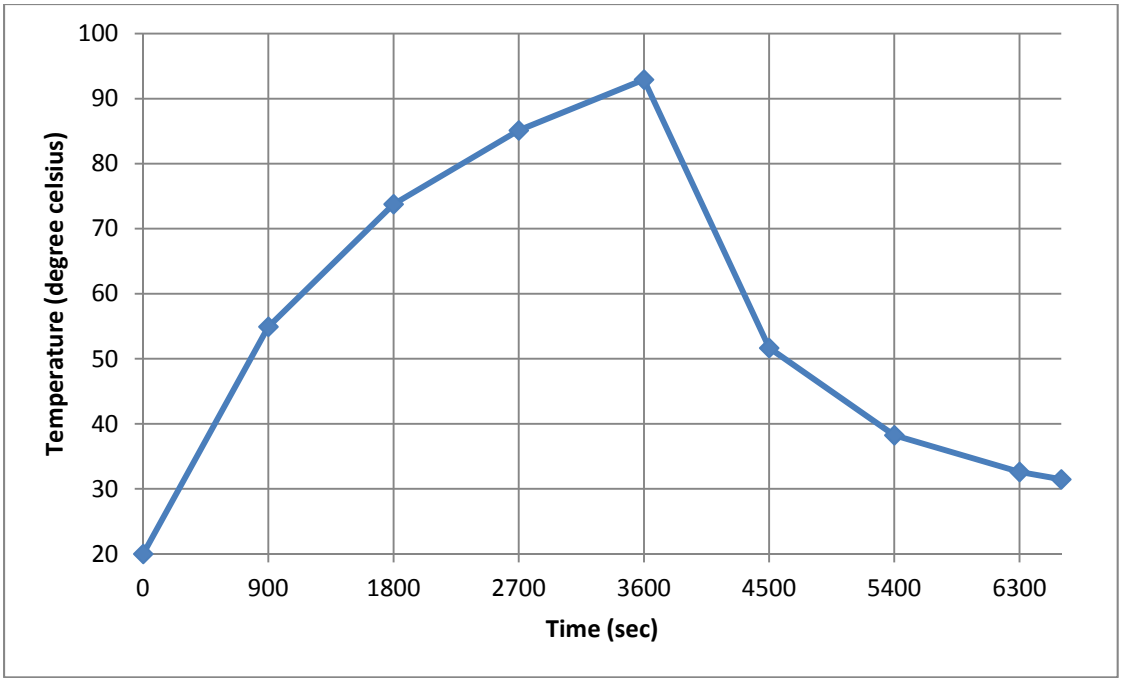

Figure 5.2: Results of Case 1 Temperature vs. Time curve for the SCC Wall

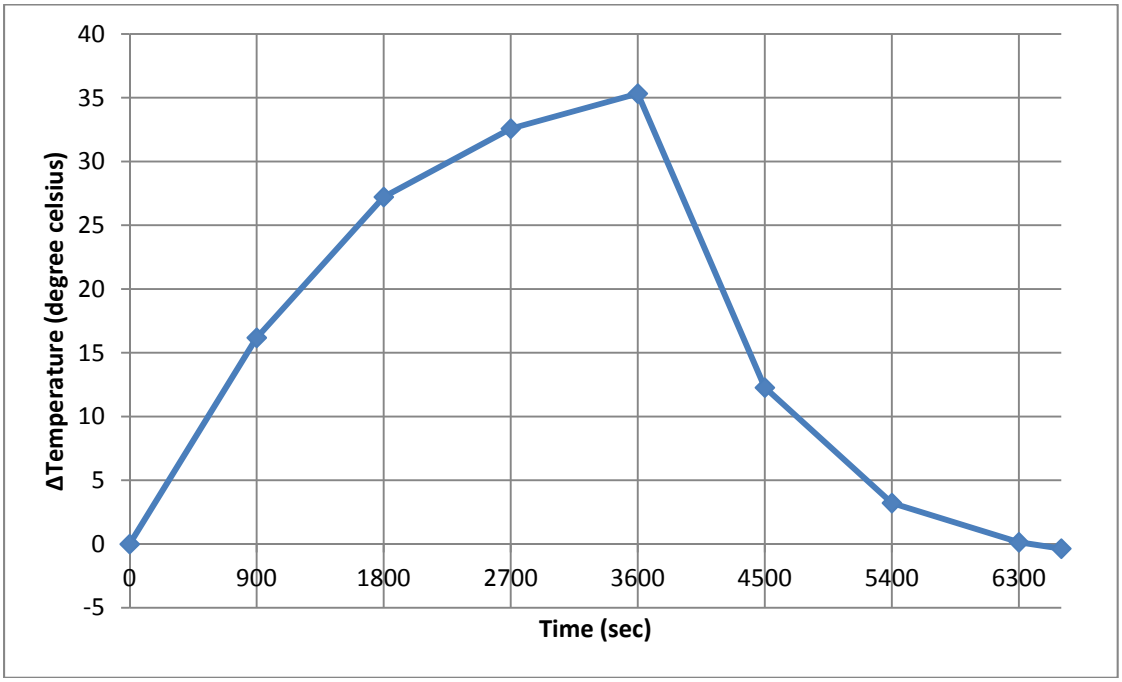

Figure 5.3: Results of Case 1, difference in Temperature vs. Time. The difference in temperature was calculated by the surface temperature difference between the defect and designated reference point

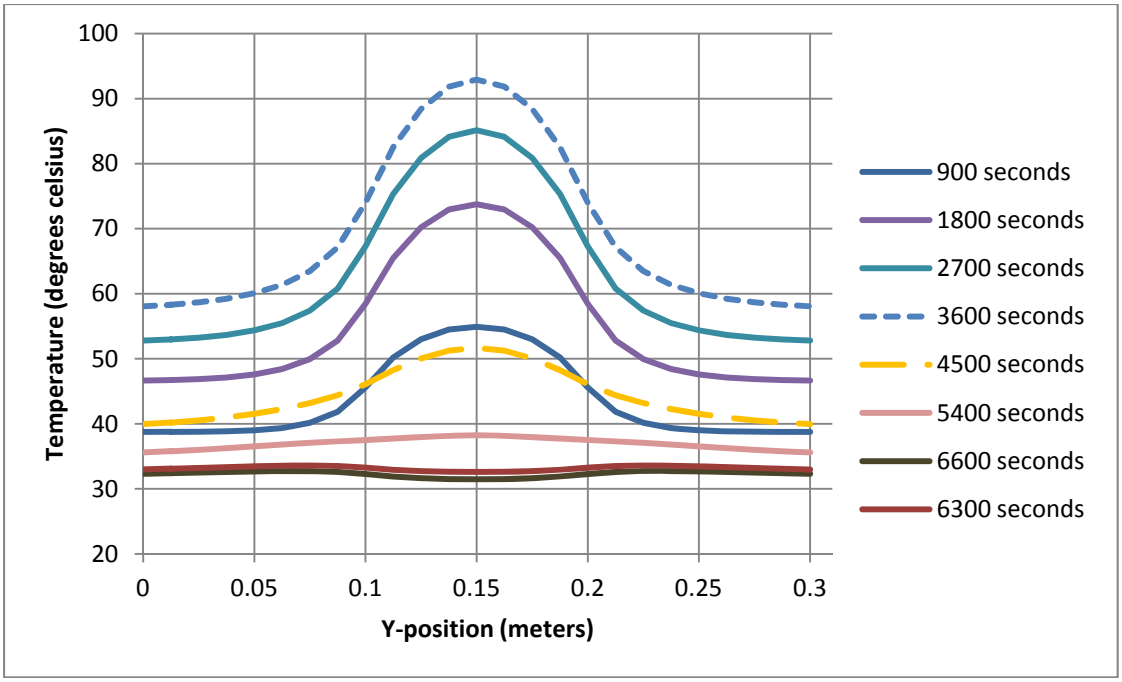

Figure 5.4: Case 1 surface temperatures versus the specimen's surface position in the y-axis, for the given heating and cooling durations

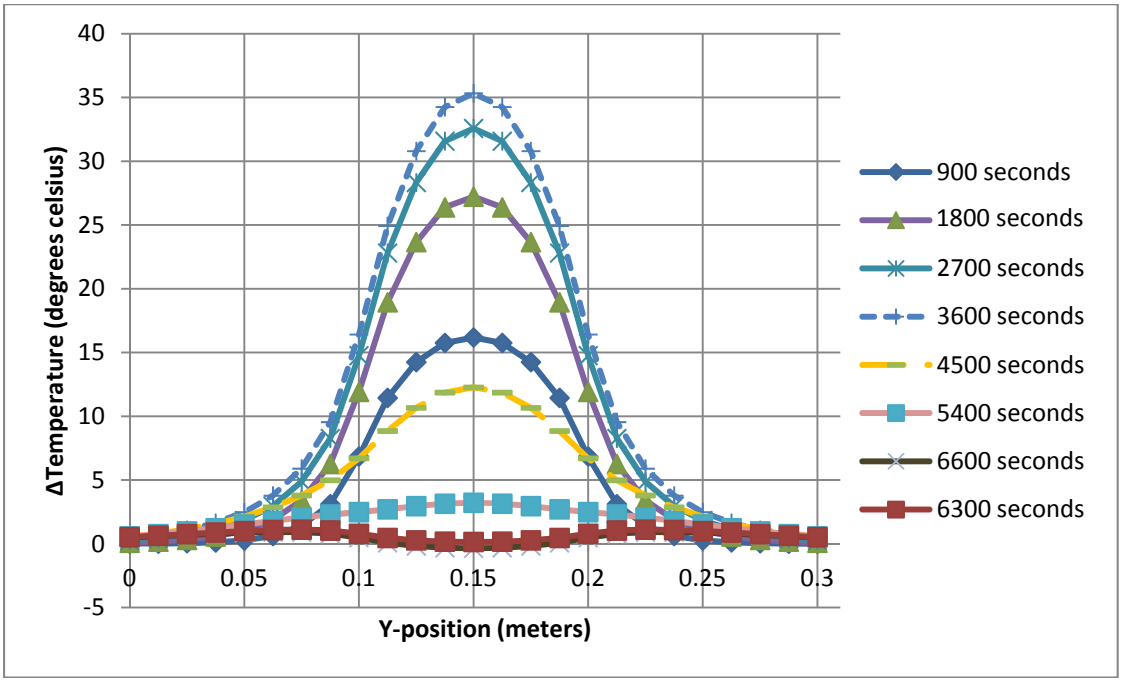

Figure 5.5: Case 1 difference in surface temperatures versus the specimen's surface position in the y-axis, for the given heating and cooling durations

5.4 CASE 2

Analysis Case 2 consisted of the same SCC wall model as Case 1, but with a change in depth of the defect to .0375 meters. Similar to Case 1, the thermal surface heat flux (q) and time duration of the heat flux (t_h) were 1250 $JT^{-1}L^{-2}$ and 3600 seconds respectively. The results of the maximum temperature occurrence on the surface of the specimen in respect to time are graphed in Figure 5.7. Figure 5.7 shows a similar increasing rate of surface temperature over the defect, to a maximum temperature of 65 ^{0}C. The maximum surface temperature occurs at the ending of the heating phase at 3600 seconds; then after, entering the cooling phase where the surface temperature has a gradual decrease towards the ambient temperature. The rate of change in the increase and decrease of the surface temperature are relatively similar to one another, showing that the rate of heating and cooling during this process are similar.

Figure 5.8 is a graph of the difference in surface temperature over the defect as compared to a reference point on the specimen's surface (Figure 5.1). The graph shows that the maximum temperatures difference between the surface over the defect and the surface of an unaffected area of the specimen is approximately 7.7 ^{0}C. It can be argued that the detection of the defect at the depth of .0375 meters is possible based on this temperature change, but the graph shows that there is a much smaller time duration from which the defect can be detected due to the decrease in the maximum difference in surface temperature in this case.

Figure 5.9 is a plot of Case 2 surface temperature versus the specimen's surface orientation in the y-axis (shown in Figure 5.6). Six different specified times (in 900 seconds intervals) during the analysis were graphed in order to get an overall depiction

of how the temperature varies across the width of the specimen. The maximum temperature occurring at the center of the specimen directly over the defect was recorded at 65 ^{0}C. The distance between the defects , 0.1 meters to 0.2 meters, showed a small increase in surface temperature change during the analysis. At the initial temperature recording (900 seconds) and the last temperature recordings (5400, 6300 and 6600 seconds) only a small temperature change from the surface over the void and the reference point of the specimen is shown on the graph. The remaining times show the temperature change between the surface over the void and the unaffected surface is much more noticeable.

Figure 5.10 is the difference in surface temperature in the y-axis of orientation. This graph gives a better representation of the change in temperature with respect to an undisturbed reference point on the specimen's surface. Similar to Figure 5.8, the maximum difference in temperature can be seen in the graph, and more importantly the difference in temperature at a specified position on the specimen can also be observed on the graph. It can also be seen that the recorded time of 3600, 4500, 2700 and 5400 seconds, the surface temperature change is still over 5 ^{0}C.

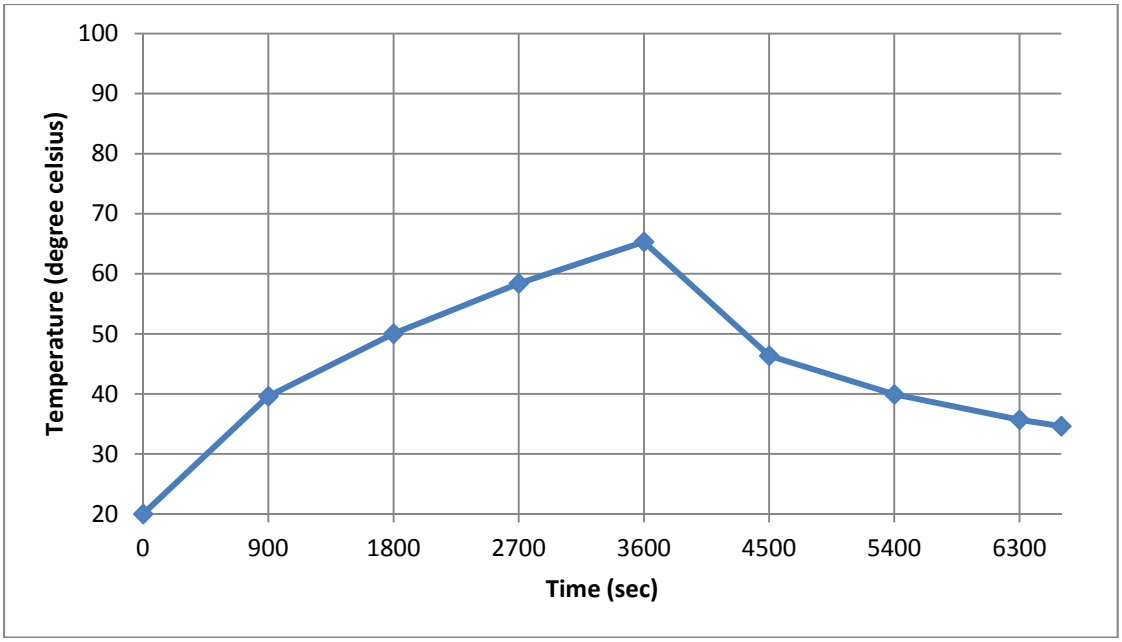

Figure 5.7: Results of Case 2 Temperature vs. Time curve for the SCC Wall

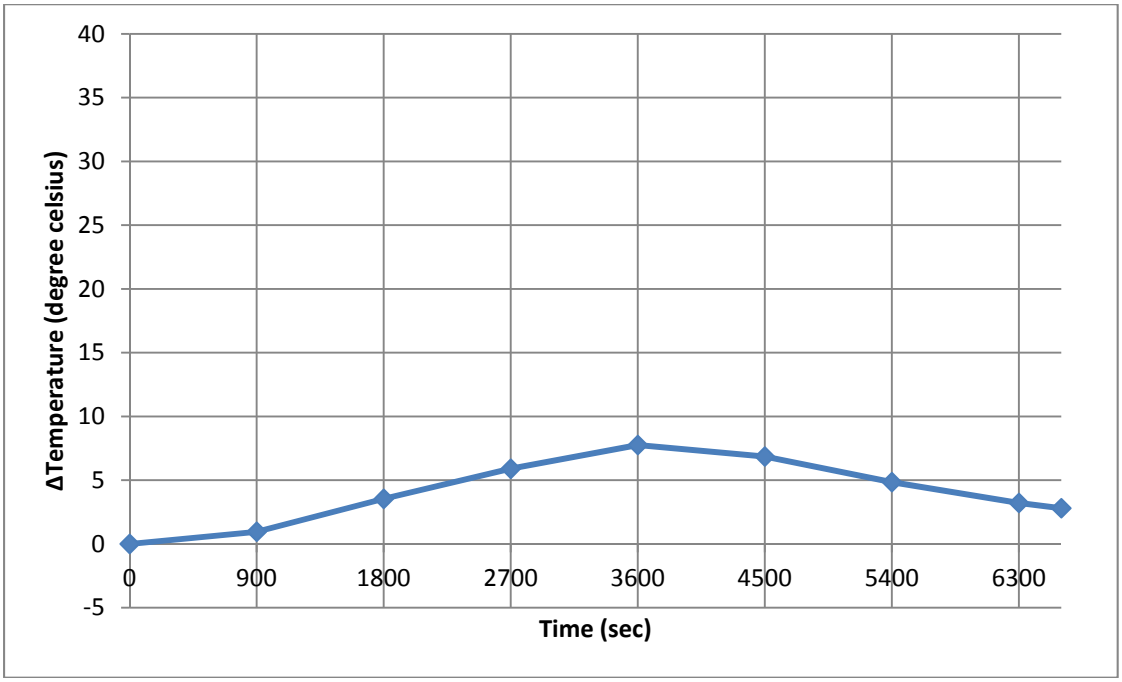

Figure 5.8: Results of Case 2, difference in Temperature vs. Time. The difference in temperature was calculated by the surface temperature difference between the defect and designated reference point

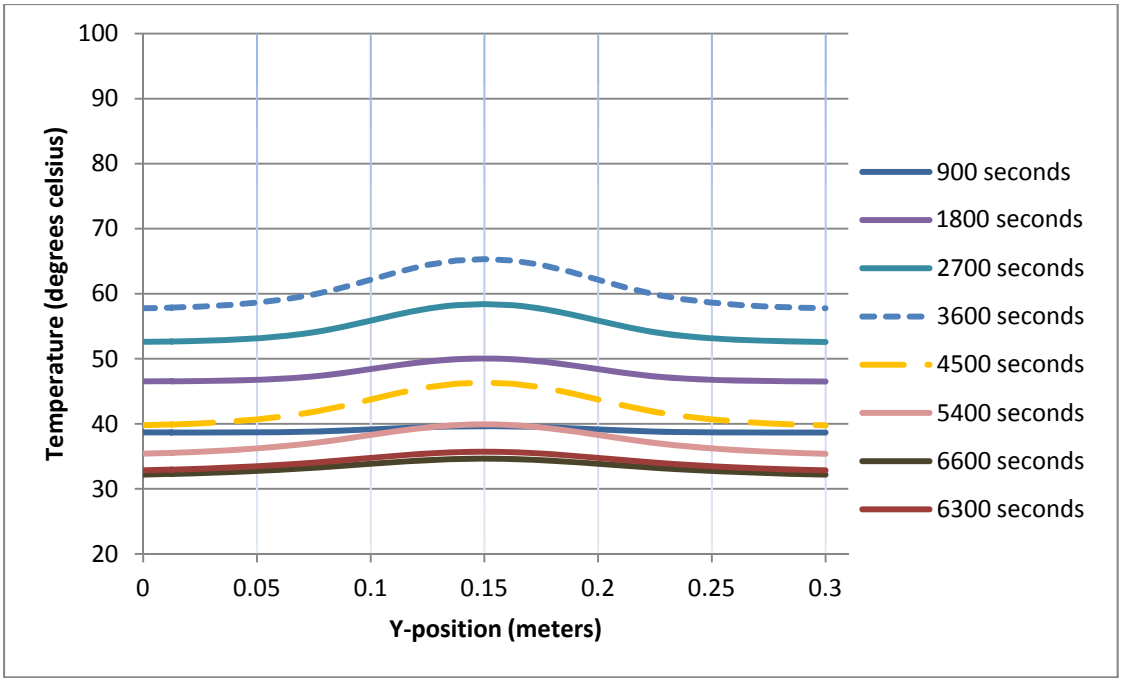

Figure 5.9: Case 2 surface temperatures versus the specimen's surface position in the y-axis, for the given heating and cooling durations

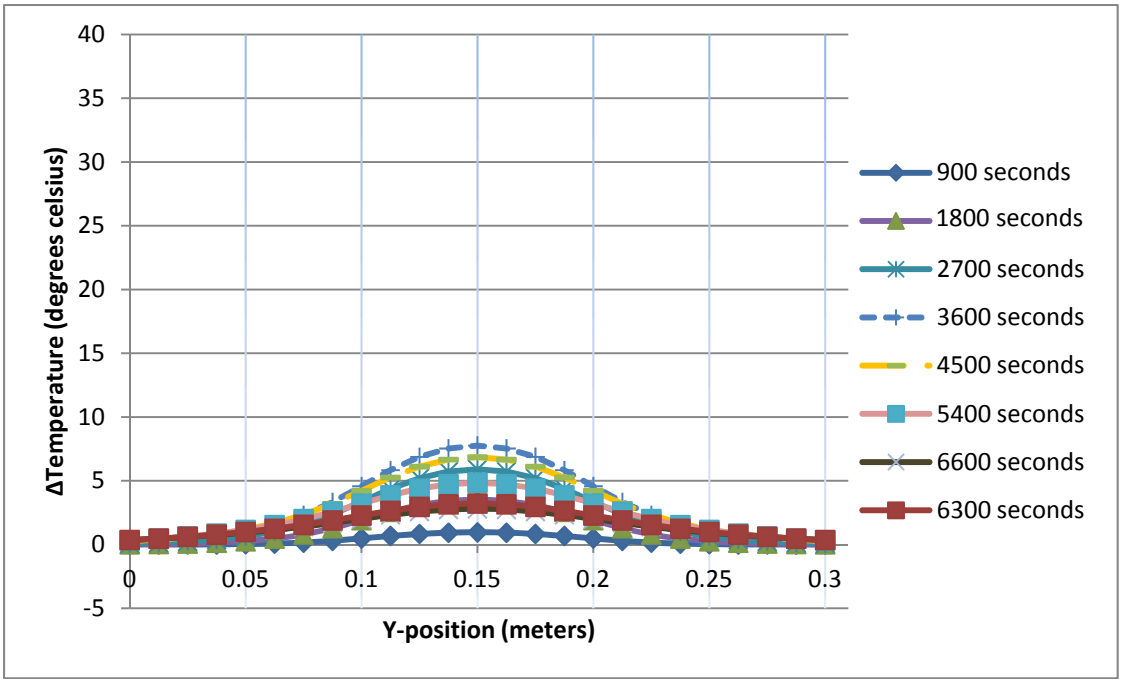

Figure 5.10: Case 2 difference in surface temperatures versus the specimen's surface position in the y-axis, for the given heating and cooling durations

5.5 CASE 3

Analysis Case 3 consisted of the same SCC wall model as Case 1, but with a change in the depth of the defect to .0875 meters. Similar to Case 1, the thermal surface heat flux (q) and time duration of the heat flux (t_h) were 1250 $JT^{-1}L^{-2}$ and 3600 seconds respectively. The results of the surface temperatures in respect to time are graphed in Figure 5.11. Figure 5.11 shows a maximum surface temperature of 58 ^{0}C. The maximum surface temperature occurs at the ending of the heating phase at 3600 seconds; then after, entering the cooling phase where the surface temperature has a gradual decrease towards the ambient temperature.

Figure 5.12 is a graph of the difference in surface temperature over the void as compared to a reference point on the specimen's surface. The graph shows that the maximum temperatures difference between the surface over the defect and the surface of an unaffected area of the specimen is approximately .8 ^{0}C. The time at which the maximum difference in surface temperature occurred was recorded between 6300 and 6600 seconds. The graph shows that the change in surface temperature continued to increase even throughout the end of the analysis during the cooling phase.

Figure 5.13 is a plot of Case 3 surface temperature versus the specimen's surface position in the y-axis. Six different specified times during the analysis were graphed in order to get an overall depiction of how the temperature varies across the width of the specimen throughout the entire analysis. A maximum temperature occurring at the center of the specimen directly over the defect was recorded at 60 ^{0}C. The temperature readings located over the defects and away from the defects have no noticeable temperature change at all times during the analysis.

Figure 5.14 is the difference in surface temperature in the y-axis of orientation. This graph gives a better representation of the change in temperature with respect to an undisturbed reference point on the specimen's surface. It can be seen that all of the graphs at the time intervals given are all very similar and show almost no change in temperature. The maximum difference in temperature was recorded at .8 ^{0}C and occurs between 6300 and 6600 seconds.

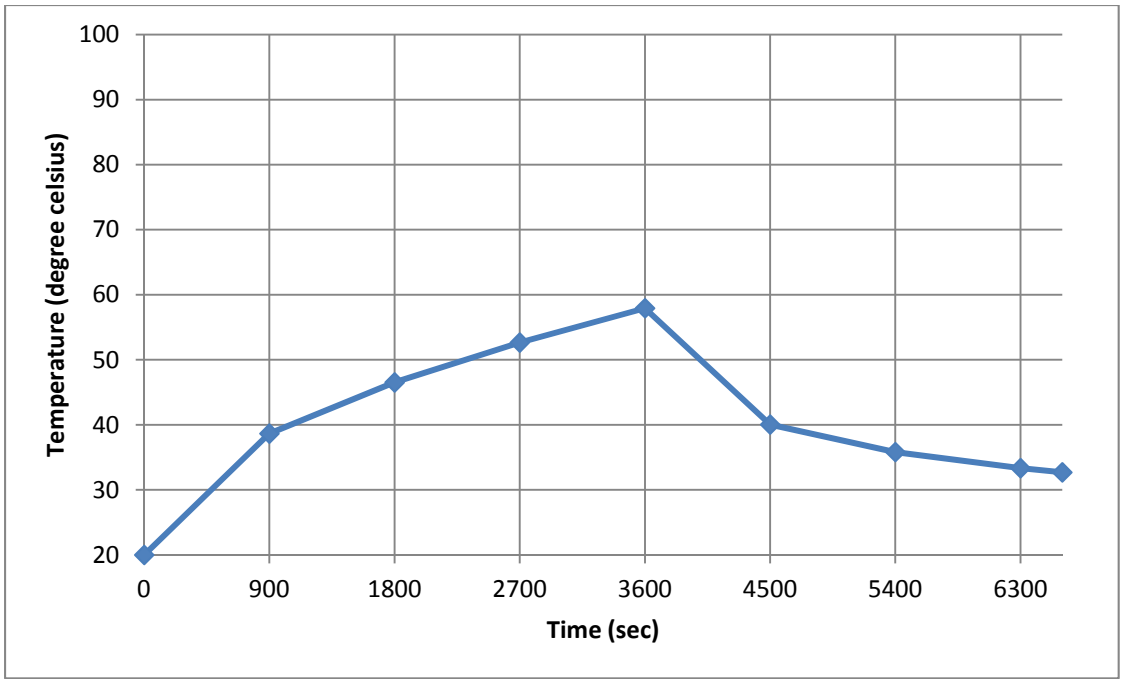

Figure 5.11: Results of Case 3 Temperature vs. Time curve for the SCC Wall

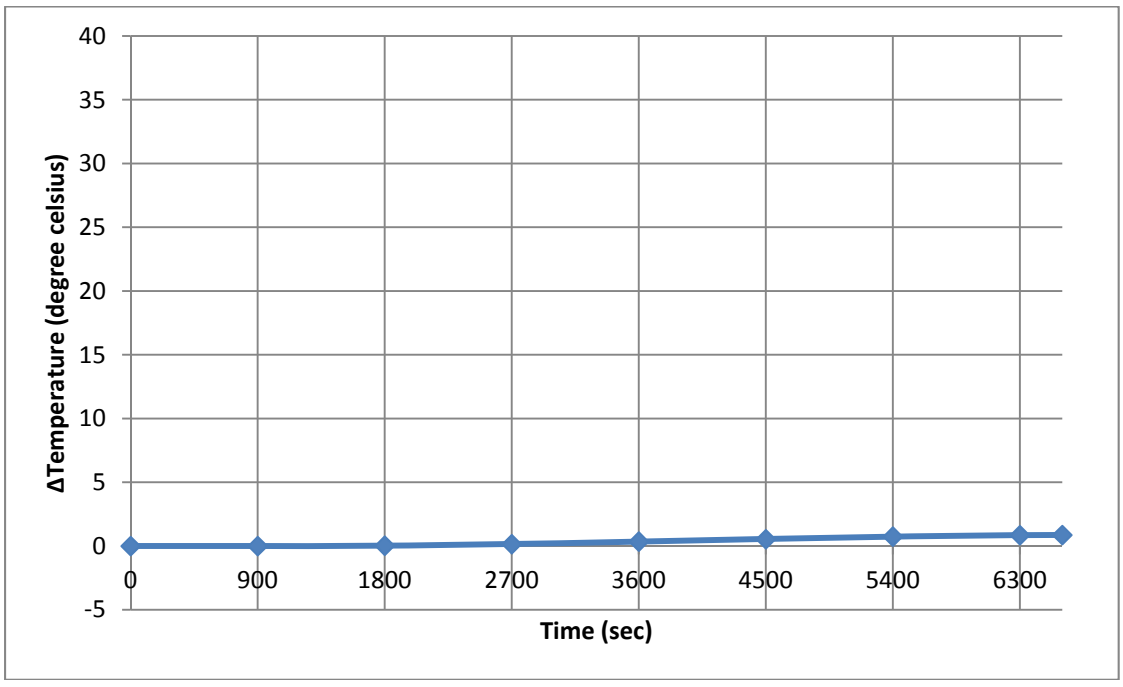

Figure 5.12: Results of Case 3, difference in Temperature vs. Time. The difference in temperature was calculated by the surface temperature difference between the defect and designated reference point

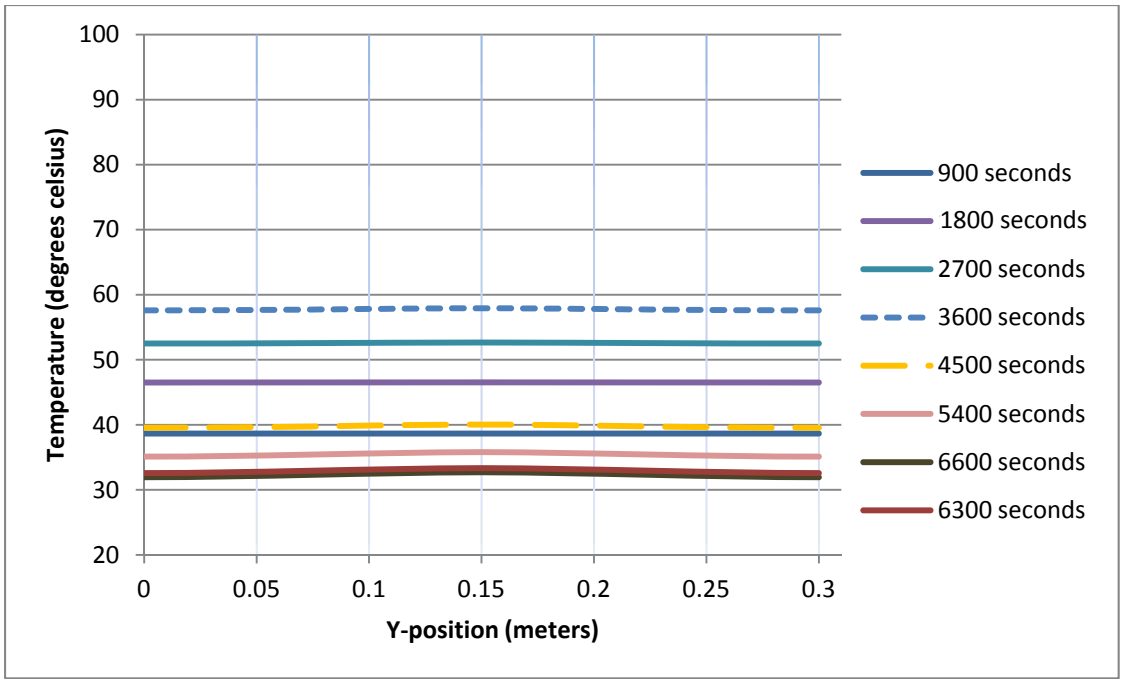

Figure 5.13: Case 3 surface temperatures versus the specimen's surface position in the y-axis, for the given heating and cooling durations

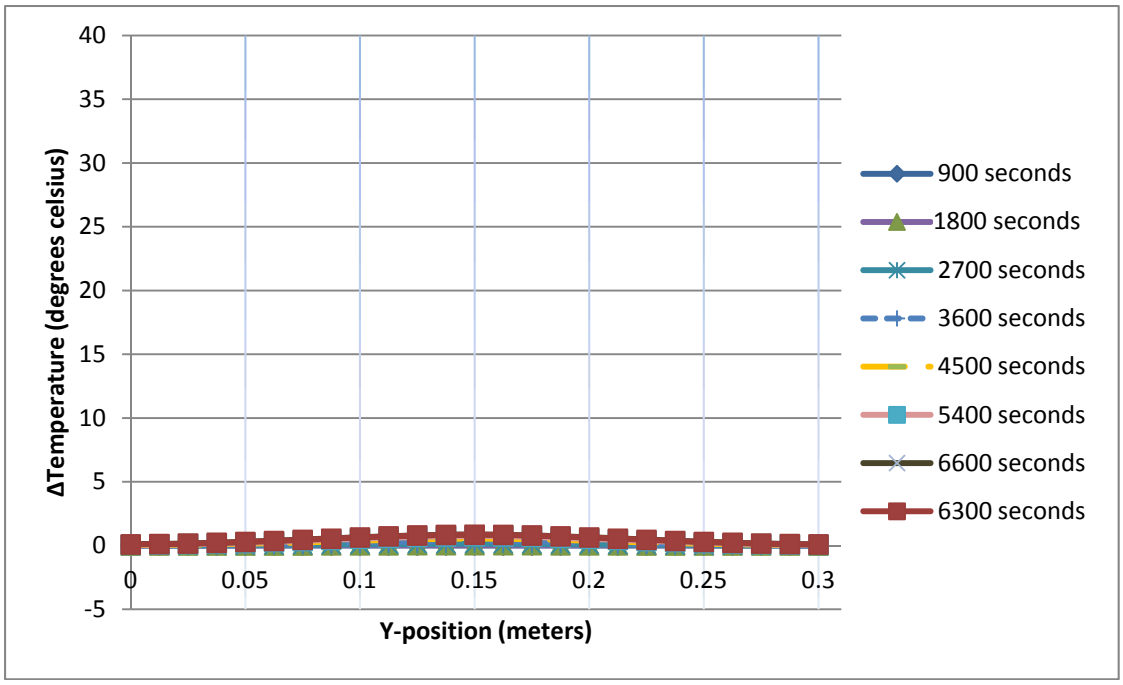

Figure 5.14: Case 3 difference in surface temperatures versus the specimen's surface position in the y-axis, for the given heating and cooling durations

5.6 CASE 4

Analysis Case 4 of this is study consisted of the same SCC wall model as Case 1, but with a defect depth of .0125 meters. In this analysis, a thermal surface heat flux (q) and time duration of the heat flux (t_h) were 625 $JT^{-1}L^{-2}$ and 3600 seconds respectively. The results of the maximum temperature occurrence on the surface of the specimen in respect to time are graphed in Figure 5.15. The maximum surface temperature experienced during the analysis was recorded at 57 ^{0}C, occurring at the end of the heating phase.

Figure 5.16 is a graph of the difference in surface temperature over the void as compared to a reference point on the specimen's surface. The graph shows that the maximum temperatures difference between the surface over the defect and the surface of an unaffected area of the specimen is approximately 18 ^{0}C. The time of which the maximum change in surface temperature occurred was recorded at 3600 seconds. This change of temperature is large significant when considering the detectability in temperature change when performing infrared thermography.

Figure 5.17 is a plot of Case 4 surface temperature versus the specimen's surface position in the y-axis. Six different specified times during the analysis were graphed in order to get an overall depiction of how the temperature varies across the width of the specimen. A maximum temperature occurring at the center of the specimen directly over the void was recorded at 57 ^{0}C. The temperature readings located in the regions over the defects, all have a noticeable temperature change during the heating phase and the initial cooling phase.

Figure 5.18 is the difference in surface temperature in the y-axis of orientation. This graph gives a better representation of the change in temperature with respect to an undisturbed reference point on the specimen's surface. Figure 5.18 shows a large difference in temperature between the defect and reference point at the recorded times between 900 to 4500 seconds. All of which could be easily detected during the infrared thermography test. The maximum change in temperature was recorded at 18 ^{0}C at the end of the heating phase.

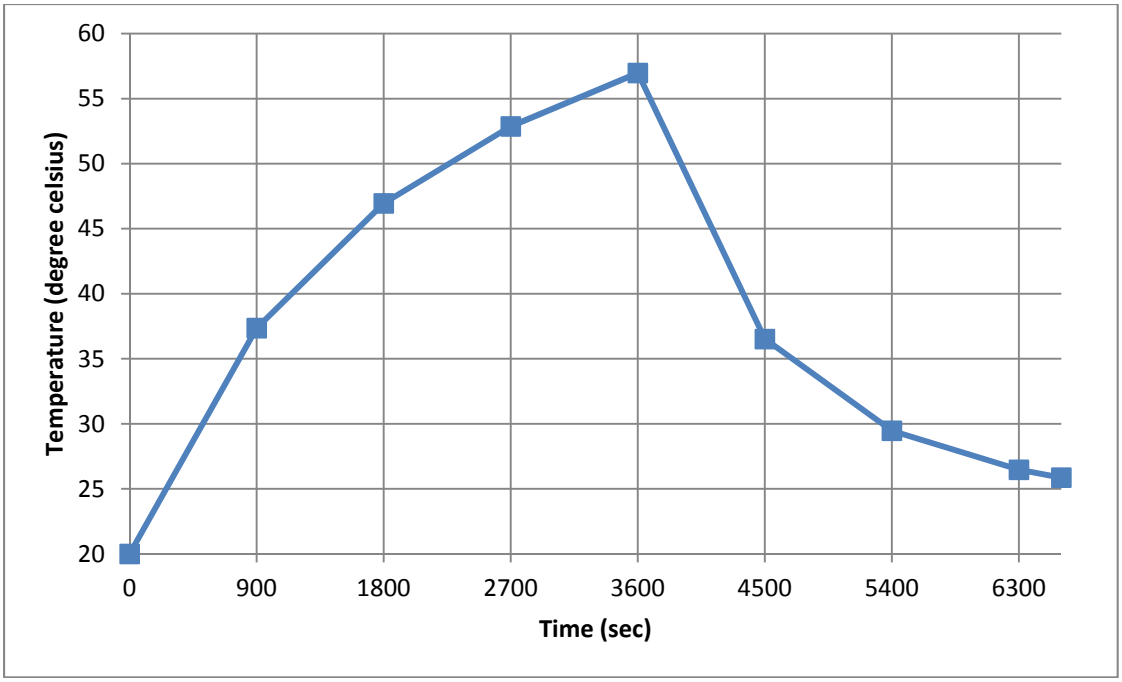

Figure 5.15: Results of Case 4 Temperature vs. Time curve for the SCC Wall

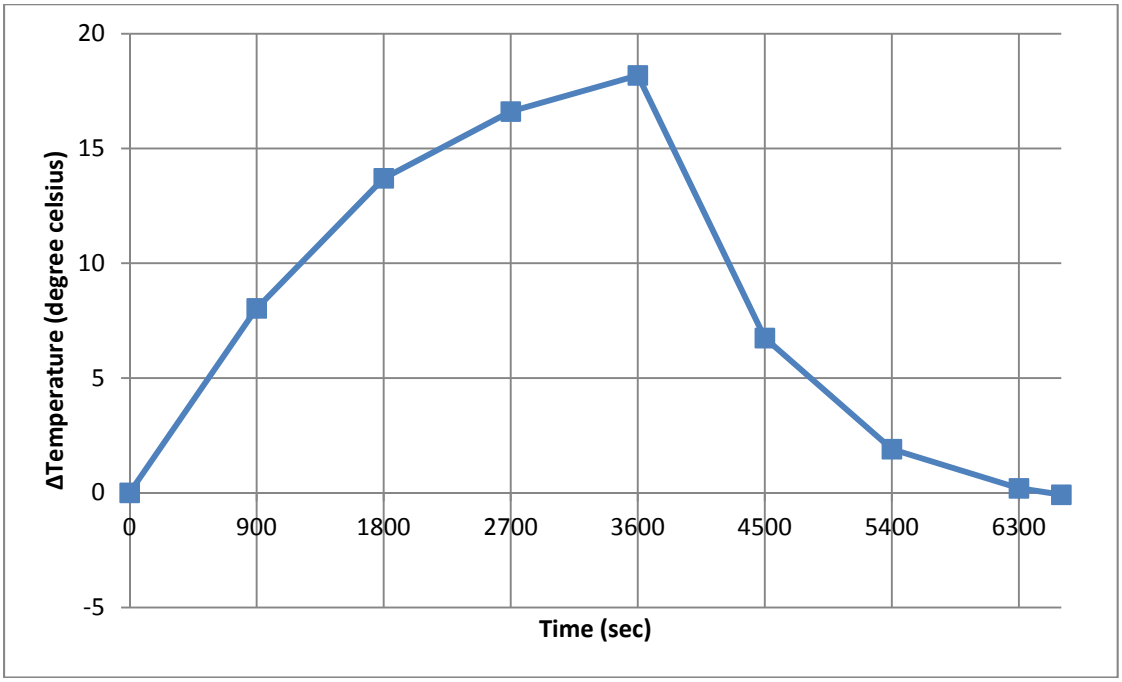

Figure 5.16: Results of Case 4, difference in Temperature vs. Time. The difference in temperature was calculated by the surface temperature difference between the defect and designated reference point

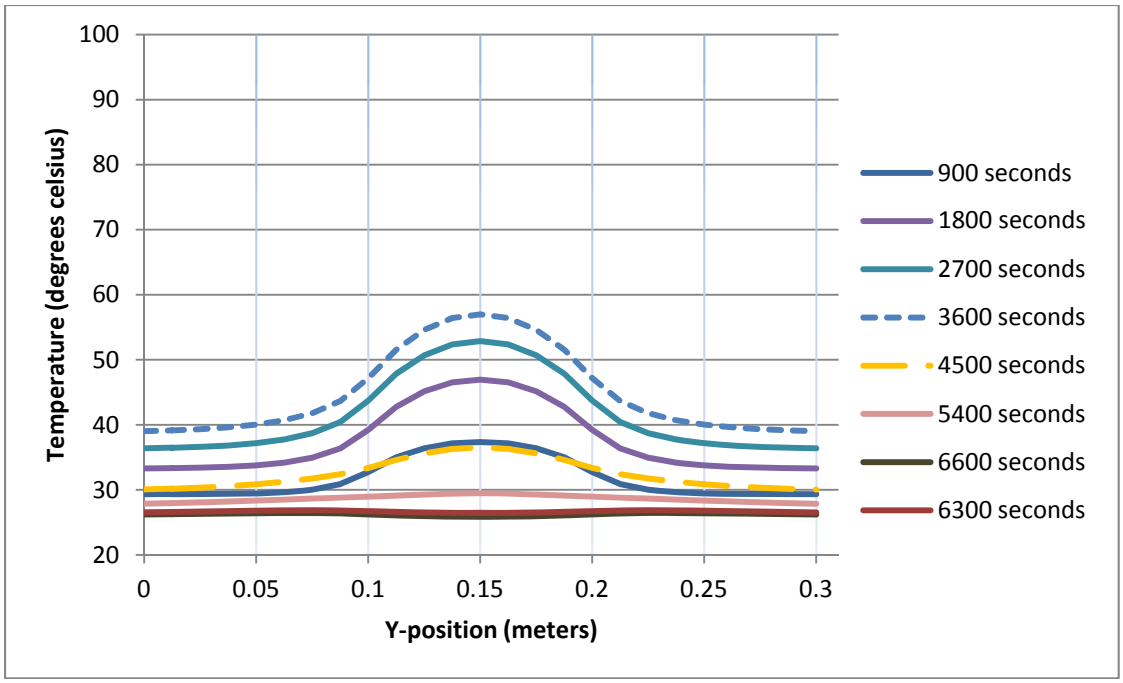

Figure 5.17: Case 4 surface temperatures versus the specimen's surface position in the y-axis, for the given heating and cooling durations

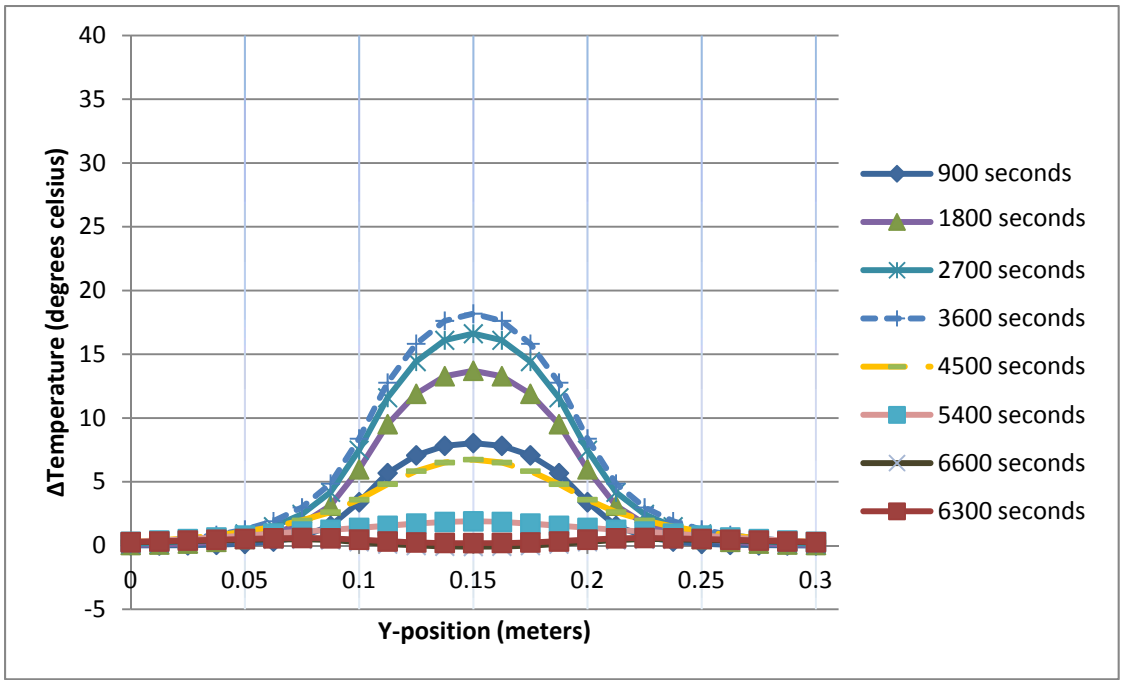

Figure 5.18: Case 4 difference in surface temperatures versus the specimen's surface position in the y-axis, for the given heating and cooling durations

5.7 CASE 5

Analysis Case 5 consisted of the same SCC wall model as Case 1, with a defect depth of .0375 meters. In this analysis, a thermal surface heat flux (q) and time duration of the heat flux (t_h) were 625 $JT^{-1}L^{-2}$ and 3600 seconds respectively. The results of the maximum temperature occurrence on the surface of the specimen in respect to time are graphed in Figure 5.19. The maximum surface temperature experienced during the analysis was recorded at 43 ^{0}C occurring at the end of the heating phase.

Figure 5.20 is a graph of the difference in surface temperature over the void as compared to a reference point on the specimen's surface. The graph shows that the maximum temperatures difference between the surface over the void and the surface of an unaffected area of the specimen is approximately 4 ^{0}C. The graph also shows a small temperature difference during the entire analysis for Case 5, meaning that the defect has a very low chance of being detected with the given testing parameters of Case 5.

Figure 5.21 is a plot of Case 5 surface temperature versus the specimen's surface position in the y-axis. The maximum temperature occurrence during this analysis was recorded at 43 ^{0}C at the center of the specimen. The temperature readings located in the regions over the defect has almost no noticeable temperature change during the entire analysis.

Figure 5.22 is the difference in surface temperature in the y-axis of orientation. This graph gives a better representation of the change in temperature with respect to an undisturbed reference point on the specimen's surface. The maximum difference in

surface temperature in the y-axis of orientation is approximately 4 ^{0}C. This small change in surface temperature illustrates that the detectability of a defect with the current parameters of Case 5 would probably not be detected.

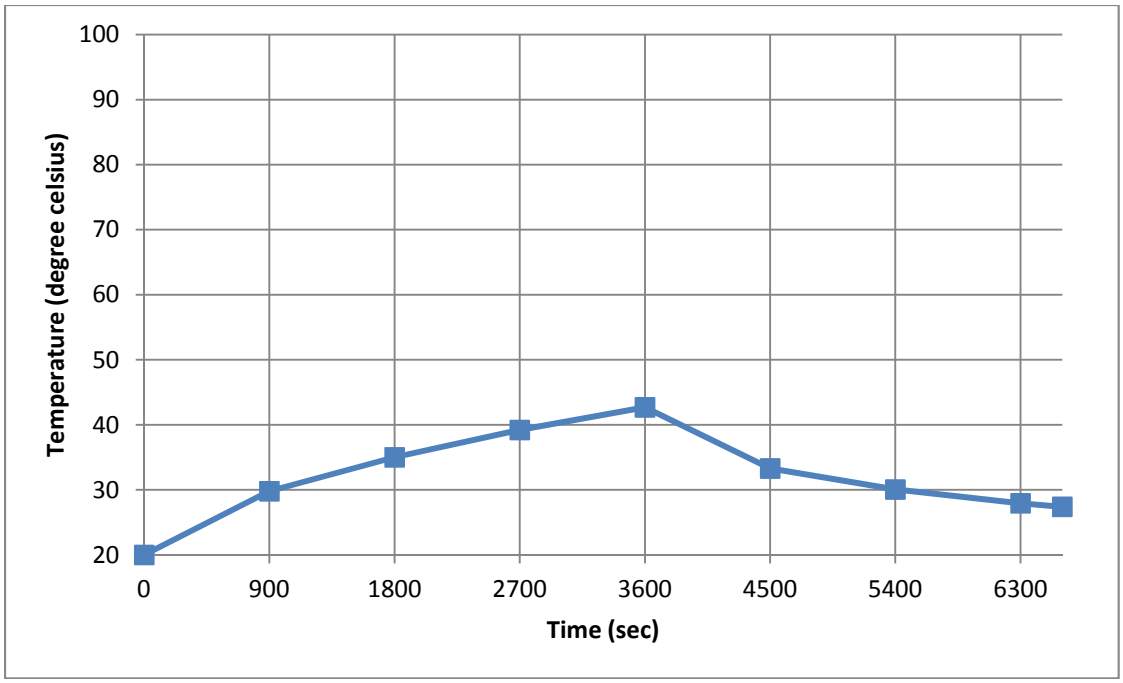

Figure 5.19: Results of Case 5 Temperature vs. Time curve for the SCC Wall

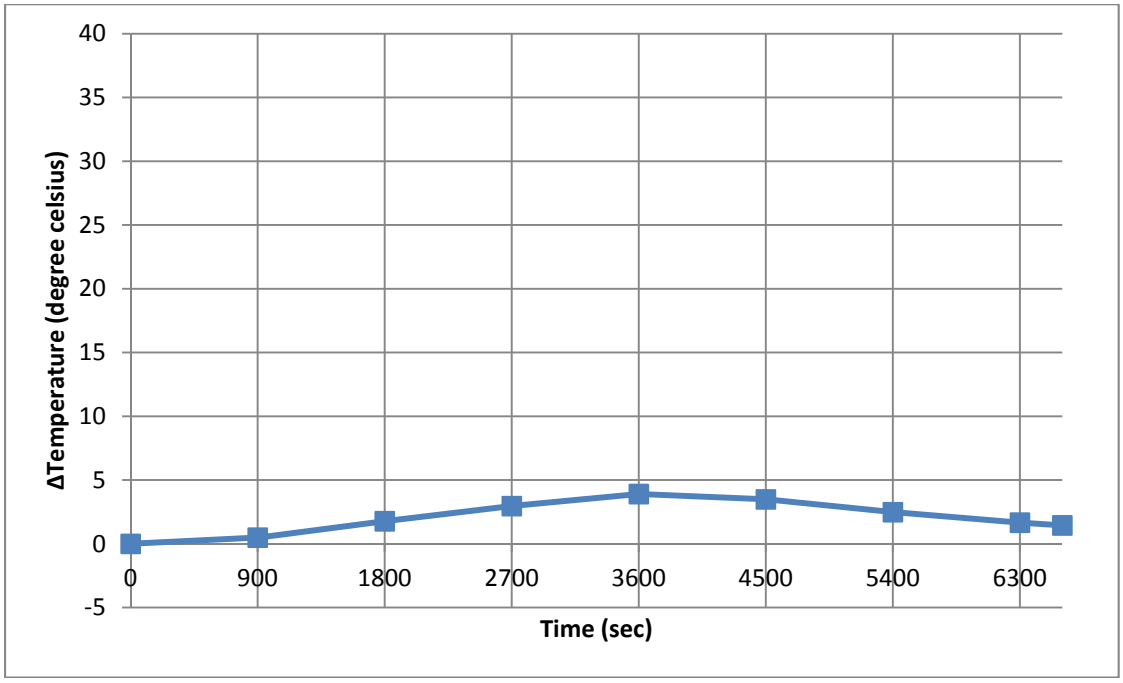

Figure 5.20: Results of Case 5, difference in Temperature vs. Time. The difference in temperature was calculated by the surface temperature difference between the defect and designated reference point.

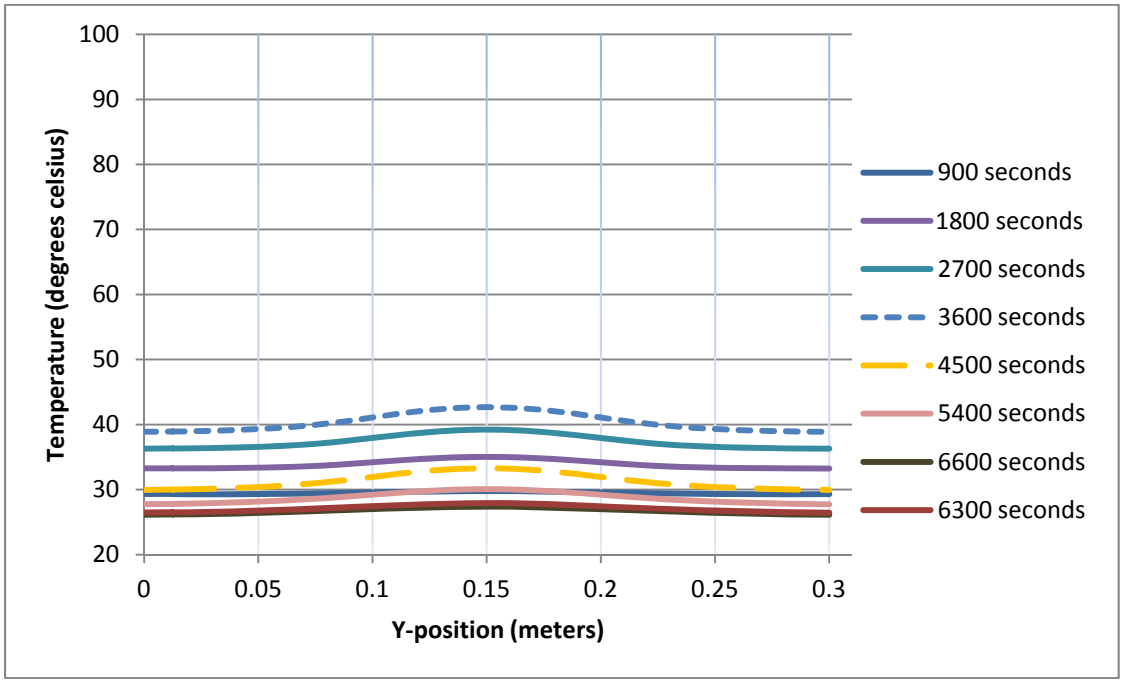

Figure 5.21: Case 5 surface temperatures versus the specimen's surface position in the y-axis, for the given heating and cooling durations

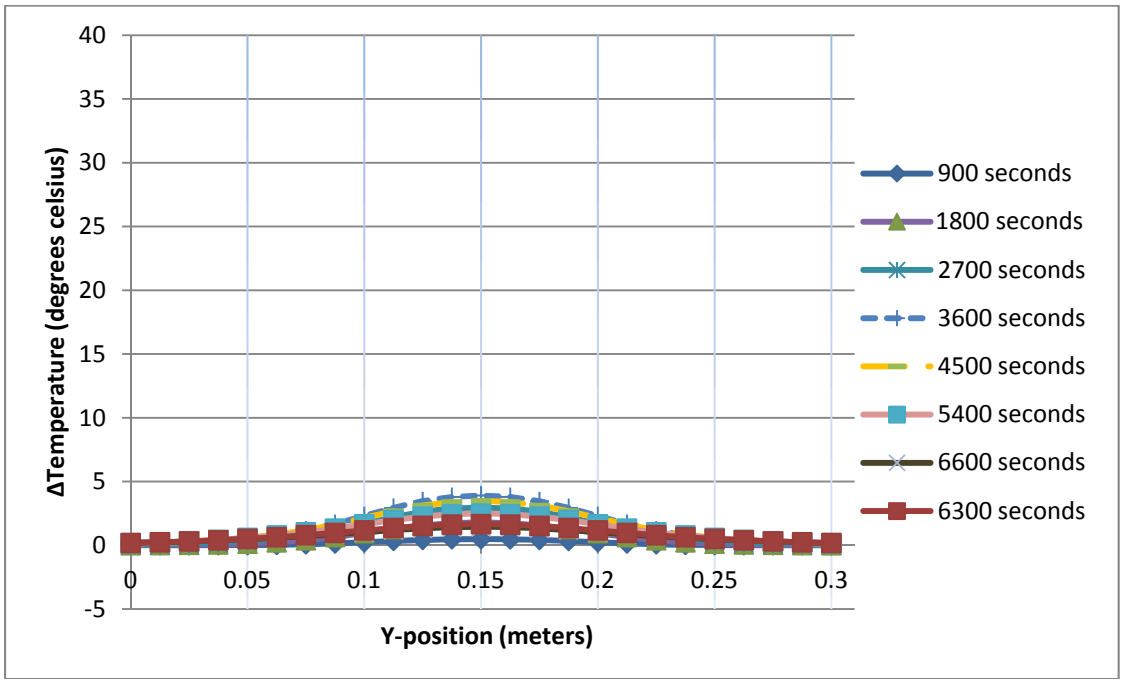

Figure 5.22: Case 5 difference in surface temperatures versus the specimen's surface position in the y-axis, for the given heating and cooling durations

5.8 CASE 6

Analysis Case 6 consisted of the same SCC wall model as Case 1, but with a defect depth of .0875 meters. In this analysis, a thermal surface heat flux (q) and time duration of the heat flux (t_h) were 625 $JT^{-1}L^{-2}$ and 3600 seconds respectively. The results of the maximum temperature occurrence on the surface of the specimen in respect to time are graphed in Figure 5.23. Figure 5.23 shows a relatively constant surface temperature throughout the analysis, with a maximum temperature of 39 ^{0}C.

Figure 5.24 is a graph of the difference in surface temperature over the defect as compared to a reference point on the specimen's surface. The graph shows that the maximum temperature difference between the surface over the defect and the surface of an unaffected area of the specimen is approximately 0.4 ^{0}C. This clearly shows that there is practically no change in temperature on the surface of the specimen during the entire Case 6 analysis.

Figure 5.25 is the difference in surface temperature in the y-axis of orientation. This graph represents the change in temperature with respect to an undisturbed reference point on the specimen's surface. The six different specified times recorded during the analysis were all straight lines starting at its initial surface temperature. This further shows that there is no change in temperature along the surface of the specimen. Figure 5.26 reinforces this with a maximum change in the surface temperature along the y-axis of orientation of only 0.4 ^{0}C.

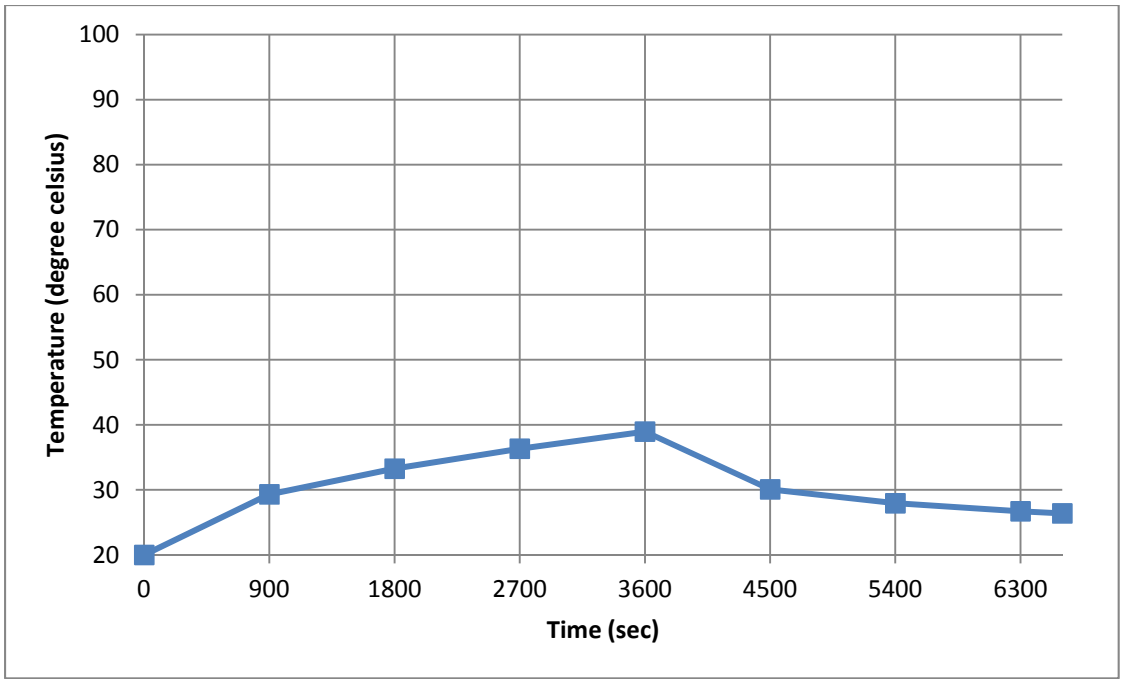

Figure 5.23: Results of Case 6 Temperature vs. Time curve for the SCC Wall

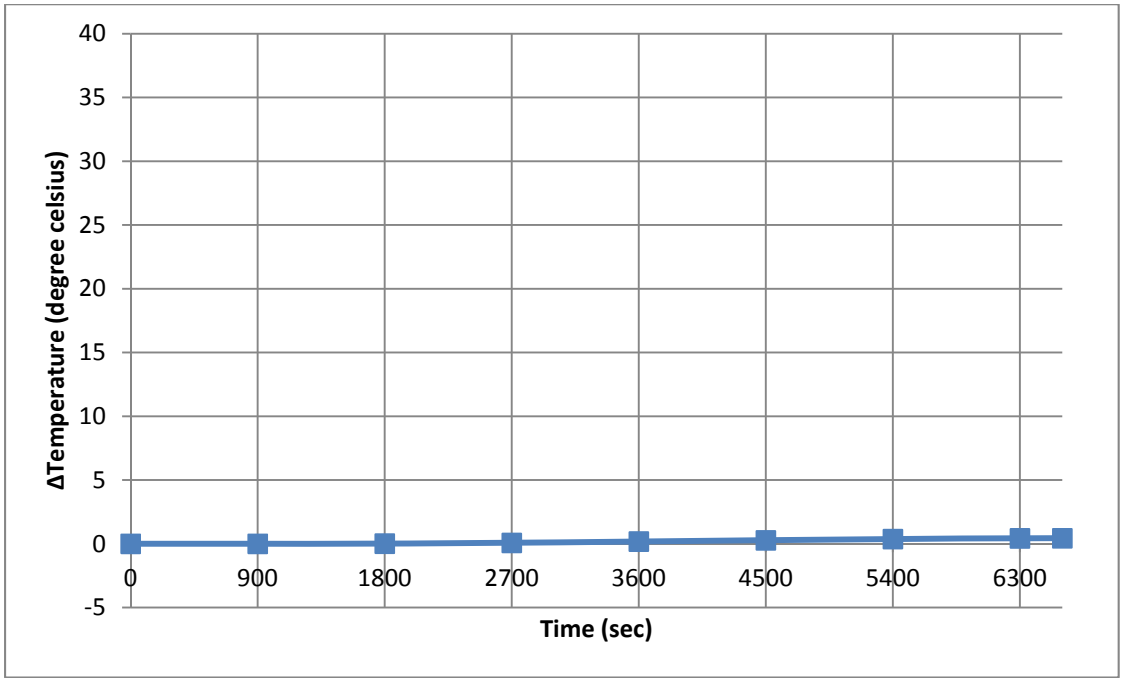

Figure 5.24: Results of Case 6, difference in Temperature vs. Time. The difference in temperature was calculated by the surface temperature difference between the defect and designated reference point

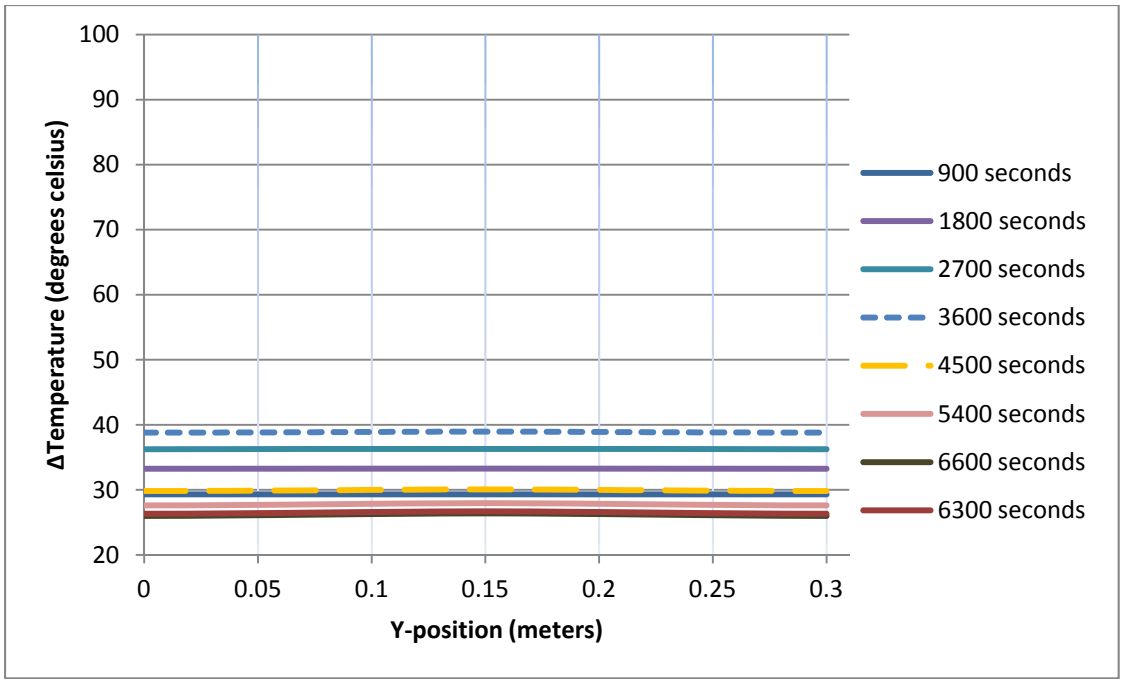

Figure 5.25: Case 6 surface temperatures versus the specimen's surface position in the y-axis, for the given heating and cooling durations.

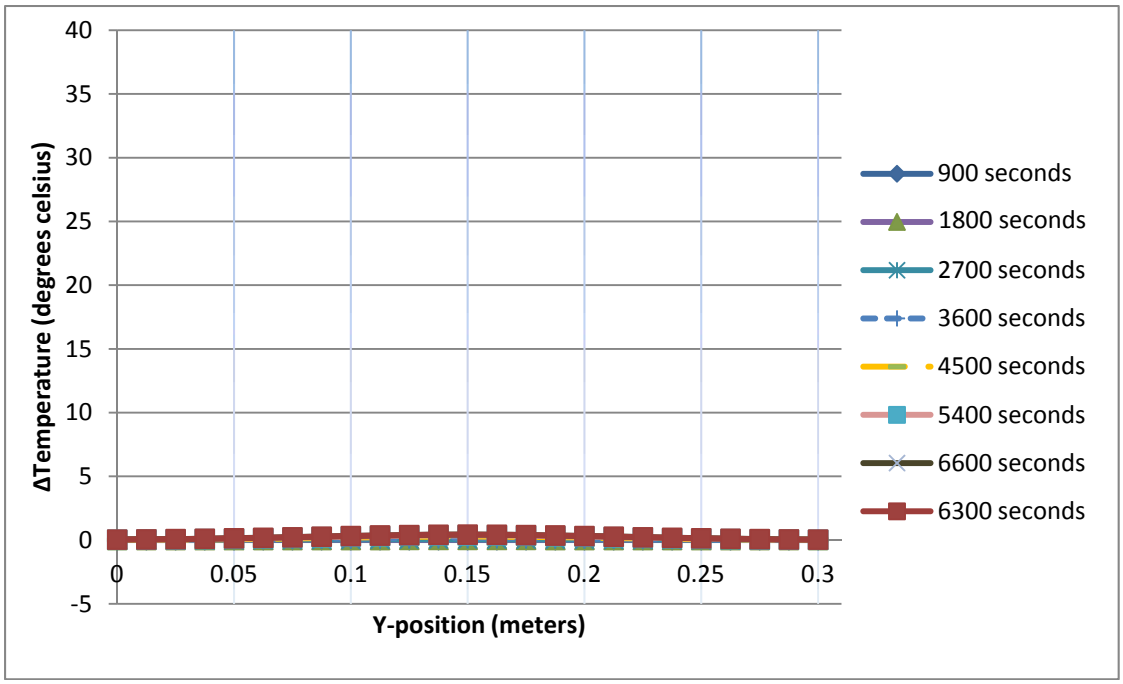

Figure 5.26: Case 6 difference in surface temperatures versus the specimen's surface position in the y-axis, for the given heating and cooling durations

5.9 CASE 7

Analysis Case 7 consisted of the same SCC wall model as Case 1, with a defect depth of 0.0125 meters. In this analysis, a thermal surface heat flux (q) and time duration of the heat flux (t_h) were 625 $JT^{-1}L^{-2}$ and 900 seconds respectively. The results of the maximum temperature occurrence on the surface of the specimen in respect to time are graphed in Figure 5.27. The maximum surface temperature experienced during the analysis was recorded at 55 ^{0}C.

Figure 5.28 is a graph of the difference in surface temperature over the defect as compared to a reference point on the specimen's surface. The graph shows that the maximum temperature difference between the surface over the defect and the surface of an unaffected area of the specimen is approximately 16 ^{0}C. The time at which the maximum difference in surface temperature occurred was recorded at 900 seconds, which is the end of the heating phase in this Case. This change of temperature is significant when considering the detectability in temperature change when performing infrared thermography, which will give a high probability of detecting the defect.

Figure 5.29 is a plot of Case 7 surface temperature versus the specimen's surface position in the y-axis. Six different specified times during the analysis were graphed, with the maximum surface temperature occurring at 900 seconds. The maximum surface temperature recorded was 55 ^{0}C. The recorded temperatures located in the regions over the defects have a noticeable temperature change during the analysis, which indicates that the capability of detecting defects with the current parameters of Case 7 is possible.

Figure 5.30 is the difference in surface temperature in the y-axis of orientation, for the six specified times. This graph shows a large difference in temperature between the defect and reference point during the analysis. The maximum change in temperature was recorded at 16.2 ^{0}C at the end of the heating phase.

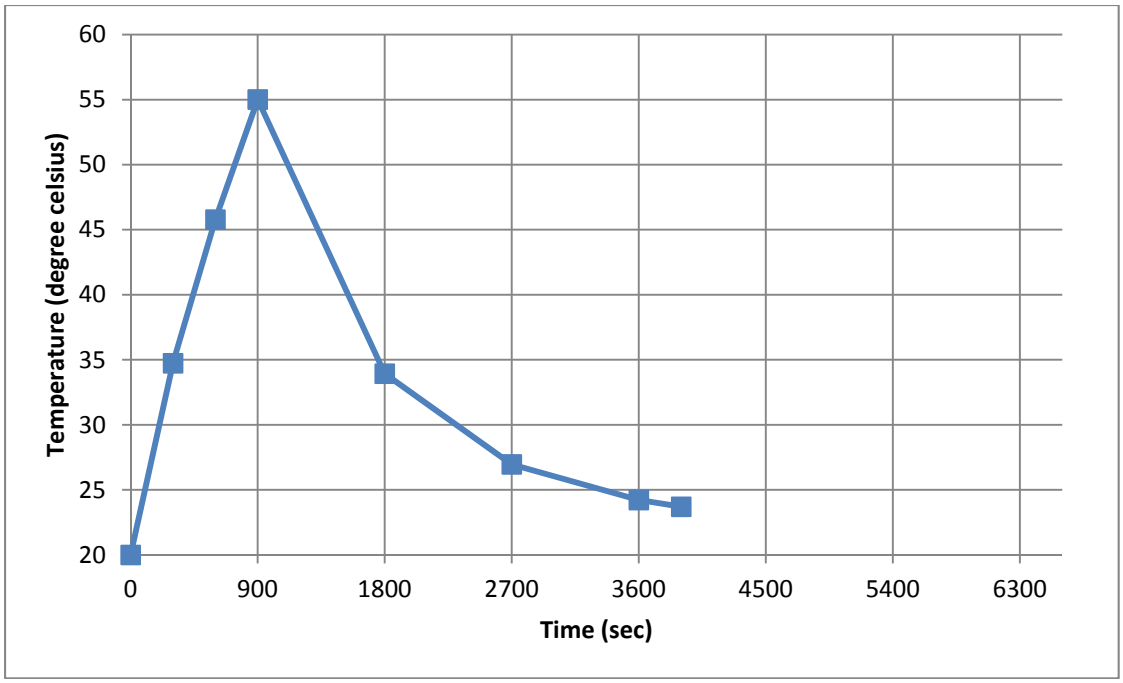

Figure 5.27: Results of Case 7 Temperature vs. Time curve for the SCC Wall

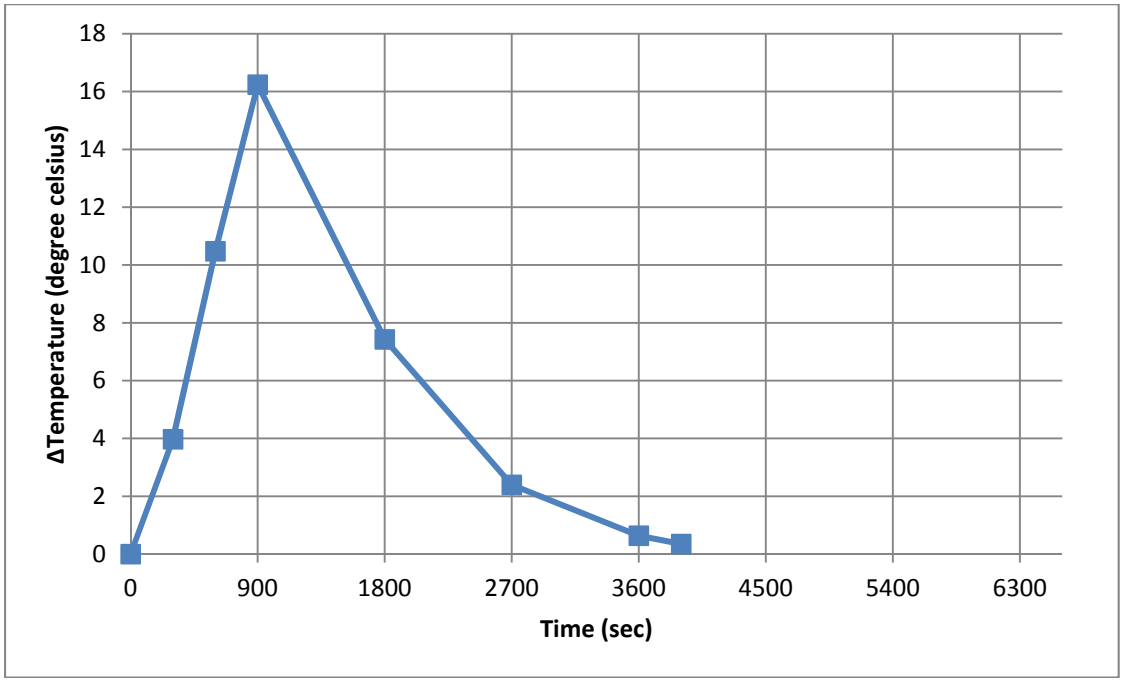

Figure 5.28: Results of Case 7, difference in Temperature vs. Time. The difference in temperature was calculated by the surface temperature difference between the defect and designated reference point

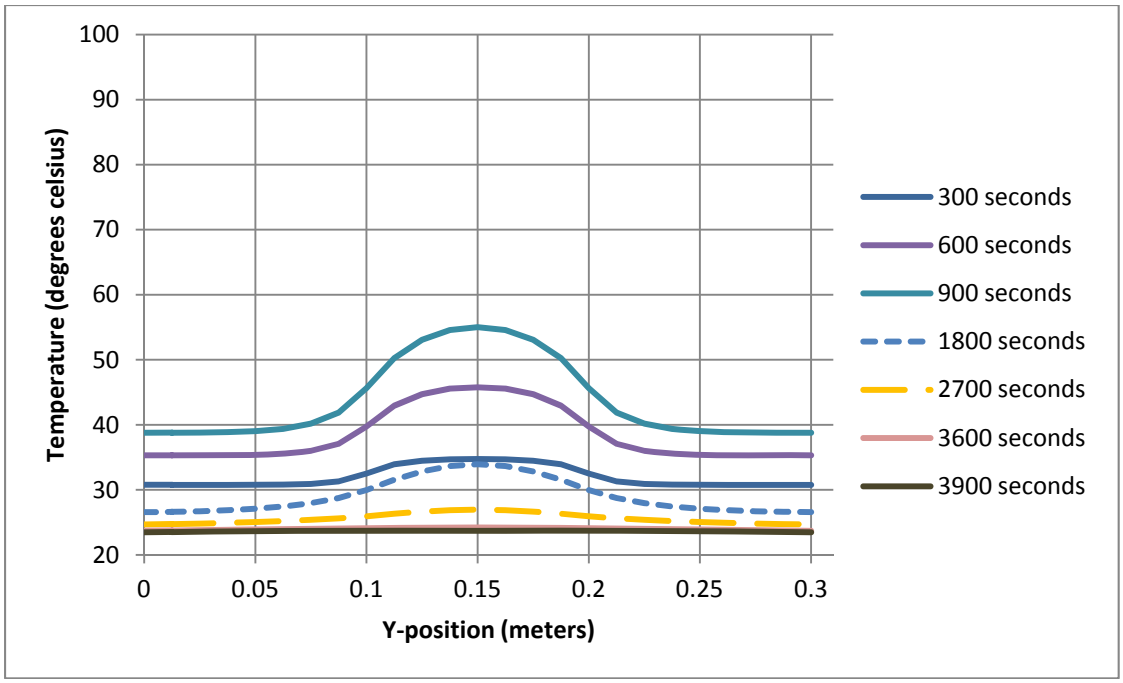

Figure 5.29: Case 7 surface temperatures versus the specimen's surface position in the y-axis, for the given heating and cooling durations

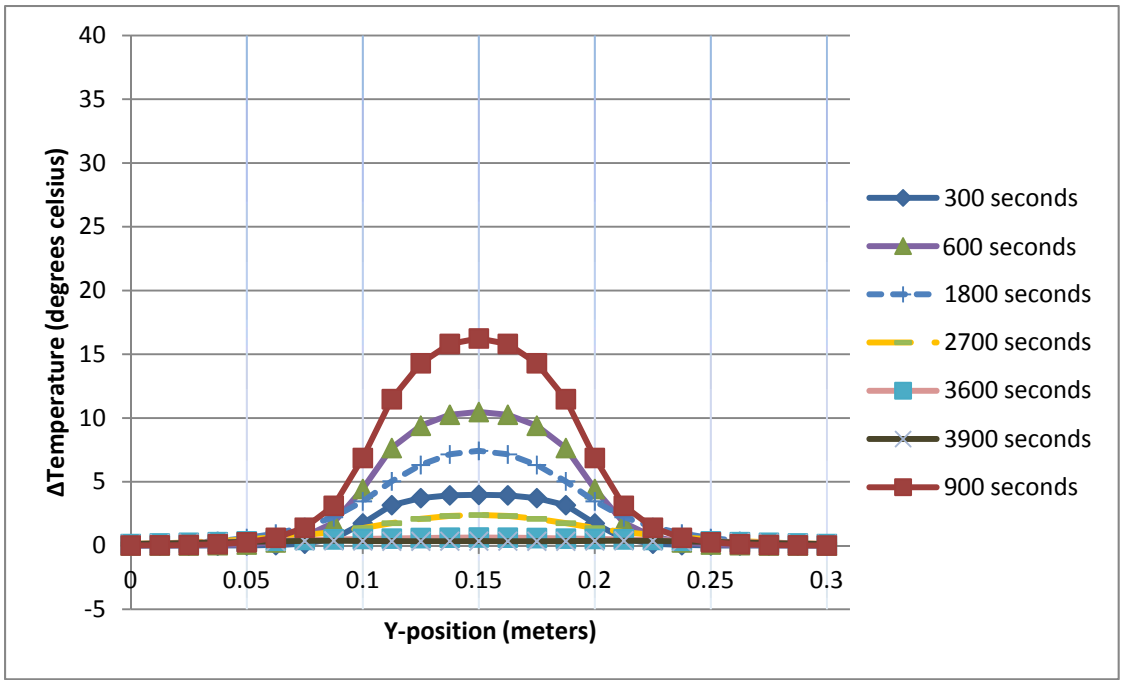

Figure 5.30: Case 7 difference in surface temperatures versus the specimen's surface position in the y-axis, for the given heating and cooling durations

5.10 SUMMARY OF CASES

Finite element analyses of the SCC wall for the parametric Cases defined in Table 5.1, shows that each parameter does have a significant impact on the detection of defects within the concrete subsurface. The graphs that show the temperature difference on the surface of the specimen, directly reflects on how well a defect can be seen by the infrared camera. And as expected, the parameters such as the increase in depth of the defect, decrease in the heating temperature and duration of the heating phase all reduce the change in the surface temperature as seen on the graphs plotted for Case 1 thru Case 7.

CHAPTER 6
DISCUSSION

6.1 INTRODUCTION

This chapter discusses the influences of the change in the depth of the defect, heating intensity and heating duration, on the detectability of the defects within the concrete subsurface.

6.2 INFLUENCE OF FLAW DEPTH

The influence of the flaw depth correlates directly to what was seen in the results of the BAM test, and what was expected based on Fourier's law of thermal conduction:

$$q = -k \cdot \frac{\mathrm{d}T}{\mathrm{dx}}$$

Fourier's law of heat conduction states that the rate of heat transfer through a material is proportional to the temperature gradient within the object's cross-section. Therefore, the larger the distance dx is, the larger the decrease in heat conduction through a specimen is. The effect of this is less heat penetrating through the material, reducing the ability for heat to flow through the region of the defect or abnormalities. This reduces the temperature change between the surface temperature above the defect and the surface temperature over an area unaffected by the flaw. To demonstrate this, the change in flaw depth versus temperature has been plotted for the parametric cases studied in Chapter 5. Plotted on Figure 6.1, Figure 6.3 and Figure 6.5 are three graphs each representing the surface temperature versus the specimen surface position across the y-orientation at heating intensity of 1250 $Js^{-1}m^{-2}$. Each figure contains three graphs analogous to the three depths of the defects, and the three figures each correspond to the time of which the data was recorded.

Figure 6.1 shows the surface temperature over the defects at 1800 seconds in the analysis. During the earlier stages of the analysis, Figure 6.1 shows that only the defect located closest to the surface showed a large surface temperature change over the area of the defect. This can be seen more clearly on Figure 6.2 which shows the difference in surface temperature between the surface over the defect and a designated unaffected area on the surface of the specimen. At the depth of .0125 meters, a maximum change in temperature was recorded at approximately 27.6 ^{0}C on Figure 6.2. The defect located at the depth of .0375 meters has a change in surface temperature of approximately 3.5 ^{0}C, which shows a large temperature difference between the two defect depths. Similarly, Figure 6.3 shows the surface temperature over the defects at 3600 seconds in the finite element model. During this time in the analysis, the surface temperature reaches its maximum temperature, thus optimizing the detection of the defect. Figure 6.4 does show that the defects located at .0125 and .0375 meters both have a change in surface temperature greater than 5 ^{0}C. Still the deepest defect located at the depth of .0875 meters has almost no change in surface temperature at the defect. Figure 6.5 illustrates the surface temperature over the defects near the ending of the analysis at 5400 seconds. In both Figure 6.5 and Figure 6.6, the graphs for all depths of the defects shows that most of the thermal energy in the system is diminished showing no change in surface temperature across the entire surface of the specimen. Figures 6.7 through Figure 6.12 are identical to Figure 6.1 through Figure 6.6, except for a heating intensity of 625 $Js^{-1}m^{-2}$.

6.3 INFLUENCE OF HEATING INTENSITY

The influence of the external heating source intensity was studied as one of the parameters in the analyses. The two external heating sources used in the analyses corresponded to heat flux intensities of 1250 $Js^{-1}m^{-2}$ and 625 $Js^{-1}m^{-2}$. In Figure 6.13 and Figure 6.14, the difference in surface temperature versus time was graphed for six cases. Figure 6.13 has six graphs plotted, each representing the three defect depths and the two heat flux intensities applied to the specimen during that analysis. This is shown in the figure by the solid lines representing the heat flux intensity of 1250 $Js^{-1}m^{-2}$ and the dashed lines representing the heat flux intensity of 625 $Js^{-1}m^{-2}$. The graphs plotted on Figure 6.13 also show the temperature difference between the surface temperature directly over the center of the defect and the surface temperature at the edge of the defect. Figure 6.14 is identical to Figure 6.13, but with a change in the locations of the temperature readings. In Figure 6.14, the surface temperature is obtained by the difference between the surface temperature at the edge of the defect and the surface temperature at a reference point designated at a surface location that is unaffected by the defect.

Both figures below clearly show the temperature difference between the two heating intensities. For example, in Figure 6.13 the maximum change in surface temperature with a heat flux of 1250 $Js^{-1}m^{-2}$ and at a defect depth of .0125 meters is approximately 19 ^0C. The maximum change in surface temperature with a heat flux of 625 $Js^{-1}m^{-2}$ and at a defect depth of .0125 meters is approximately 8.2 ^0C. Figures 6.13 also shows the change in surface temperature for both heating intensities become smaller as the depth of the defects increase, eventually showing almost zero change in surface temperature

between both heating intensities. Figure 6.14 follows the same characteristics as Figure 6.13, but with slight different temperature reading for each graph.

6.4 INFLUENCE OF HEATING INTENSITY AND HEATING DURATION

Plotted on Figure 6.15 are the graphs of each Case that contains a defect at the depth of .0125 meters. As shown in the figure, there are three Cases of which the depth was located at .0125 meters. Two Cases had similar heating temperatures at 1250 $Js^{-1}m^{-2}$ and the other Case with only half of the heating temperature of the other two Cases. Similarly, one of the Cases with a heating source of 1250 $Js^{-1}m^{-2}$ also had 900 seconds of heating time rather than the 3600 seconds of heating time given in the other two Cases. As shown in the Figure below, each alteration of the parameters mention above had an impact in increase or decreasing the surface temperature.

Plotted on Figure 6.16 are the graphs of each Case that contains a defect at the depth of .0375 meters. In Figure 6.16, there were two different heating intensities graphed. Case 2 with a heat flux of 1250 $Js^{-1}m^{-2}$ and Case 5 with half of the heat flux of Case 2. The graphs plotted on Figure 6.16 and Figure 6.15 show a significant difference between the changes in surface temperature. The figures show that even with a small change in the defect's depth, a large impact on the surface temperature occurs. The heat flux and heating duration both also have an impact, but the two figures clearly show that the depth of the defect has a major influence on whether or not the flaw can be detected. In all of the cases graphed in Figure 6.15, the temperature change on the surface is large enough to be theoretically detected by an infrared camera. In Figure 6.16, Case 2 is barely greater than 5 ^0C, and if Case 3 or Case 6 were plotted (containing defect depth

3), the change in surface temperatures would all be well below 5 ^{0}C, making the detection of the defects unlikely.

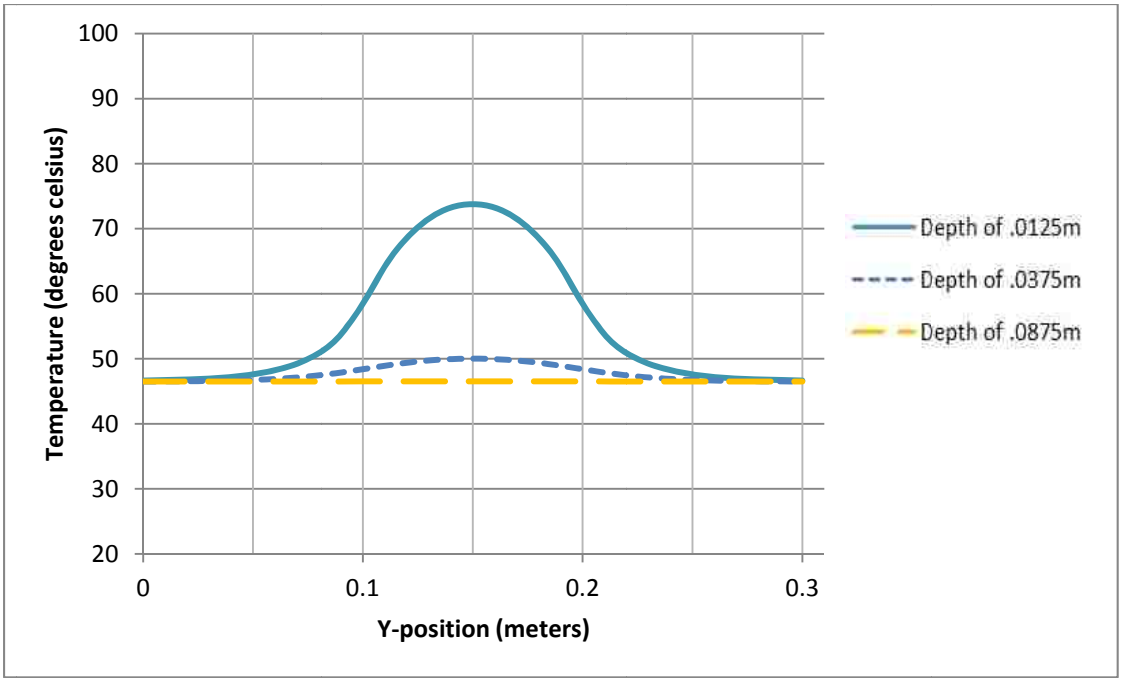

Figure 6.1: Surface temperatures in the Y-axis of orientation over the defect at 1800 seconds and a heat flux of 1250 $Js^{-1}m^{-2}$

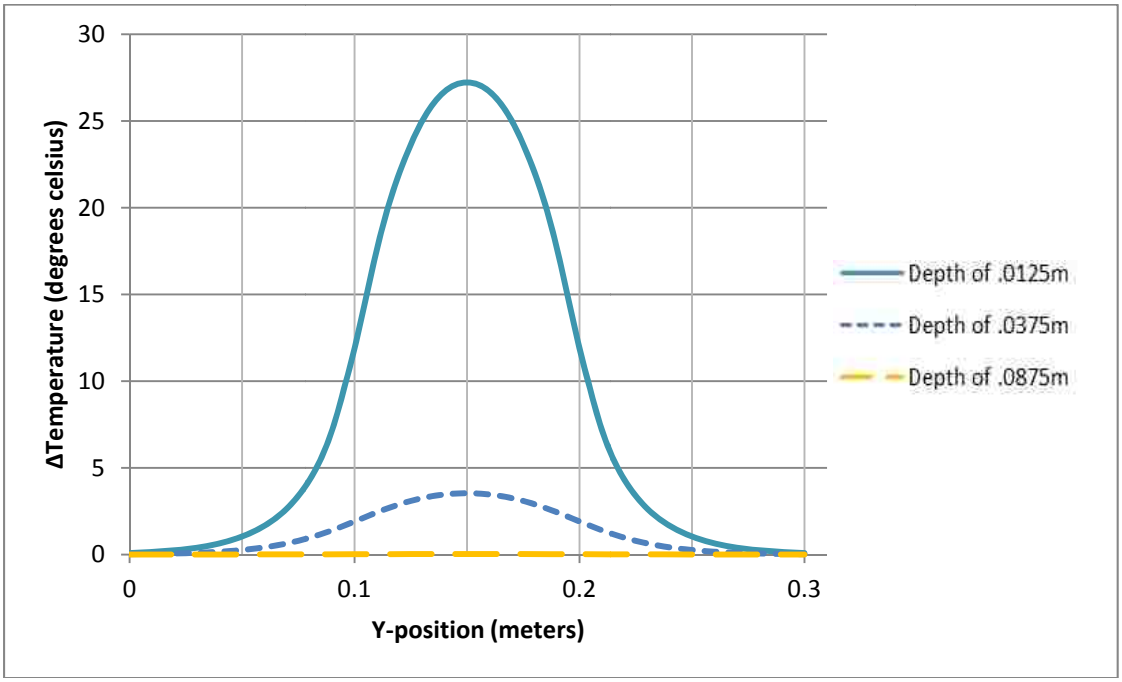

Figure 6.2: The difference in surface temperatures in the Y-axis of orientation over the defect at 1800 seconds and a heat flux of 1250 $Js^{-1}m^{-2}$

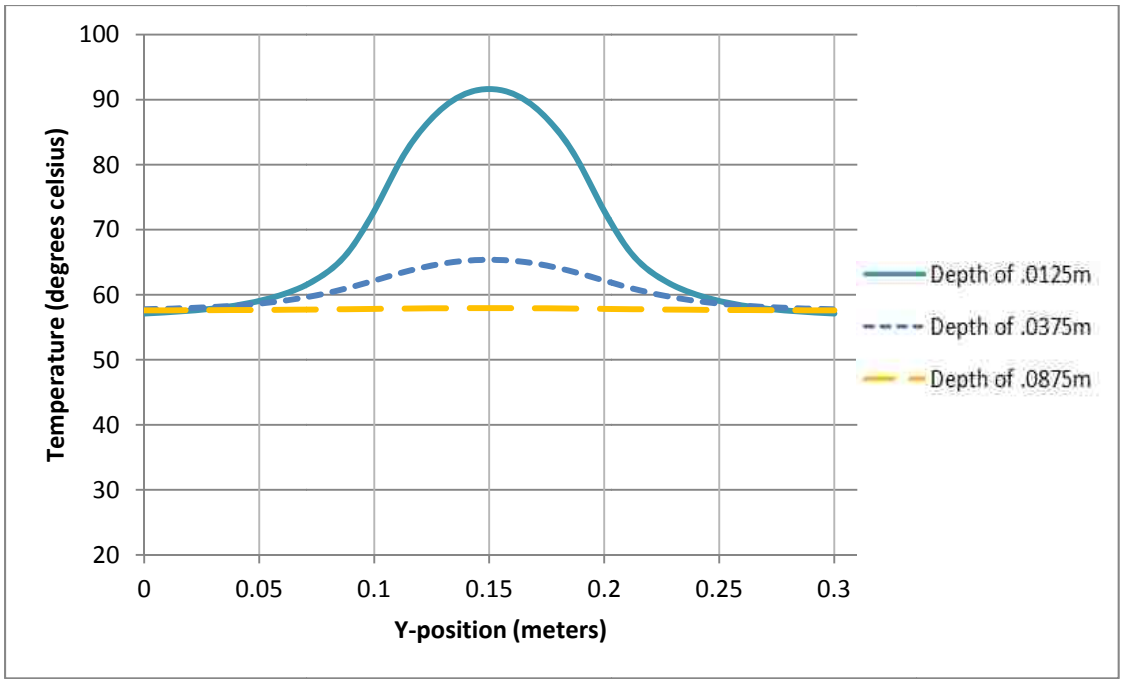

Figure 6.3: Surface temperatures in the Y-axis of orientation over the defect at 3600 seconds and a heat flux of 1250 $Js^{-1}m^{-2}$

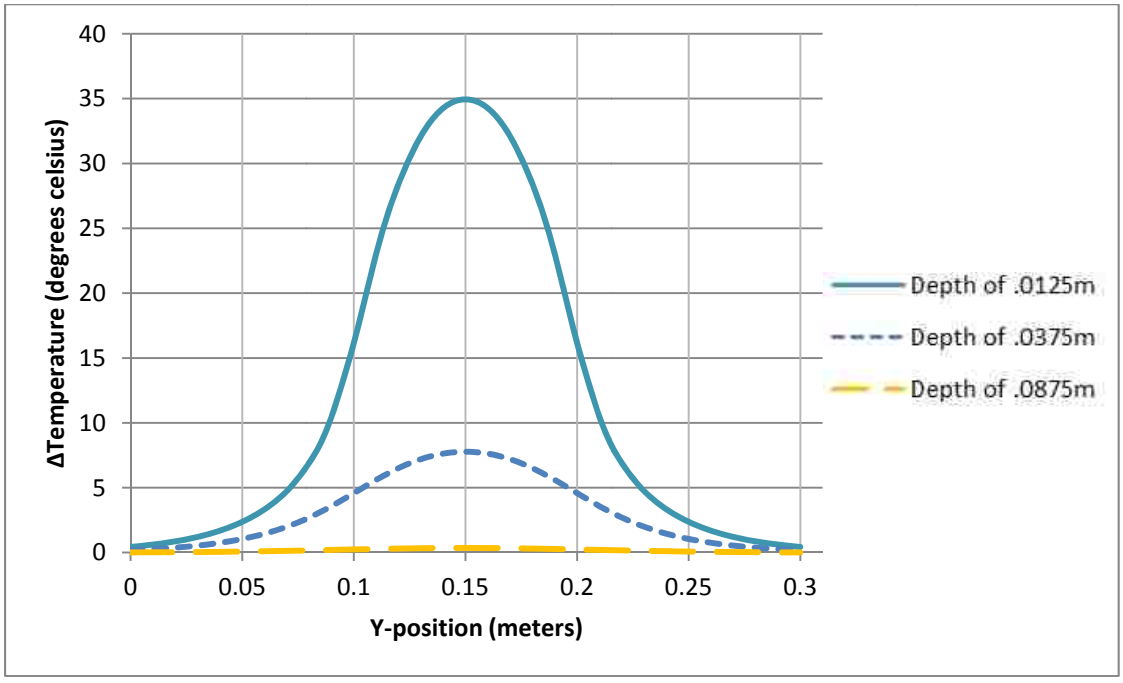

Figure 6.4: The difference in surface temperatures in the Y-axis of orientation over the defect at 3600 seconds and a heat flux of 1250 $Js^{-1}m^{-2}$

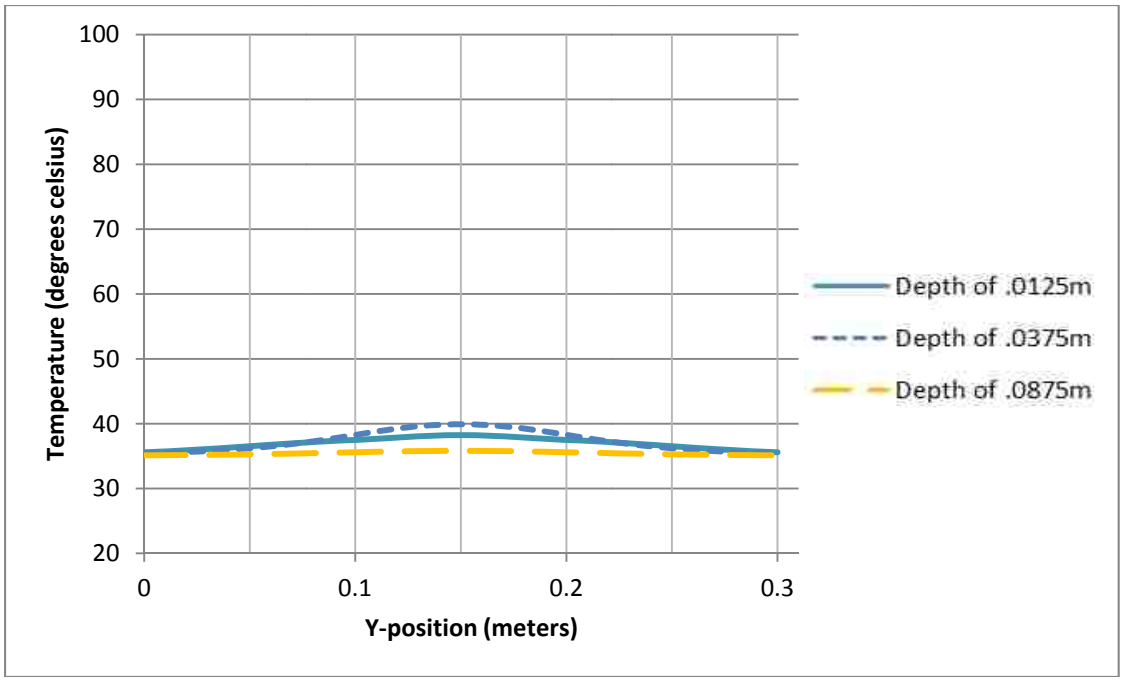

Figure 6.5: Surface temperatures in the Y-axis of orientation over the defect at 5400 seconds and a heat flux of 1250 $Js^{-1}m^{-2}$

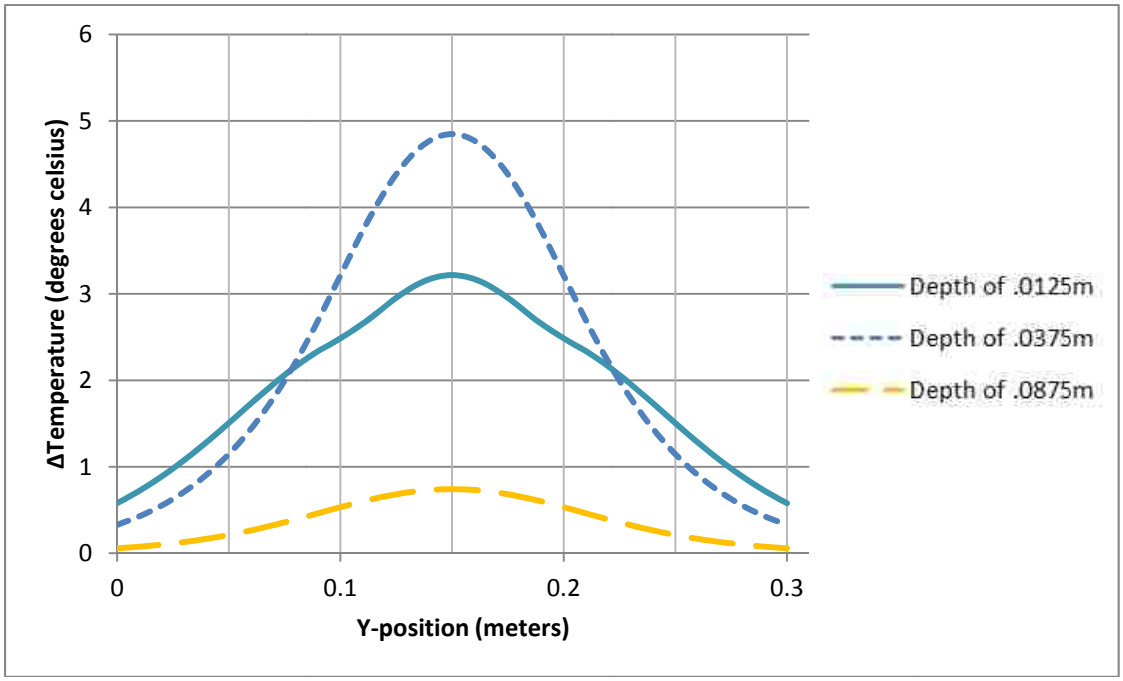

Figure 6.6: The difference in surface temperature in the Y-axis of orientation over the defect at 5400 seconds and a heat flux of 1250 $Js^{-1}m^{-2}$

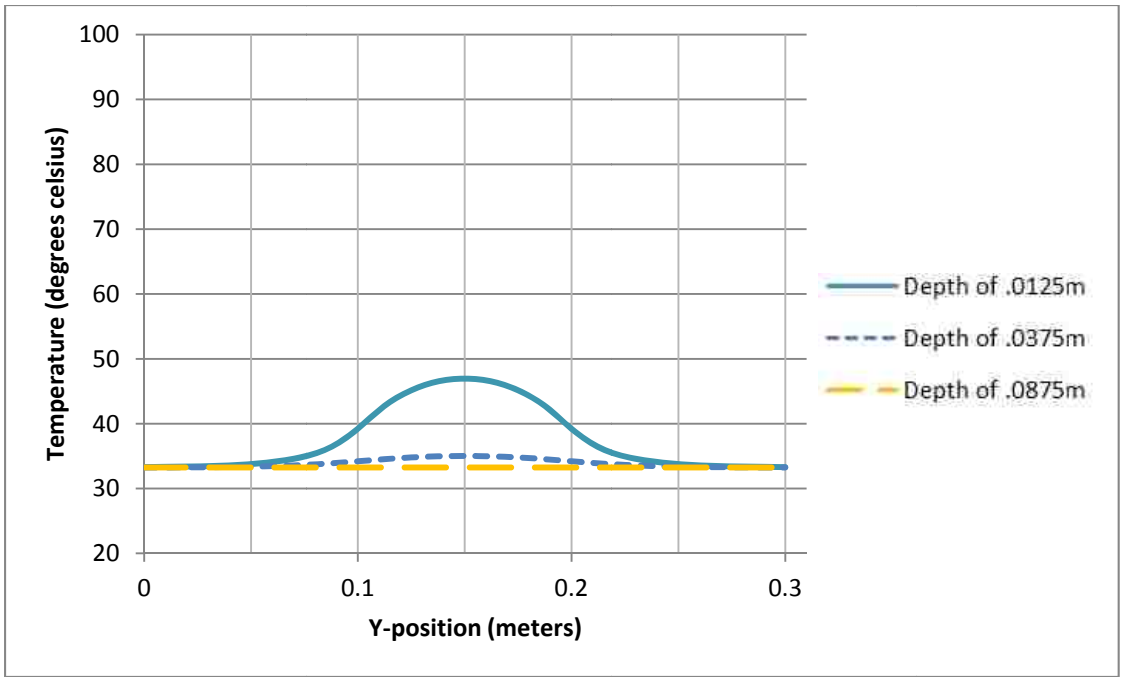

Figure 6.7: Surface temperatures in the Y-axis of orientation over the defect at 1800 seconds and a heat flux of 625 $Js^{-1}m^{-2}$

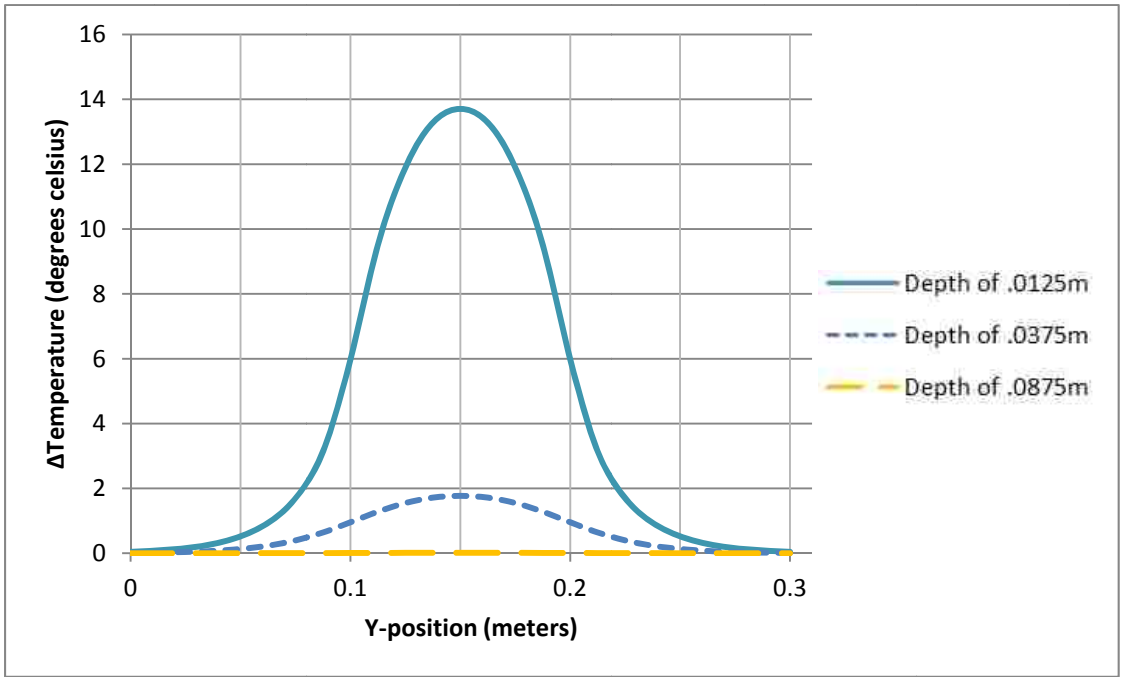

Figure 6.8: The difference in surface temperature in the Y-axis of orientation over the defect at 1800 seconds and a heat flux of 625 $Js^{-1}m^{-2}$

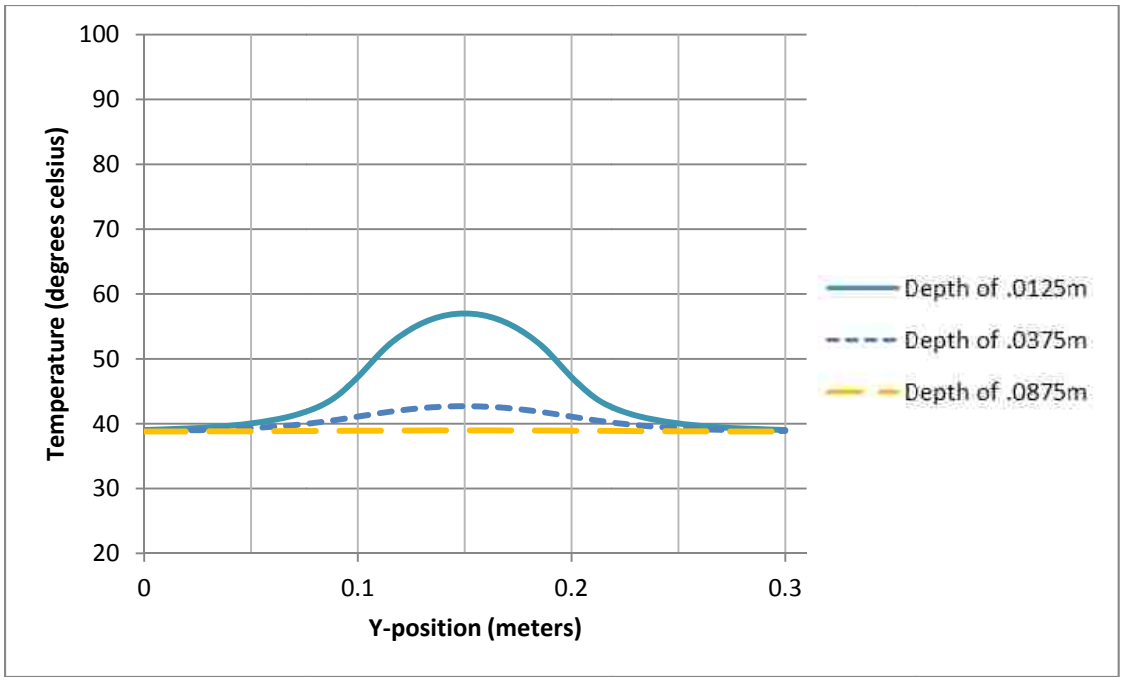

Figure 6.9: Surface temperatures in the Y-axis of orientation over the defect at 3600 seconds and a heat flux of 625 $Js^{-1}m^{-2}$

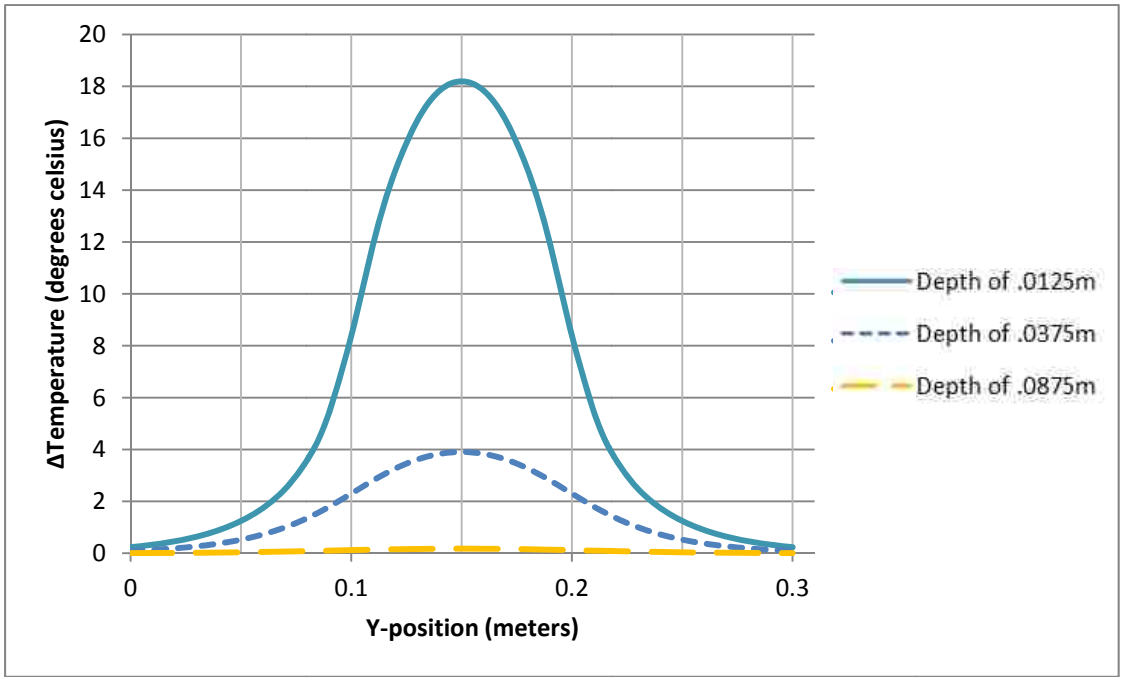

Figure 6.10: The difference in surface temperature in the Y-axis of orientation over the defect at 3600 seconds and a heat flux of 625 $Js^{-1}m^{-2}$

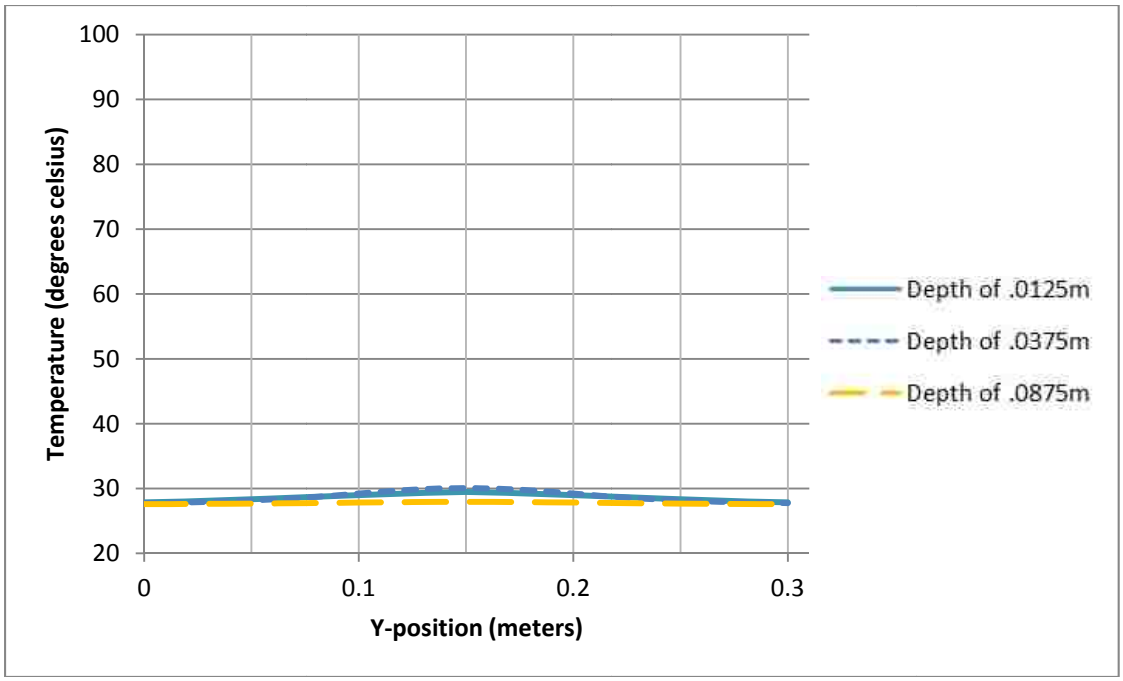

Figure 6.11: Surface temperatures in the Y-axis of orientation over the defect at 5400 seconds and a heat flux of 625 $Js^{-1}m^{-2}$

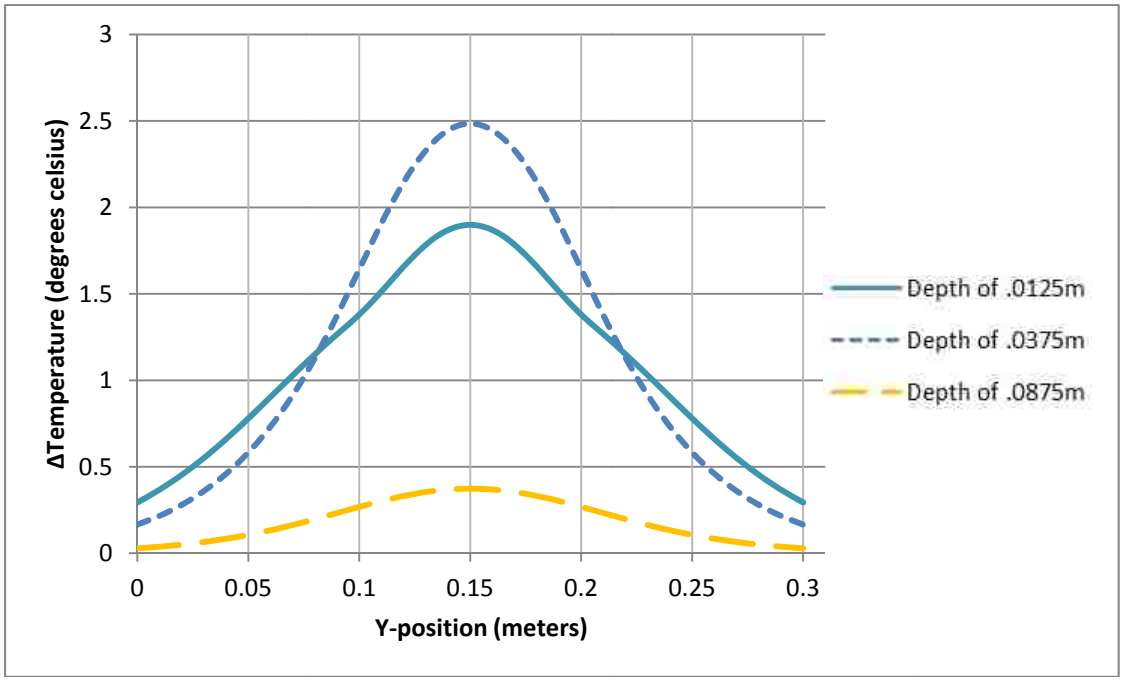

Figure 6.12: The difference in surface temperature in the Y-axis of orientation over the defect at 5400 seconds and a heat flux of 625 $Js^{-1}m^{-2}$

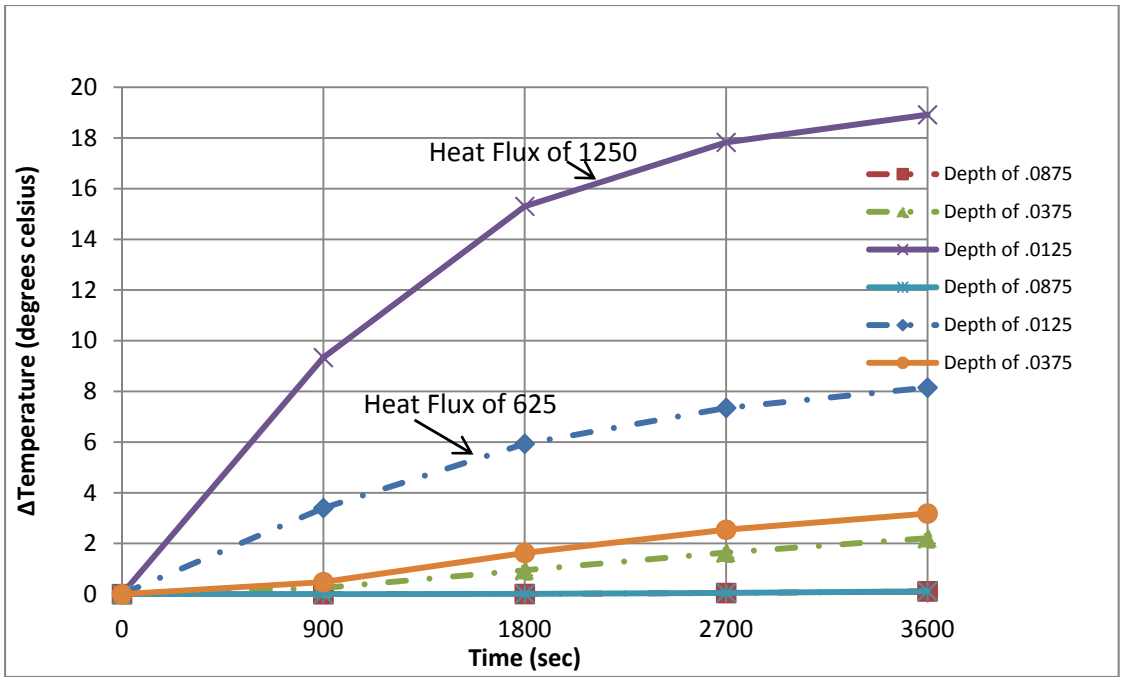

Figure 6.13: Difference in surface temperature between the center of the defect and the edge of the defect

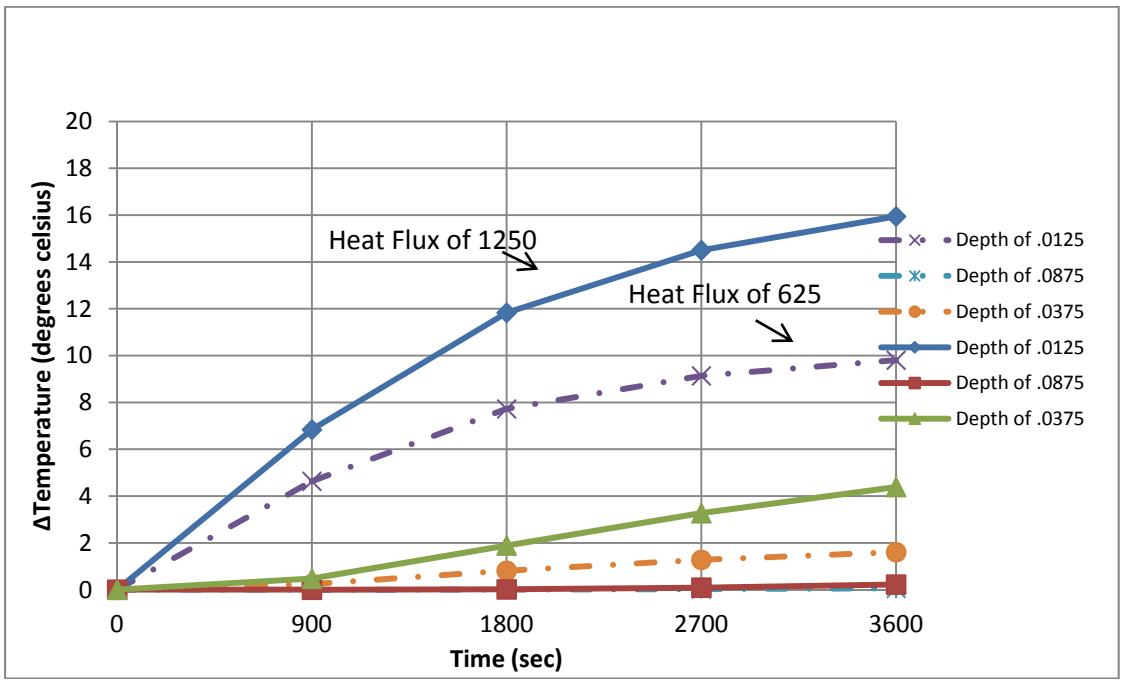

Figure 6.14: Difference in surface temperature between the specimen's reference point and the edge of the defect

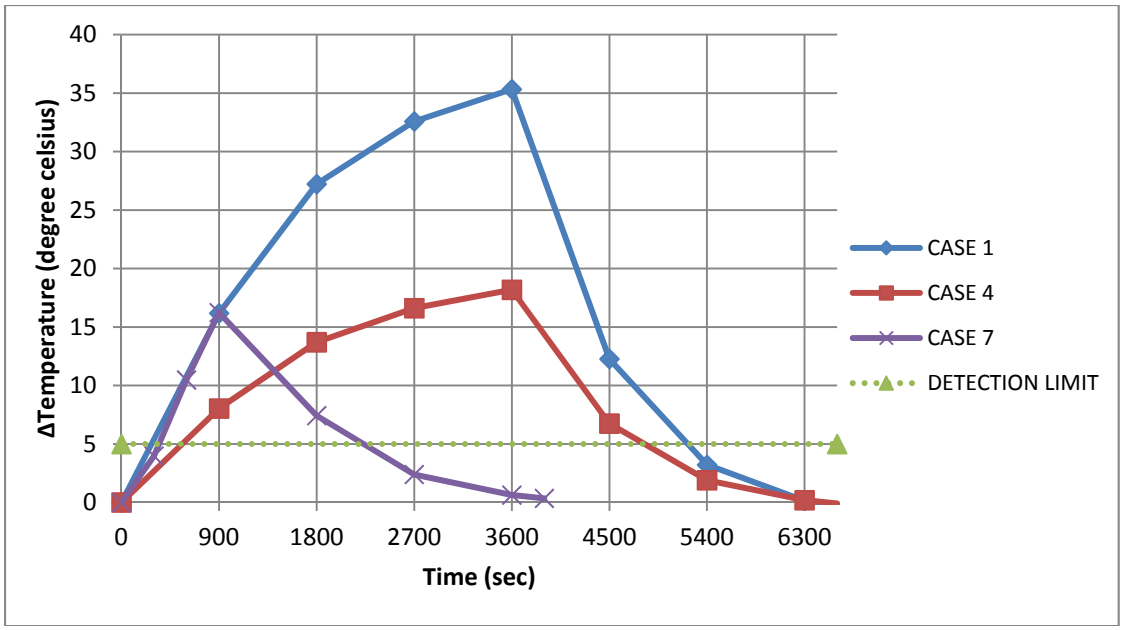

Figure 6.15: Plotted change in Surface Temperature vs. Time for defects located at the depth of .0125 meters (Case 1, Case 4 and Case 7)

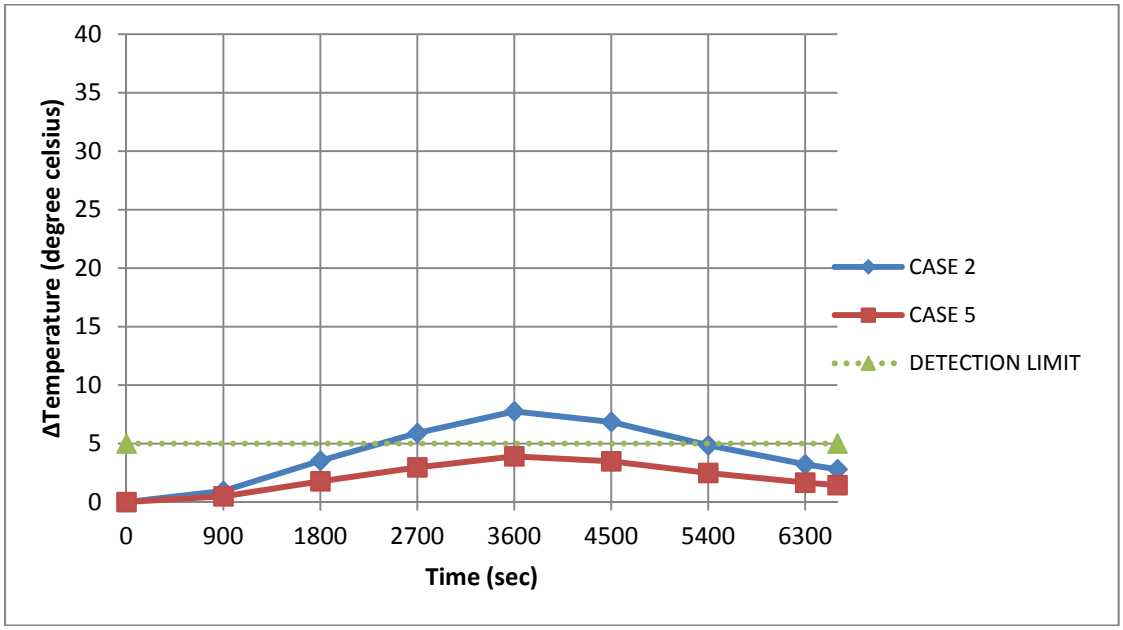

Figure 6.16: Plotted change in Surface Temperature vs. Time for defects located at the depth of .0375 meters (Case 2, Case 5)

CHAPTER 7
SUMMARY AND CONCLUSIONS

7.1 INTRODUCTION

The objective of this research is to demonstrate and validate the effectiveness of impulse thermography for nondestructive testing on Steel-Concrete Composite Structures, and to examine the limitations of impulse thermography with parametric studies. In the previous chapters, numerical results from experiments and finite element models were obtained in order to verify the use of thermography for composite structures. This research has shown the effectiveness of impulse thermography, but has displayed that this method of nondestructive testing has its limitations.

7.2 SUMMARY

The analyses performed in this research indicate that thermography can be used as a form of nondestructive flaw detection for Steel-Concrete Composite structures.

By comparing the results of the BAM model to the BAM test performed by the Technical University of Berlin, it was concluded that the finite element results gave reasonable prediction of the experimental results obtained in the BAM test. In order to keep the validity of the results obtained from the BAM model, a similar model was created to simulate thermography for a Steel-Concrete Composite structure (SCC model).

To investigate the effectiveness and limitations of thermography as a form of NDT on SCC walls, several parameters were studied, as discussed in Chapter 5. The parameters mainly focused on the effects of the change in depths of the defects, heating

intensity and heating durations of the analysis. The results discussed in Chapter 5 showed that defects within the specimen were detectable at certain depths, heating intensities and heating duration. Limitations of the detectability of the defects were seen corresponding to the different parametric cases. This was clearly shown on the graphs presented in Chapter 6. One of the most evident limitations of detecting defects in the subsurface of the specimen was the depth of the defect. Other parameters such as the duration of the heating and cooling process helped determine characteristics of the defects in the model. For example, longer heating and cooling durations allowed a more definitive thermographic surface image of deeper defects that cannot be seen in shorter time durations.

7.3 CONCLUSIONS

The following conclusions are drawn from this study:

- The BAM experimental results produce some discrepancy with the surface temperature results of Defect 7. Although this experiment was used as a validation to the results of the FEM model, the BAM experiment may have some experimental error.

- Table 3.3 shows that the results obtained from the BAM model does differ from the results of the BAM experiment maximum difference in surface temperature. The table shows that there is a range from .02 to 4.95 Kelvin, difference at the measured defects. However, the results from the tables and graphs in Chapter 3, show a comparable surface temperature behavior between the model and the experiment data. For example, the deeper flaws caused a smaller surface temperature difference in both cases.

- Due to the correlation between both the BAM experiment and the BAM model results, it can be concluded that the finite element model does capture the correct behavior of infrared thermography, but not with precise accuracy.

- Based on the parametric cases conducted in Chapter 5 for the SCC wall, it can be concluded that the detection of the defects in the composite structure is limited based on the depth of the defect. In the analyses conducted in Chapter 5 and Chapter 6, it is shown that all defects directly under the steel plate at approximately .5 inches, can be easily distinguished by infrared thermography. At approximately 1.5 inches depth, detection of defects are visible at certain heat fluxes and heating time durations. And at approximately 3.5 inches depth, detection of defects is not visible based on this study.

- Also studied in Chapter 6 is how each of the different parameter fluctuations can be used to optimize the best thermographic image in locating defects and other abnormalities. For example, Figure 6.4 and Figure 6.6 shows that the deeper defects can be seen at longer cooling durations, where defects close to the surface may not show a clear difference in surface temperature; or Figures 6.13 and 6.14 display a large differences in surface temperature when the heat flux is increased.

7.4 FUTURE STUDIES

The main component of this research was based on the finite element model created in Abaqus to simulate the infrared thermography procedure and process. Further research should be done with various other models, with different materials and thermal proprieties to improve the accuracy and understanding of using a finite element model for such analyses. In addition, more convergence studies and mesh refinements on the model should be conducted based on other experiments performed similar to the BAM experiment. Additional convergence studies may help eliminate errors in the model and also create more accurate results.

With a more consistent and accurate model, more realistic applications should be studied; such as other types of composite structures (size, shapes, material properties) and different types of defects (delaminations at composite interfaces and defects filled with different type of non-concrete material).

In this report only seven parametric cases were tested; heat flux, heating duration and flaw depths. In order to get a better understanding between the correlations of these parameters, a larger analysis matrix should be created. More parametric cases such as testing more heat fluxes, creating more defect depths, defects shapes and sizes and more heating durations, will allow a better determination of the limitation of infrared thermography for Steel-Concrete Composite structures.

Eventually, a live infrared thermography experiment of a Concrete-Steel Composite structure should be tested similar to the BAM experiment.

REFERENCES

ACI Committee 318 (2011), "Building Code Requirements for Structural Concrete", American Concrete Institute, Farmington Hills, MI.

ACI Committee 349.3R-02 (2010), "Evaluation of Nuclear Safety-Related Concrete Structures", American Concrete Institute, Farmington Hills, MI.

ACI Committee 228.2R-12 (2013), "Report on Nondestructive Test Methods for Evaluation of Concrete in Structures", American Concrete Institute, Farmington Hills, MI.

Varma, A., Malushte, S., Sener, K., Booth, P. and Coogler, K. (2011), "Steel-Plate Composite SC) Walls: Analysis and design including thermal effects", Research Report Div-VI: Paper ID# 761, Department of Civil Engineering, Purdue University, W. Lafayette, IN.

Dr. Ing (2005), "Use of impulse thermography for quantitative nondestructive testing in civil engineering", PhD Dissertation, Technical University of Berlin, Berlin, Germany.

Schlaseman, C., Russell, J. (2004), "Application of Advanced Construction Technologies to New Nuclear Power Plants", Report MPR-2610 Rev. 2, U.S. Department of Energy, Washington, D.C.

International Atomic Energy Agency (2009), "Advanced Construction Methods for New Nuclear Power Plants", General Conference Document, Vienna, Austria http://preserve.lehigh.edu/cgi/viewcontent.cgi?article=2167&context=etd

Pessiki, S., Kohno, M., Jun Lee, B. (2006), "Analytical Investigation of Steel Column Fire Test", ATLSS Report No. 06-23, Civil and Enviromental Engineering Department, Lehigh University, Bethlehem, PA.

Maierhofer, C., Brink A., Wiggenhauser R. (2005), "Quantitative impulse-thermography as non-destructive testing method in civil engineering – Experimental results and numerical simulations", Report, Federal Institute for Material Research and Testing, Berlin, Germany.

Abaqus/CAE 6.10.1, Dassault System Corporation, Providence, RI.

VITA

Tobi Peter Showunmi was born on July 12, 1988 in Newark, New Jersey. After graduating from Pennsbury High School in 2006, Tobi attended Lehigh University P.C. Rossin School of Engineering in Bethlehem, Pennsylvania. In May of 2010. Tobi earned a Bachelor of Science in Civil Engineering. Tobi continued his education, pursuing his graduate degree at Lehigh University and will receive his Master of Science in Structural Engineering at Lehigh University in 2013.